Monitoring Single Heart Cell Biology using Lab-on-a-Chip Technologies

A thesis submitted for the degree of

Doctor of Philosophy at the University of Glasgow

By

Wei Cheng (B.A, M.A)

Bioelectronics Research Centre

Dept. of Electronics

Faculty of Engineering

University of Glasgow

March 2009

Author's declaration

The work presented in this thesis was conducted by the author and has not previously been submitted for a degree or diploma at this University or any other institution.

Acknowledgements

Abstract

There has been considerable interest in developing microsensors integrated within lab-on-a-chip structures for the analysis of single cells; however, substantially less work has focused on developing "active" assays, where the cell's metabolic and physiological function is itself controlled on-chip.

The heart attack is considered the largest cause of mortality and morbidity in the western world. Dynamic information during metabolism from a single heart cell is difficult to obtain. There is a demand for the development of a robust and sensitive analytical system that will enable us to study dynamic metabolism at single-cell level to provide intracellular information on a single-cell scale in different metabolic conditions (such as healthy or simulated unhealthy conditions). The system would also provide medics and clinicians with a better understanding of heart disease, and even help to find new therapeutic compounds.

Towards this objective, we have developed a novel platform based on five individually addressable microelectrodes, fully integrated within a microfluidic system, where the cell is electrically stimulated at pre-determined rates and real-time ionic and metabolic fluxes from active, beating single heart cells are measured. The device is comprised of one pair of pacing microelectrodes, used for field-stimulation of the cell, and three other microelectrodes, configured as an enzyme-modified lactate microbiosensor, used to measure the amounts of lactate produced by the heart cell. The device also enables simultaneous in-situ microscopy, allowing optical measurements of single-cell contractility and fluorescence measurements of extracellular pH and cellular Ca^{2+} from the single beating heart cell at the same time, providing details of its electrical and metabolic state.

Further, we have developed a robust microfluidic array, wherein a sensor array is integrated within an array of polydimethylsiloxane (PDMS) chambers, enabling the efficient manipulation of single heart cells and real-time analysis without the need to regenerate either working electrodes or reference electrodes fouled by any extracellular constituents. This sensor array also enables simultaneous electrochemical and optical measurements of single heart cells by integrating an

enzyme-immobilized microsensor. Using this device, the fluorescence measurements of intracellular pH were obtained from a single beating heart cell whose electrical and metabolic states were controlled. The mechanism of released intracellular $[H^+]$ was investigated to examine extracellular pH change during contraction. In an attempt to measure lactate released from the electrically stimulated contracting cell, the cause of intracellular pH change is discussed. The preliminary investigation was made on the underlying relationship between intracellular pH and lactate from single heart cells in controlled metabolic states.

List of Notations

E	Potential applied
E^o	Standard potential for the redox couple
R	Molar gas constant
F	Faraday constant
T	Absolute temperature
j	The flux of redox
$k°$	Standard rate constant for electron transfer
α	Transfer coefficient
n	Number of electrons transferred
C_{Red}	Concentration of reduced form of an electroactive molecule
D	Diffusion coefficient
$\dfrac{\partial c}{\partial x}$	Concentration gradient
i	Current density
δ	Thickness of diffusion layer
C^0	Concentration of analytes at electrode surface
i_0	Exchange current
E_{eq}	Equilibrium potential
η	Overpotential
θ_i	Inner diameter
L_d	Length change
V_d	Volume dispensed
T_d	Shot time
$E_{1/2}$	Half-wave potential
E_{pa}	Anodic peak potential
E_{pc}	Cathodic peak potential
v	Scan rate
i_{pa}	Anodic peak current
i_{pc}	Cathodic peak current
r^2	Correlation coefficient
V	Reaction rate

V_{max}	Maximum reaction rate
$[S]$	Substrate concentration and
K_M	Michaelis-Menten constant rate
Q	Charge passed during reaction
Q_{max}	Maximum charge passed under saturating conditions
$[q]$	Quantity of added lactate
τ	Decay time
Y_0	Minimal amplitude of Ca^{2+} transient
Y_{max}	Maximum amplitude of Ca^{2+} transient
A	$Y_{max} - Y_0$
F/F^o	Relative fluorescence intensity

List of Tables

List of Equations

List of Figures

Chapter 1 Introduction

1.1 Single-Cell Based Assay

The cell, the basic structural and functional unit of an organism, plays a crucial role in the regulation and control of life activities. The understanding of biological and physiological processes will benefit from the ability to analyse the complexity of dynamic changes in the context of the single cell. Biologists have been analysing whole organs or tissues and cell cultures for centuries, but techniques used to study single cells have only recently been developed in a multi-disciplinary field that encompasses chemistry, electronics and physiology. In addition, as heterogeneity is present in cell populations, a single-cell based assay will help to elucidate more complex behaviours within cells that might be completely overlooked when studying cell populations.

Techniques developed from single-cell based assays allow the determination of the locations of molecules within cells and to study of rare samples in which only one or a few cells are available, such as patient derived cancer cells. A great challenge in this technique is the requirement for high sensitivity and selectivity, given the fact that the cell has a small size (diameter 7-200 μm) and volume (femtolitres to nanolitres), only trace amounts of intracellular components (zeptomoles to femtomoles) and a rapid biochemical reaction time (millisecond scale).

The first complete assay of a single neuron from *Helix aspersa* was developed using capillary liquid chromatography and capillary electrophoresis (CE) [1], and since then, capillary electrophoresis (CE) has been combined with detection methods such as laser-induced fluorescence (LIF), electrochemical detection (ED) and mass spectrometry (MS) [2-4] for single-cell analysis. Due to extensive research on the complex characteristics of the single cell and the objects contained therein, advances in microscale approaches and techniques for single-cell analysis have been made, enabling information obtained from the single-cell assay to be explored with high temporal and spatial resolution [5].

1.2 Technique Approaches to Single-Cell Signalling

Over the last two decades, there has been dramatic and continuous interest in the dynamic monitoring of intracellular or intercellular processes. These cellular signals released from cells participate in the regulation and control of life activities (for instance, abnormal secretion resulting in the disturbulence of biological functions and the development of disease). Real-time dynamic measurements of the signal molecules from single living cells will help to improve our understanding of complicated physiological processes such as cellular metabolism and intercellular communication. The dynamic signal from a single cell is often at a sub-cellular level (attomole/femtomole quantities) and takes place within less than a few milliseconds, thus making dynamic monitoring of individual cells a significant analytical challenge.

Electrochemistry can provide temporal and spatial information on the release of chemicals from individual cells. Extracellular events, in addition to those occurring inside a cell, can be monitored in real time. Physiologist including neuroscientists often use carbon microelectrodes to track the transport of neurotransmitters and exocytosis. Approaches using light microscopy have already been developed for the dynamic imaging of single cells, among which fluorescence imaging for single-cell analysis has been the most frequently reported. In the past few years, the analysis of even more complex biological systems has been achieved, with the use of MEMS (microelectro mechanical systems) has attracted increased attention. Herein, these key approaches for single-cell signalling are described, with particular attention being paid to single-cell based assays using microfabricated structures.

1.2.1   Electrochemical Sensing

There exists a variety of electroactive intracellular species, which can be electrochemically oxidized either directly [6-8] or by using an enzyme-linked assays [9, 10]. Microelectrodes have intrinsic properties such as their small size, high sensitivity, high selectivity and rapid response times, making them particularly useful for the dynamic monitoring of electrochemically active messengers within single cells. Wightman et al. [11] first used carbon fibre microelectrodes (CFME) to measure the

exocytosis events involved in catecholamine secretion from individual bovine adrenal medullary chromaffin cells. The fabrication involved the use of handcrafted carbon fibre (~7 μm dia) sealed in a fine pulled capillary as a microelectrode. Amperometry and cyclic voltammetry are the two primary techniques that have been used non-invasively to monitor exocytosis from single cells. The advantage of amperometry is that it provides excellent time resolution, while cyclic voltammetry has a lower temporal resolution, providing a current-voltage curve whose characteristics depend on the particular redox nature of the molecule present at the electrode surface. Fast-scan cyclic voltammetry (CV) is particularly useful because it has sufficient temporal resolution to allow the observation of individual secretory processes with simultaneous collection of information on the detected species.
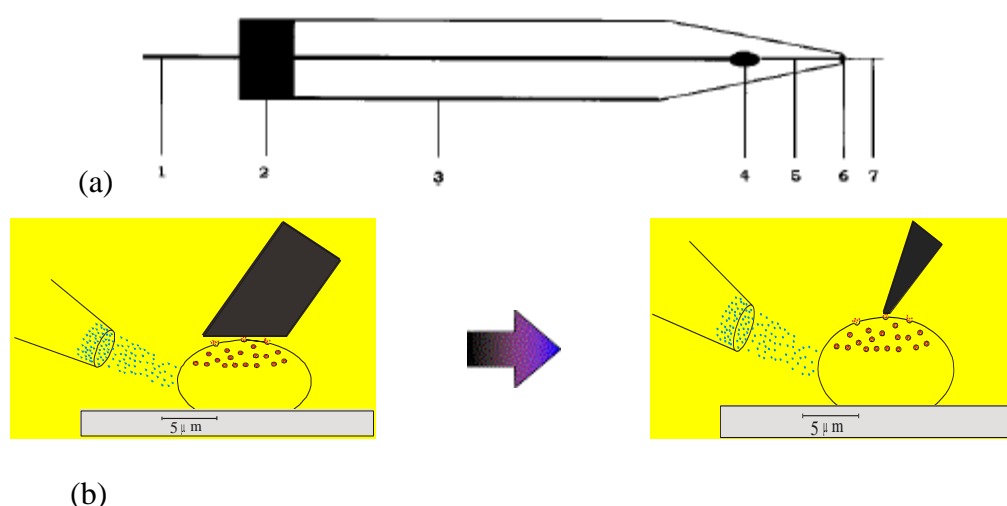
Figure 1.1 (a) Schematic drawing of a carbon fibre electrode: 1, copper wire; 2, epoxy resin; 3 glass capillary; 4, joint of copper and carbon fibre (silver print conductive paint); 5, carbon fibre; 6, glass/fibre interface; (b) Schematic of the experimental arrangements for single-cell measurements using a carbon fibre microelectrode (left) and a nanoelectrode (right). The electrode was positioned close (~1 μm) to the PC12 cell (cell line established from a rat pheochromocytoma), which was cultured on a Petri dish. A microinjector was placed approximately 20 μm from the cell to introduce the signal. The red dots indicate the distribution of vesicles within the cell. The "nanoelectrode" allows the single exocytosis events to be monitored.

These techniques have been widely applied to a variety of intracellular secretions, including many types of neurotransmitters, including dopamine [12], histamine [13], 5-hydroxytryptamine [14], hormones [15] e.g. insulin [16]. Dynamic measurements of single-cell secretions using chemically modified microelectrodes have been reviewed in detail [17]. Ultra-micro or "nanoelectrodes" have the ability to detect secretions from single living cells with sufficient sensitivity and temporal resolution to resolve even

isolated exocytotic events. A new method has been developed for fabricating low-noise carbon fibre nanoelectrodes (CFNEs) [18] to monitor, in real time, single exocytotic events of single vesicles, illustrating the non-uniform distribution of dopamine in single cells [19, 20].

Coupled with other approaches, electrochemical sensing can provide a fuller intracellular profile with high temporal and spatial resolution. Using ultra-microelectrodes and patch clamp techniques, Hochstetler et al. [21] detected the dopamine released in real time from individual neurons of the mouse retina. Kennedy and co-workers [22, 23] measured Zn^{2+} efflux from single pancreatic cells and discussed the exocytosis mechanism of a single pancreatic cell using both electrochemical and optical methods.

However, one of the limitations of carbon-fibre amperometry is that it is difficult to detect total quantities of intracellular analytes because only the partition of total release that is immediately adjacent to the electrode can be recorded with such a high time resolution. In order to characterise dynamic chemical events from single cells with minimal dilution, small containers with well-defined volumes are required, along with electrochemical sensors. A picolitre vial has been fabricated from fused silica capillaries, providing a transparent container that is suitable for the observation and manipulation of a biological cell, sample solution and electrodes, to measure the uptake and release of the neurotransmitter dopamine [24].

1.2.2 Fluorescence Assay

The advent of fluorescent labelling technologies, along with the many of sophisticated light microscope techniques available, has made the investigation of dynamic processes in living cells almost commonplace including chemilunescence, Raman, IR, fluorescence, for example [25]. These light microscopy techniques for live cell imaging have been reviewed by Stephéns and Allan [26] and Roger [27]. Among these techniques, fluorescence imaging for single-cell analysis has been the most frequently reported, as fluorescence imaging enables the direct observation of delicate intracellular structures [28-32]. The advantage of fluorescence imaging is that it allows non-electroactive components to be monitored and directly detects a native released substance with minimal

disruption to the cell. This is in contrast, for example, to microelectrode probing, which generally requires the manual manipulation of isolated cells and electrodes to the desirable location.

In these methods, an inverted fluorescence microscope is generally equipped with a charge-coupled device (CCD) camera, which is used for fluorescence imaging. Different kinds of functional fluorescence microscope systems have been designed to suit the requirements of the various types of imaging analysis for single cells. Examples include the inverted epifluorescence microscope, which is equipped with a mercury lamp imaging fibre-based array CCD detector to obtain single living cell array imaging [33] and the use of confocal laser-scanning microscopy (CLSM) to obtain high-resolution fluorescence images of delicate structures within cells due to an extra optical filter (pinhole) in the light path [34, 35].

Since the advent of green fluorescent protein (GFP) technology, which has revolutionized live cell imaging [36, 37], many other potential fluorescent probes have been introduced into cells. These techniques are highly sensitive and allow the measurement of different cellular events using reporter proteins or fluorescent dyes, widely utilised to monitor intracellular dynamics of single living cells. In some cases, native fluorescence can be used to track the released intercellular species; however, in most cases with these methods, cells are incubated in a solution containing a reagent that reacts with released molecules to form a fluorescent product, which can be detected using an imaging method. Examples of this approach include the monitoring of ATP secretions in astrocyte cultures using a chemiluminescent reaction [38]. Intracellular ions, such as calcium, can also be measured fluorescently using the indicator Fluo family of dyes. For example, the complex of Ca^{2+}-Fluo-2 was excited at both 340 nm and 380 nm and the resulting fluorescence from individual islets was collected. The ratio of the emission intensities after excitation at 340 nm and 380 nm was used as a normalized measurement of intracellular $[Ca^{2+}]$. Similarly, Zn^{2+} released from isolated pancreatic ß-cells was studied using the Zn^{2+} indicator [39]. On the other hand, more functional fluorescence probes have ben investigated to achieve more precise location labelling and higher spatial resolution. Examples of these novel probes include the application of fluorescent semiconductor nanocrystals (quantum dots) in the imaging of single cells [40].

Fluorescence imaging can be used to display intracellular information with a higher spatial resolution and can be readily integrated with a second method to provide improved levels of information. For example, combined with electrochemical methods that can monitor with high temporal resolution, fluorescence methods can display complete information from inside a single cell. Using laser-scanning confocal microscopy combined with the amperometric method, Kennedy and co-workers [41] monitored Zn^{2+} efflux from single pancreatic β-cells with high spatial and temporal resolution and discussed its exocytosis mechanism.
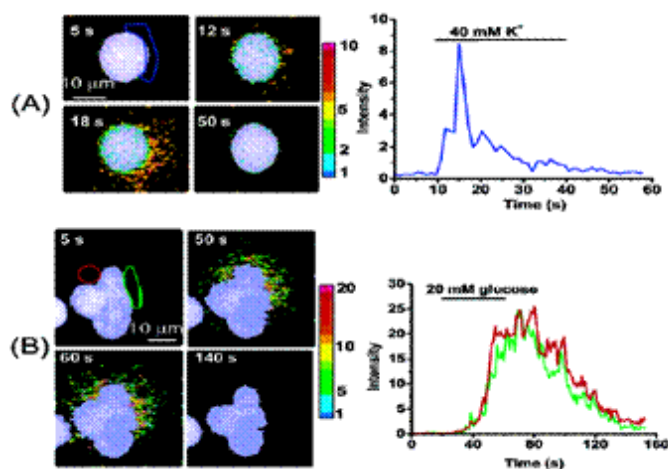
Figure 1.2 Imaging of Zn^{2+} release with FluoZin-3 from isolated pancreatic β-cells at 1 sec temporal resolution. The fluorescence intensity ratio was colour-coded, as indicated by the scale bars. All images were acquired at a rate of 1 Hz (32 scans averaged/image): (a) Zn^{2+} released from a single cell induced by 40 mM K^+ stimulation; (b) Zn^{2+} released from a cluster of four cells induced by 20 mM glucose stimulation [41].

1.2.3 Electrophysiological Assay

Ion channels mediate electrical current flow, playing crucial roles in cellular physiology. Electrophysiological techniques use microelectrodes, which access the interior of the cell, to directly measure the ionic currents through a cell membrane. Among these electrophysiological techniques, the patch clamp technique [42] is the most popular. In its configuration, the cell membrane is partially aspirated into a fine pulled glass pipette (~1 μm) to form a tight electrical seal and then ruptured to provide intracellular access (Fig. 1.3). To measure ionic current flow, it is necessary to make good electrical contact between the pipette and the cell membrane by sucking a single cell onto the pipette. Using

a pipette electrode clamped to the cell, the increase of membrane capacitance associated with exocytosis from a single cell can also be monitored in real time.

(a)   (b)
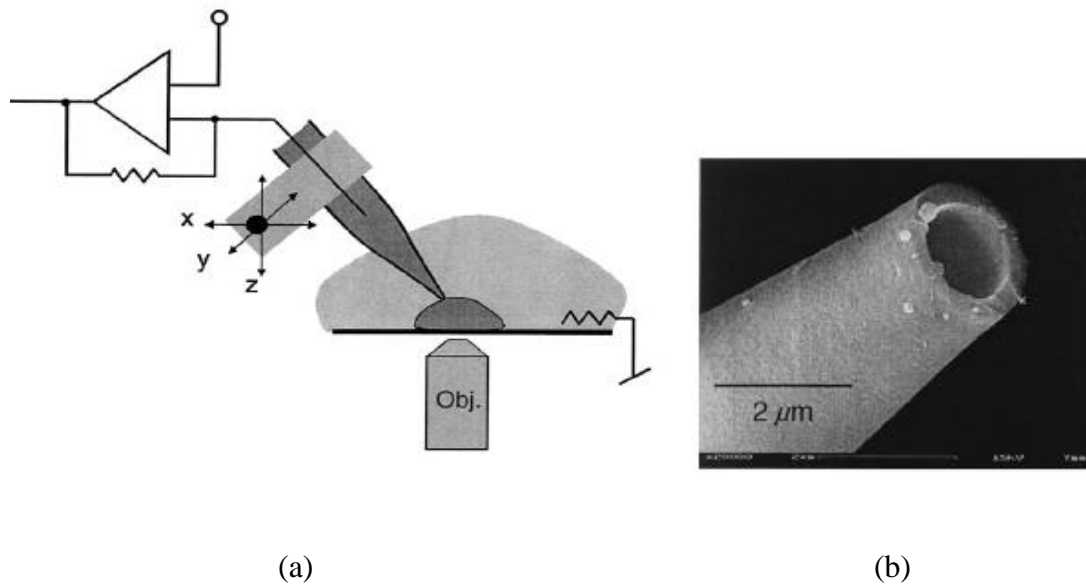
Figure 1.3 (a) Configuration of the typical patch clamp technique; (b) Scanning electron micrograph (SEM) of the tip of a typical borosilicate pipette [42]. Using an x-y-z micromanipulator and an inverted microscope, the tip (diameter 1-2μm), filled with electrolyte solution, is positioned onto a cell. Having applied suction to seal the cell membrane onto the tip, electrical access to the interior of the cell is then established. Changes of ionic current flow (such as ion channels) can then be monitored when substances inside the cell are exchanged with those contained in the pipette.

1.3 The Nature of Excitation and Contraction (EC) Coupling in Cardiomyocyte

The contraction of cardiac myocytes (heart muscle cells) is the most direct marker to determine if the heart function maintains properly [43]. The improper contraction of cardiac myocytes is most likely to be indicated as cardiovascular diseases and sudden cardiac dysfunction. EC coupling is known as a process of contraction of the myofilaments where electrical depolarization of the cell membrane leads to intracellular Ca^{2+} release with conversion of an electrical stimulus to mechanical response where the electrical stimulus resulted in an action potential with the mechanical response being cell contraction.

During this process, the initial trigger for EC coupling is generated by depolarization of the plasma membrane, which allows for Ca^{2+} entry in cardiomyocytes by mechanisms specific to the muscle type. This increase in Ca^{2+} activates calcium-sensitive contractile proteins that then use ATP to cause cell shortening. The potential to stimulate this process

by depolarizing the cell membrane is called action potential. Figure 1.4 illustrated the action potential and consequence phases of membrane potential in a cardiomocyte.

(a)

(b)
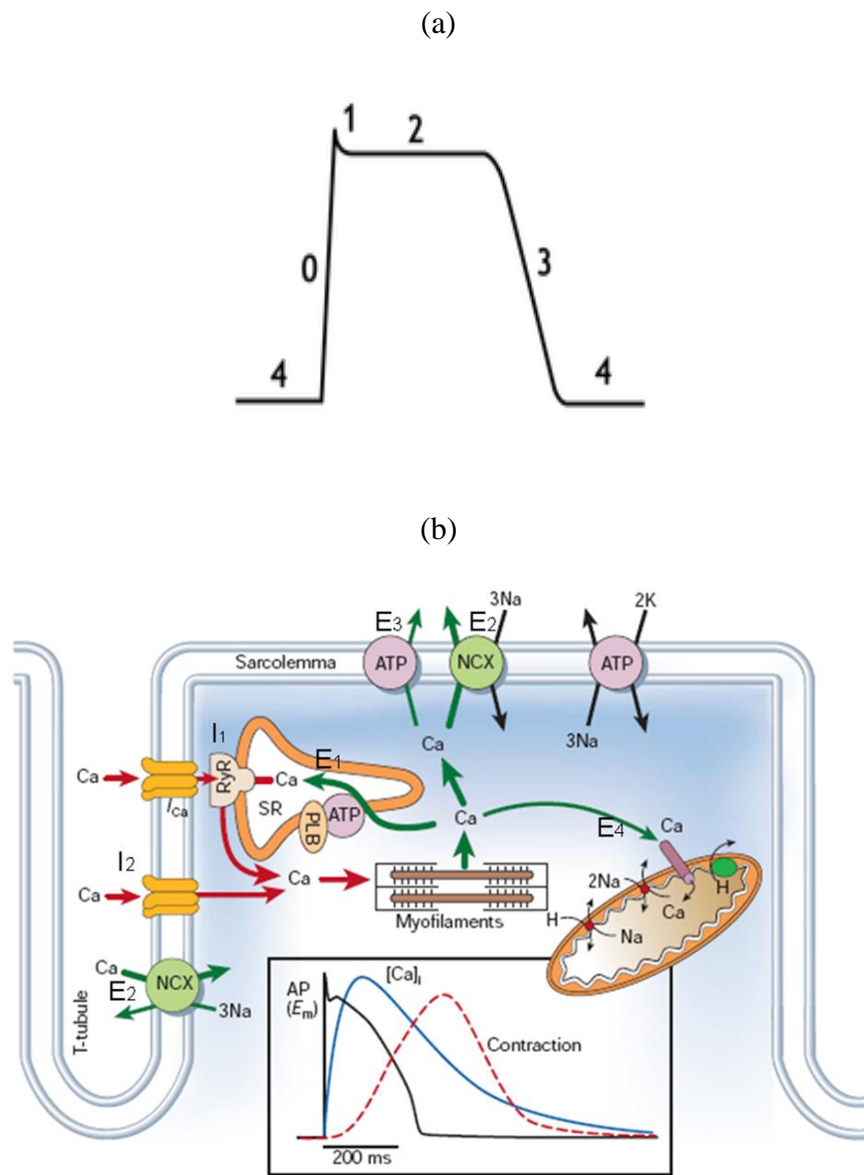
Figure 1.4 (a) The action potential and consequence phases of membrane potential in a cardiomocyte; (b) The Ca^{2+} transport in ventricular myocytes (cardiomyocyte). Inset shows the time course of an action potential. The red arrow indicated the influx of Ca^{2+}. The green arrow indicates the efflux of Ca^{2+} (adapted from [47]).

In Figure 1.4 (a), Phase 0 (zero) is the immediate stimulate potential which depolarize the cell. The sudden increase of membrane potential is due to the sudden increase in membrane permeability to Na^+ ions and decrease in K^+ permeability. Then high Na^+ permeability decreases because of sodium-channel inactivation which makes Phase 1

when decay occurred. The characteristic plateau in Phase 2 results from the opening of voltage-sensitive calcium channels. At this stage, the inward flow of Ca^{2+} ions is equal to that of the outward flow of K^+ ions. Because membrane potential continues to decrease, the Ca^{2+} permeability declines while the K^+ permeability increases. This initiates repolarization efflux of K^+ ions, Phase 3. At phase 4 the membrane potential decreases to its resting value where it will remain steady until the next action potential is generated.

1.3.1 Ca^{2+} Signalling Mechanism during EC Coupling

It is still an ongoing subject in the EC coupling field to elucidate the relation between excitation and contraction. It was known that the ubiquitous second messenger Ca^{2+} is essential in cardiac electrical activity and is the direct activator of the myofilaments, which cause contraction [44].

One source of controversy in the role of intracellular Ca^{2+} in cardiac E-C coupling was whether Ca^{2+} from the extracellular space influx into the cell and contribute entirely to its contraction or there was a reservoir of stored Ca^{2+} within the cell that is responsible for the cytosolic Ca^{2+} increase. It is now known that Ca^{2+} induced Ca^{2+} release (CICR) from the sarcoplasmic reticulum (SR) is the major contributor to cytosolic Ca^{2+} at contraction, about 75% of amount of total cytosolic Ca^{2+} [45].

Much research has also been performed to understand the pathway of the EC coupling process in cardiomyocytes in which Ca^{2+} serves as the second messenger [46]. Figure 1.4 (b) shows the Ca^{2+} transport in ventricular myocytes (cardiomyocyte). Inset shows the time course of an action potential (black curve as the same as Figure 1.4 (a)), Ca^{2+} transient (blue curve) and the contraction (red curve) measured in a rabbit cardiomyocyte at 37 ℃ [47]. In Figure 1.4 (b), the combination of Ca^{2+} influx from extracellular space (I_1) and release from SR (I_2) raises the free intracellular Ca^{2+} concentration ($[Ca^{2+}]_i$), allowing Ca^{2+} to bind to the myofilament protein troponin C, which then switches on the contractile machinery. When relaxation occurs, $[Ca^{2+}]i$ declines allowing Ca^{2+} to dissociate from troponin. This transport has more complicated mechanisms and so far it has been found that four pathways are involved in the Ca^{2+} transport out of the cytosol: SR Ca^{2+}-ATPase (E_1), sarcolemmal Na^+/Ca^{2+} exchange (E_2), sarcolemmal Ca^{2+}-ATPase

(E_3) or mitochondrial Ca^{2+} uniport (E_4). The quantitative importance of these four routes varies between species, for example, the activity of SR Ca^{2+}-ATPase is higher in rat ventricle than in rabbit ventricle (because of a greater concentration of pump molecules), and Ca^{2+} removal through Na^+/Ca^{2+} exchange is lower.

There is different mechanism in EC coupling in cardiac muscle when compared with that in skeletal and smooth muscles [48]. When skeletal muscle is stimulated, the membrane depolarizes, but there is no Ca^{2+} entry. The membrane potential becomes more positive, activating dihydropyridine receptors that are coupled to RyRs, initiating Ca^{2+} release. In cardiac myocytes, in contrast, membrane depolarization induces Ca^{2+} entry through L-type Ca^{2+} channels (LTCCs) located on the transverse tubules, which is necessary to trigger intracellular Ca^{2+} release from sarcoplasmic reticulum (SR). Contractile machinery is activated when the cytosolic Ca^{2+} level increases. It has also been shown that in cardiac myocyte, there is an optimal Ca^{2+} concentration outside SR at which the SR Ca^{2+} channel is activated, beyond or below which the channel was less active or inactivated [49]. The channel inactivation results from Ca^{2+} binding to a low-affinity site on the channel itself only when Ca^{2+} concentration outside SR is high enough.

1.3.2 Measurement of Cytosolic [Ca^{2+}]

The study of cardiomyocyte EC coupling has attracted great attention since the dysfunction of cardiomyocytes may result in cardiovascular diseases [50]. As discussed as above, the Ca^{2+} acts as a universal second messenger in the cardiomyocyte and the contraction mechanism of cardiomyocytes is a Ca^{2+}-triggered process, and therefore, the cytosolic Ca^{2+} measurement ([$Ca^{2+}]_i$) has become one of the most widely used approaches in the contractility study of myocytes [51–53].

The myocyte's mishandling of Ca^{2+} is a central cause of both contractile dysfunction and arrhythmias in pathophysiological conditions. Changes in Ca^{2+} homeostasis have been seen in a variety of diseases, including hypertension and heart failure [54]. In addition, with respect to drug biosafety issue, many chemicals and drugs (*e.g.*, caffeine [55]) have undesirable side effects on the heart as measured by their effects on the [$Ca^{2+}]_i$ mobilization. Monitoring [$Ca^{2+}]_i$ in cardiomyocytes could also facilitate the discovery of cardiovascular drugs (*e.g.*, positive inotropic therapy [56]).

Among the main methods which are used to monitor intracellular Ca^{2+} including microelectrodes, nuclear magnetic resonance and optical imaging, optical methods have been the most powerful [57]. Aequorin was initially used as Ca^{2+} sensitive indicator, which is a bioluminescent protein consisting of apoaequorin, and coelenterazine. It was originally isolated from aequorea forskalea. When aequorin is bound with Ca^{2+}, 465-nm light is emitted, together with apoaequorin and CO_2 [58]. However, this reaction requires twelve Ca^{2+} ions to consume six aequorin molecules for just only one photon emission; as a result, the light output is very low. In addition, the microinjection and aspiration system required to make the introduction into the cell are difficult. In the 1980s, a variety of chemical fluorescent indicators such as BAPTA (1, 2-bis(o-aminophenoxy)ethane-N,N,N',N'-tetraacetic acid) and its fluorescein derivatives of BAPTA like fluo-3 and fluo-4 were produced by Tsien and colleagues [59]. In the absence of Ca^{2+}, the BAPTA moiety quenches the fluorescence of the attached fluorophore by photoinducedelectron transfer. Binding of Ca^{2+} causes a 100-fold increase in the emission fluorescence intensity with no shift in wavelength These reagents have provided trustworthy methods for measuring $[Ca^{2+}]_i$. Since the development of these dyes, Ca^{2+} related intracellular phenomena have been widely investigated [60].

Recently, the interests of many researchers have extended from monitoring $[Ca^{2+}]$ at the cellular level to that of the subcellular level. It has been found that $[Ca^{2+}]$ is not even distributed throughout the whole cell and that intracellular heterogeneity of $[Ca^{2+}]$ (such as Ca^{2+} waves and Ca^{2+} sparks) can be observed in heart muscle. With the advent of the confocal laser scanning microscope (CLSM) in the 1980s and more recently multiphoton microscopy, measurement of intracellular $[Ca^{2+}]$ were possible with precise spatial and temporal resolution which have enabled scientists to record the spatial movement of $[Ca^{2+}]$ at subcellular level in 3-dimension [61].

1.4 BioMEMS and Microfluidics

Since the development of the lab-on-a-chip concept or miniaturized total analysis system in the early 1990s [62], devices based on MEMS have been used in a wide variety of biological applications. The integration of living biological systems into microdevices has been an evolving interdisciplinary field, and has branched into many different

applications, such as biological and chemical analysis [63–65], clinical and forensic analysis [66] and medical diagnostics [67]. Significant advantages have been demonstrated by miniaturizing devices, including their reduced requirements for reagents and cells (critical for valuable samples and for high-throughput screening); short reaction times; their portability for diagnostics; their versatility in design and the potential for parallel operation and even for integration with other miniaturized devices [68-70].

As most biological applications are aqueous-based, microfluidic devices are the most common class of BioMEMS devices. In microfluidics, small volumes of solvent, sample and reagents are moved through microchannels embedded in a chip. The analysis of more complex biological systems, such as living cells, using microfluidic devices has attracted increased significant attention [71-74]. The dimensions of commonly used microfluidic devices fit well with those of cells, enabling the use of these devices in the integration and automation of cell and reagent handling with cell lysis and high efficiency separation, creating the potential for the high-throughput analysis of individual cells.

In the following sections, we discuss several different methods that have been developed to manipulate single cells and different types of chemical and electrophysiological analysis integrated within microfluidic devices.

1.4.1 Single-Cell Manipulation

Electrokinetic pumping is a common technique for the control of flow in microfluidic devices and has thus been used to manipulate cells. Li and Harrison first performed the manipulation and transport of various cells, such as red blood cells, yeast cells and *E. coli*, through a channel network using electro-osmotic and electrophoretic pumping and demonstrated the cell lysis process at a T-junction on a silicon-based microfluidic chip [75]. By applying an electrical field across a thin membrane containing a micro- or nanopore, single cells were transported towards the pore and immobilized on top of it, where patch-clamping techniques could then be used for single-cell analysis [76].

Optical tweezers are known to be able to tether biological molecules to dielectric spheres and then capture the spheres at the focal point of an electric field gradient. Optical or

dielectrophoretic traps have been coupled with microfluidic devices for the manipulation of cells [77, 78]. This method allows individual cells to be isolated and manipulated without contact or contamination; however, these methods are limited by their need for elaborate and complex optics, electronics or both and by the expense of the instrumentation required.

Dielectrophoresis (DEP) is the electronic analogue of optical tweezers [79, 80] and is defined as the lateral motion imparted on uncharged particles as a result of polarization induced by non-uniform electric fields. DEP has been successfully applied at microchip scales to manipulate and separate a variety of biological cells, including bacteria, yeast and mammalian cells. However, this technique suffers from accidental cell lysis or effects on cell viability as a result of the application of a high AC electrical field, and its application is also limited by the complicated instrumentation required. The method required the cell to be polarised relative to its media, meaning that often non-physiological solvents are used to suspend the cell.

Hydrostatic pressure can be used to manipulate cells while maintaining their original viability. A number of different constriction structures of the microfluidic device can be combined with this contamination-free and easily implemented method to manipulate single cells, including microfilters [81–84], microwells [85–87], dam structures [88, 89] and sandbag structures [90], or the interior surfaces of microchannels can be modified with reactive coatings [91–93]. A dam structure [88] has been constructed in a microfluidic chip to allow the location and alignment of cells. This structure allowed controllable numbers of fragile cells to move in the microchannels and to be immobilized in the desired locations under fluid pressure. Recently, there has been increasing interest in the miniaturization of valves and pumps on microfluidic devices for cell manipulation [94-96]. One example of this involved the creation of a microfluidic network, integrated with valves and pumps, which enabled the passive and gentle separation of single cells from the bulk cell suspension, allowing the precise delivery of nanolitre volumes of reagents to that cell [96].

1.4.2 Single-Cell Sensing

The advent of the microfluidic chip offers the potential to develop sophisticated and automated cellular physiological experimental systems that incorporate the manipulation, immobilization and analysis of intracellular parameters and to detect the presence of cell metabolites, even on a single-cell level. Initial efforts toward such systems have demonstrated the use of a microfluidic chip to measure dopamine release from a single cell, with hydrostatic pressure being used to trap a cell while an external microelectrode was manually positioned over it for the measurement of the dopamine released [97], as well as a microfluidic device that incorporates continuous perfusion and an on-line electrophoresis immunoassay, and the monitoring of insulin secretion from single islets of Langerhans (special groups of cells from the pancreas) [98].

1.4.2.1 Electrophysiological Monitoring

Despite the success of the traditional patch clamp technique, it requires complex and expensive equipment and remains highly laborious. Microfluidic based patch-clamp systems uniquely offer the potential of high throughput analysis of single cells and greatly reduce the cost of complicated instrumentation through the miniaturization of the traditional cell-patch setup for the automated manipulation of single cells.

These chip-based devices generally use a planar geometry, where the patch pore is etched in a horizontal membrane to divide the top cell compartment from the bottom recording electrode compartment [99, 100], as shown in Figure 1.5. Recently, a microfluidics-based lateral geometry for electrical measurements of cells was proposed [101]. A 12-channel patch clamp array was developed, incorporating partial cure bonding, which yields robust seals on individually selected mammalian cells under optical observation. Cell trapping on this microfluidic device provided multiple cell addressing and manipulation sites for efficient electrophysiological measurements at a number of patch sites, as shown in Fig. 1.6. A common challenge associated with these devices continues to be the improvement in cell-attached seal resistance to the GΩ range, as lower resistance is insufficient for patch clamp recording. It is important to note that the highly invaginated structure of the cardiomyocyte makes it impossible to create a high impedance seal. To date, there are no examples of a high throughput cardiomyocyte patch clamp device.
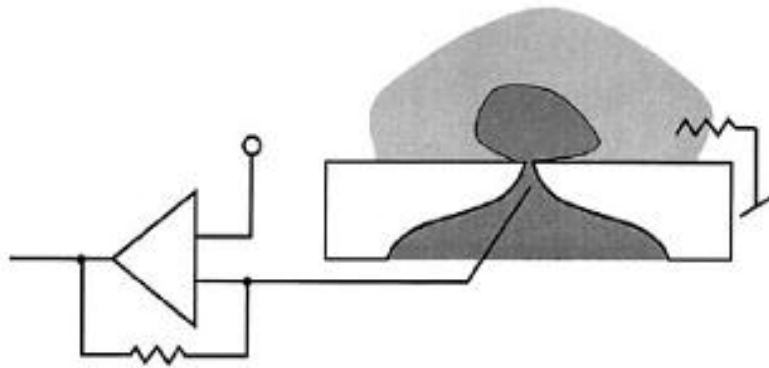
Figure 1.5 The configuration for whole cell recording using a planar chip device. The quartz chip contains a region in which an aperture of micrometre dimensions is produced to trap the cell, which is sealed onto the aperture by brief suction [100].
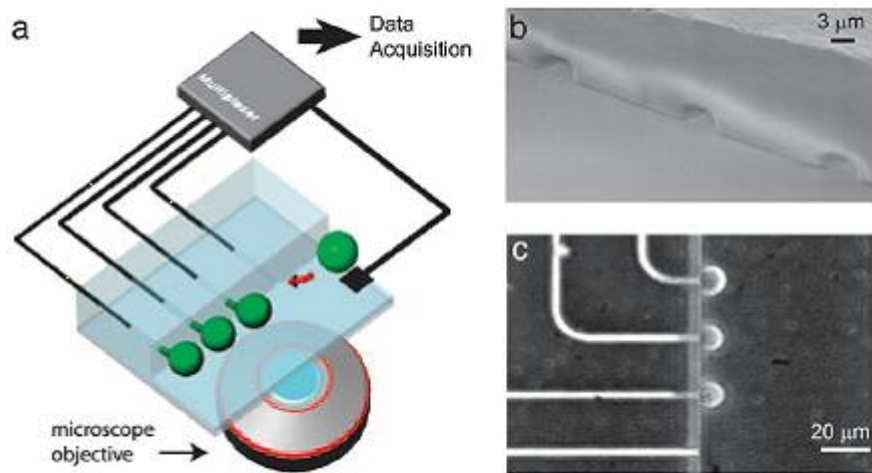
Figure 1.6 Patch clamp array on a microfluidic platform: (a) The device consists of twelve capillaries, with six arrayed along each side of the main chamber fluidic channel; (b) Scanning electron micrograph of three recording capillary orifices as seen from the main chamber; (c) Darkfield optical microscope image of cells trapped at three capillary orifices. Trapping was achieved by applying negative pressure to the recording capillaries [101].

1.4.2.2 Optical Measurement

Microfluidic devices are generally fabricated using transparent materials with vertical channel walls, so that high-sensitivity fluorescent detection can easily be integrated within these devices. The implementation of microfluidic technologies has provided significant

32

advantages over traditional cell-based fluorescence assay in terms of automation and costs. Initial systems aimed to integrate fluorescent detection within microfluidic devices for single-cell signalling and to incorporate continuous perfusion and an on-line electrophoresis immunoassay to monitor insulin secretion from single islets of Langerhans (special groups of cells from the pancreas) [102]. The design of the traditional capillary electrophoresis (CE) system was based on the microfluidic chip in materials such as PDMS or glass, and in this system, cell sampling, loading, immobilization, lysing and separation with laser-induced fluorescence detection have been integrated on-chip to determine the intracellular constituents of individual cells.

Another driving force for the development of systems such as cell-based assay has been a desire to develop high throughput screening, which can provide data that are representative and comparable to those obtained from animal models or clinical trials. A microfluidic system has recently been developed by Caliper Life Sciences for high-throughput screening applications [103], which involves a glass microchip with integrated 'sipper' capillaries, which 'sips' fluids, such as compounds, dyes, buffer, from plate wells, while at the same time continuously drawing solutions, such as enzyme, substrate or cell suspensions, from integrated, on-chip wells (Fig. 1.7). The resulting mixtures are transported downstream in a microchannel, which serves as an incubation chamber, to a detection point where the fluorescence signal is recorded. The system is capable of performing assays with considerably higher throughput and better reproducibility than conventional, plate-based screening platforms. In addition, the chips consume far smaller amounts of chemicals and solvents than conventional systems.
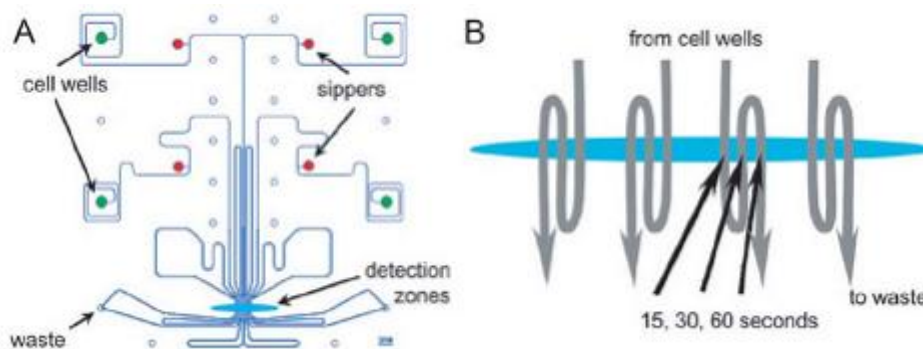
Figure 1.7 (a) Schematic of Caliper Life Sciences' FS-417 four-sipper cell chip for detecting agonist-induced calcium flux. Dye-loaded platelet samples are drawn from the cell wells and continuously streamed through the chip. Platelets are exposed to agonist aspirated from a 384 well microtitre plate at the sipper junction and mixed by diffusion while the sample flows continuously through the chip past the fluorescence detection zone; (b) The microfluidic chips are designed to allow four samples to flow simultaneously through the detection zone three times, allowing 15 s, 30 s, and 60 s incubation intervals. The time to detection is defined by the flow rate and the distance from the sipper to the detection zone [103].

1.4.2.3 Micromachined Electrochemical Sensors

Microfabrication techniques borrowed from the microelectronics industry enable the fabrication of a wide variety of two-dimensional (planar) and three-dimensional devices. The flexible design of microfabrication methods has resulted in a wide variety of electrochemical sensors with different geometries and sizes, providing advantages in many aspects over traditional external microelectrodes that were developed for single-cell signalling. Further, coupled with micromachined sensors based on microfluidic systems, these microfabricated devices build a powerful platform for single-cell analysis that can be highly automated and mass-produced at low unitary cost [104-106]. Yasukawa et al. [107] developed a picolitre volume chamber integrating a working microelectrode for detecting the metabolic flux resulting from the stress responses of a single cell electrochemically through the determination of concentrations of peroxides, thus enabling the investigation of the activity of cellular protection mechanisms. However, in this system, the microelectrodes have not been fully integrated. In the initial attempt to develop completely integrated sensor technology for single-cell signalling, a 600 pL micrometre-scale titre chamber has been fabricated, containing an integrated electrochemical sensor to measure purine produced by a single heart cell during simulated ischaemia using a cascade of enzyme-linked assays [108, 109]. Further miniaturisation of microelectrodes and the reduction in size of microchambers to geometric volumes as

34

small as 160 pL has been reported, integrated to form a picolitre microchamber for amperometric determination of lactate from a single permeabilised heart cell [110].

1.4.3 Technique Significance of Micromachined Systems for Single Cell Signalling

One of the major limitations of carbon-fibre amperometry for single-cell signalling is that it is difficult to detect total quantities of intracellular analytes, as only the portion (2-15%) of the total release that is adjacent to the electrode can be time-resolved and measured [111]. The analytical chamber, produced at micro- or even nano-scale, means that no analyte is lost to the bulk solution, due to the defined analytical volume. In addition, within the structures, there is more efficient transport of analyte to the microelectrode, as a consequence of the specific diffusion profiles for a given geometry, which will often result in higher fluxes of released intracellular species.

In this micromachined system, higher signal-to-noise ratios and faster steady-state responses can be achieved, due to the shorter diffusion distance between the electrode and the analytes to be measured. It is known that the amount of intracellular analyte released is usually small (normally less than fmol quantities), and the corresponding amperometric signal to the released analyte is usually small (less than nA), so there is a need to improve the physiological sensitivity (the ability to measure the intracellular constituents). Under this circumstance, as the volumes of such devices are small (typically less than nL quantities), for a given analytical sensitivity of the device, the decreased dilution of intracellular analytes into the chamber will result in a relatively increased physiological sensitivity.

The development of such a micromachined system with a transparent glass base has provided a platform for the simultaneous observation of the cell using light microscopy during real-time measurement. In this study, this is of particular importance, as the single cardiac myocyte undergoes a dramatic change in both appearance and pathophysiology during simulated contraction. The system allows the direct observation of electrophysiological changes in cells, and also enables the second method employed (fluorescence imaging) to collect more information during the complex metabolism of a single contracting myocyte.

Assays using traditional probe type microelectrodes are also elaborate because the electrodes have to be individually fabricated and manually positioned very close to cells using a microscope and micromanipulators. The integrated system (micromachined sensors integrated within the analytical chamber) decreases the demands on the skill of the operator, although it increases the skill required in the microfabrication of the electrodes.

Finally, there is an ultimate demand for cell-based assay with improved throughput which can potentially provide information that is comparable to that obtained from animal models or clinical trials. The micromachined system may be integrated within microfluidics to produce apparatus with a lab-on-a-chip format potential for high throughput cell analysis.

1.5 Single Cardiomycocyte Study in Microfluidic System

Cardiac disease remains the leading killer and cause of morbidity in the developed world. It is a complex pathology, with myriad factors including electrical, chemical, metabolic, mechanical, and immunological factors manifesting on scales ranging from the molecular to the whole organism. Ultimately, the fate of an individual's heart comes down to what happens at the single cardiac myocyte. As discussed previously, with the advance of microfluidics and microfabrication technology, these microfluidic systems can provide a unique platform for *in vivo* environment for cell culture as well as reaction and detection environment for cell-based assay. In the last decade, microfluidic system has been widely used to study individual biological cells not only because the dimensions (10–100 um) of microfluidic channels are highly compatible with the sizes of the biological cells [112-114], but also because the most cell-based assay techniques, such as electrical, optical, electrophysiological methods, can be integrated into these microfluidic systems. The integration on such as a micro-scale device has provided a prospect high throughput analysis/screening of biological cells which therefore is believed to have significant contribution to the research in drug discovery and cellular physiology study.

As stated, microfluidic systems have been developed to study the single cardiomyocyte. The cardiomyocyte, with its long cylindrical (rather than round) shape, large cell size, and

fragility makes the manipulation and selection of the cell rather difficult. To date, there are a few reports on the study of single cardiomyocyte in microfluidic chips [108, 110, 116-125]. These studies are caterogrised and reviewed in the aspect of application.

1.5.1   Cardiomyocyte Stimulation and Membrane Potential Measurement

Like other cells type, extracellular potentials of cardiomyoctes are generally measured using saline-filled glass micropipettes which are loosely held to the cell membrane mechanically or by suction. This technique could be laborious and time consuming as the thin membrane can be ruptured with the risk of destroying it during the measurement. In addition, with patch pipettes set-up, it is difficult to realise simultaneous recordings from multiple separate sites on the same cell. Therefore, automated electrophysiology in microfluidic system has emerged as an alternative method with the potential to produce a higher throughput, which is also less laborious and technique demanding over traditional glass capillary electrode in cell patch clamp techniques [101].

Measurements of extracellular potentials using planar microelectrodes require the size of each recording electrode to be comparable to the size of the cell [115]. When the cell does not entirely cover the electrode, a recordable signal cannot be obtained from that electrode because of a voltage division across the areas exposed to the conducting solution. Initial efforts to the designs of the planar microelectrode for cardiomyocte extracellular monitoring have included an array of microelectrodes in 100 pL large microscopic chambers to stimulate single adult rabbit ventricular myocytes [116]. In addition, a hybrid chip was described which combines a microfluidic network fabricated in a silicone elastomer (PDMS) with planar microelectrodes to enable the continuous perfusion and chemicals delivery to the cardiomyocyte, and was used to measure extracellular potentials from single adult murine cardiac myocytes in a restricted extracellular space. Single cells were trapped inside the 100 pL microchamber by pressure gradients and maintained for several hours by continuous perfusion. The localized delivery of drugs to a portion of the cell was also demonstrated [117].
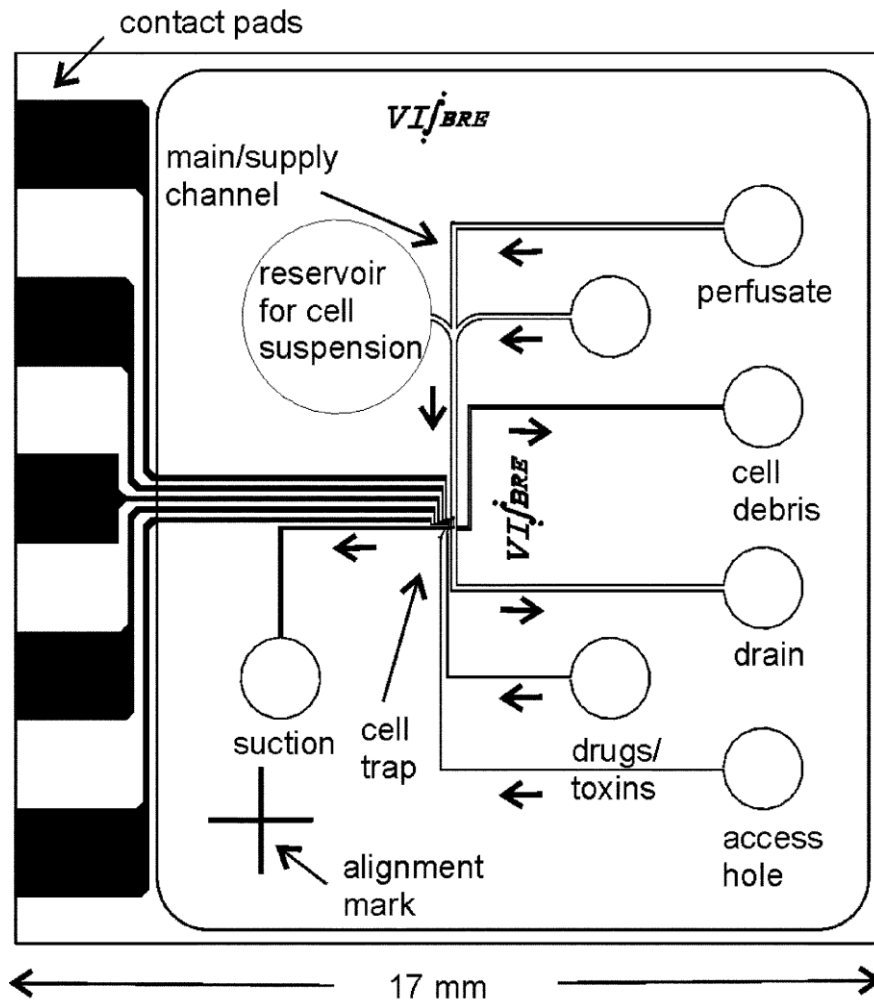
Figure 1.8 Schematic overview of the microfluidic channels and microelectrodes. The cell trap is located in the center of the device at the confluence of the vertical fluidic channels and the horizontal electrode traces. The cell suspension is pipetted into the 60 μl reservoir on the upper left side of the chip, from where single cells are drawn into the microchamber by pressure gradients. Arrows indicate the directions of the pressure gradients applied by using external syringes during the experiment [117].

The irregular shape and the surface structure of cardiomyocytes has prevented the formation of a high-resistance seal on this existing apertures using the fabricated method. To overcome this limitation, Klauke have developed a microfluidic structure to form an insulating polymer partition (gap), which served to define two microfluidic pools reminiscent of the sucrose gap technique [118]. A single cadiomocyte was aligned within the device, bridging two microfluidic pools, and lying across the lithographically defined electrically insulating defined electrically insulating polymer partition (or gap). The cell was electrically stimulated across this insulating gap and the recorded extracellular currents and voltages were related to the size and duration of the trigger pulse with a 20 MΩ seal resistance across the cell between the two microfluidic pools. Using this similar

38

device, two ends of a single cell confined in a microfluidic device can be independently superfused using dual superfusion pipettes to study the response of the stimulated end of the cardiac myocyte for example, during evoked electrical activity by application of drugs, in comparison with the untreated cell end [119].

1.5.2   Intracellular Components and Metabolic Monitoring

As a consequence of the fact that Ca^{2+} is generally regarded as a universal intracellular messenger, regulating a diverse range of cellular processes, Ca^{2+} measurements are now one of the most important validation assays in high-throughput drug screening in the pharmaceutical industry. It has been known that many anticancer drugs (*e.g.*, daunorubicin, DNR) have a serious toxic effect on the heart, and the prolonged use of DNR can cause severe heart damage [120]. Therefore, the study of the toxicity (*e.g.*, cardiac effect) of drug candidates (*e.g.*, antitumor drugs) on hearts based on $[Ca^{+2}]_i$ measurements would also provide the necessary information to help the drug candidates to pass drug safety requirements of regulatory agencies.

A microfluidic method to integrate various single-cell operations as well as on-chip dye loading and quantitative analysis of intracellular calcium concentration have enabled the study of the contraction of a single cardiac myocyte as has been proposed by Li's group [121]. The same group has recently developed a microfluidic device which allows studying the effect of the anticancer drug candidate – isoliquiritigenin (IQ), and the chemotherapeutic drug-DNR, on calcium mobilization of a single cardiomyocyte [122].

By measuring the acidification rate in the extracellular environment, the metabolic activity of cells can be investigated, and the impact of chemicals and drugs on cell physiology can be also studied by measuring the decrease in pH that occurs as acidic metabolites build up in the extracellular space. A glass substrate with thin film pH sensitive IrOx electrodes was sealed to a replica-molded polydimethylsiloxane (PDMS) microfluidic network with integrated valves, which allows the trapping of single cardiac myocytes and the measurement of the pH of the single myocyte from the Acyl-CoA dehydrogenase (VLCAD) deficient mice [123, 124]. This device equipped with pH sensors could have potential applications in high-content high throughput drug screening efforts.

In the efforts towards precisely control of the metabolic state (such as ischemia) of the single mycyote on chip, Ganitkevich has developed a glass chip on which microscopic rectangular wells have been etched into a hydrophobic photoresist coating with each 192 pL well accommodating a single ventricular myocyte [125]. The open fluid volume was kept constant in time, and the oxygen tension in the picochamber was rapidly equilibrated with that in the gas phase, where it was controlled at sufficiently low levels. This system is used to stimulate the myocyte to ischemia and studied responses of the sarcolemmal ATP-sensitive K^+ (KATP) channel current, to graded ischemia and to rapid changes of the ischemic grade.

The ability to analyse cell metabolic products in real time could enhance our understanding of cellular physiological processes, such as those during inter- and intracellular communication between and within isolated cells. Typically, the release of small (sub-attomole) quantities of metabolites occurs rapidly, within fewer than a few hundred milliseconds of cell stimulation, making the dynamic monitoring of an individual cell a significant analytical challenge. By using restricted low extracellular volumes, single heart cell signalling was investigated with electro-chemically linked assay: using a micrometre-scale chamber containing an integrated sensor to measure adenosine released from a single lysed heart cell, which demonstrated that adenosine reaches the extracellular zone regardless of its metabolic condition [108] and the development of two-electrode sensors integrated within a picolitre microchamber for the amperometric determination of lactate from single lysed healthy myocytes or those in a state of stimulated hypoxia [110]. In these studies, the bulk fluid in the chamber was removed once a myocyte was captured, leaving the myocyte isolated in its own volume of extracellular fluid trapped within the well by surface tension. To date, most of these previous studies have only involved taking measurements from *quiescent* heart cells, in which inhibitors or detergents have been used to promote changes in cell physiology. There has been little work on developing "active" cell assay, where the heart cell's metabolic state and physiological function are controlled on-chip. There is great demand for the development of an "active" cellular assay for single heart cell signalling so that *in vitro* real-time single-cell signalling could be achieved during cell metabolism with the metabolic state of the cell also controlled on-chip.

In this work, we have developed micromachined systems for single heart cell signalling by using an electrochemical microbiosensor together with stimulatory electrodes, integrated within a pL-scale microfluidic chamber, enabling the cell to be stimulated at pre-determined rates, and to explore the metabolic effect of making the cell "work" under different controlled metabolic conditions. These systems incorporate a microfabricated enzyme-modified sensor to determine the lactate produced from single heart cells in controlled metabolic states, and also allow other important metabolites (such as H^+ and Ca^{2+}), as well as cell length, to be optically measured, simultaneously providing detailed information about the heart cell's electrical and metabolic state, such as the relationships between simultaneous changes to these metabolites and the cell's metabolic state. We chose to measure the single-cell production of lactate because it is an important cellular metabolite and of significant clinical interest in heart cell physiology. For example, lactate levels can be monitored to indicate the health of a cell, because damaged cells, or those in which oxygen supply is restricted, tend to produce larger amounts of lactate.

1.6 Thesis Outline

Chapter 2 will address the design and microfabrication of two microfabricated devices that are used throughout this study. One platform involves five individually addressable microelectrodes, fully integrated within an SU-8 microfluidic chamber. The second device comprises an electrochemical sensor array integrated within a microfluidic array chamber made using PDMS. The fabrication methods and the use of SU-8 and PDMS as the two primary polymeric materials to fabricate microfluidic chambers at different aspect ratios will be explored.

In Chapter 3, the first platform is electrochemically characterised using the ferrocene monocarboxylic acid redox couple, with the subsequent enzymatic determination of lactate with lactate oxidase (LOD). An in-house picolitre-scale microinjection system is developed and used for the optimization of the lactate assay using an enzyme-modified bioanalytical sensor. The kinetics and stability of the LOD immobilised sensor are investigated.

In Chapter 4, a single heart cell is manipulated and electrically stimulated to contract at a pre-determined frequency. Real-time measurements of single-cell contractility and fluorescence measurements of extracellular pH and cellular Ca^{2+} from the single beating aerobic heart cell are achieved. Stimulated metabolism of the single anaerobic cell is investigated through the real-time monitoring of cell contractility shortening and extracellular pH during continual pacing. The quantitative measurement of lactate from a single aerobic/anaerobic heart cell in response to electropermeabilisation is achieved.

In Chapter 5, a sensor array integrated within an array of PDMS microfluidic chambers is presented. An in-house dual pipette system is established to dispense pL lactate and to electrically characterise the biosensor by the determination of lactate using an enzyme-linked assay. Real-time fluorescence measurements of extracellular pH and cellular Ca^{2+} during cell contraction are achieved. The mechanism of cell acidosis during stimulated cell contraction is investigated using real-time monitoring of intracellular pH. The underlying mechanism is further investigated, with an attempt to spontaneously measure the extracellular lactate during continuous cell contraction. The key advantages of this device over the single chamber device in cell manipulation and parallel analysis are presented, such as the fact that it does not require the regeneration of fouled electrodes.

Finally, Chapter 6 describes the design and fabrication of a simple integration of microfluidic systems for real-time analysis of a single heart cell. Individually addressable microelectrode array systems towards high-throughput screening of single myocytes are proposed.

Chapter 2 Device Design and Microfabrication

2.1 Introduction

This chapter describes the design and fabrication of single microfluidic chambers and chamber array devices integrating electrochemical sensors and sensor arrays. A range of functional materials have been used as substrates for the fabrication of microfluidic chambers wherein single-cell monitoring can be conducted. This is followed by a description of the construction of an Ag|AgCl quasi-reference electrode using electrochemical deposition or chemical vapour deposition. The stability of the reference electrodes using these two methods is compared.

2.2 Chemicals and Materials

All solutions were prepared using high-purity deionized water (Millipore Elix 10) and analytical reagent grade chemicals, without further purification. Unless otherwise stated, all chemicals were obtained from Sigma-Aldrich (Dorset, UK). SU-8 10 was obtained from Microchem Corp (Newton, MA, USA). SU-8 developer (Micro deposit EC-solvent: propylene glycol monomethyl ether acetate) was from Shipley Europe Limited (Coventry, UK). Isopropyl alcohol and glass slides were obtained from BDH Laboratory Supplies (Poole, England). Poly(dimethylsiloxane) (PDMS) was obtained from Dow Corning (Northants, UK). Photoresist S1818 and AZ 4562 were obtained from Shipley Europe Limited (Coventry, UK).

2.3 Methods

2.3.1   Design

2.3.1.1 General Design Considerations

When developing a microfabricated format for the real-time monitoring of intracellular contents from single living cells, there are many considerations that must be addressed. Firstly, all materials used in this device must be biocompatible with the cell, at least for

the relatively short-term experiments required for this research. Secondly, the ability to maintain the physiochemical environment of the cells must be preserved while providing the flexibility to perform real-time electrochemical analysis. Thirdly, the desire for spatially localized electrode sites must be balanced against such things as the optimisation of the stimulation field to be applied and the signal-to-noise ratio of the measurement to be performed. Finally, the availability and fabrication requirements of the materials have to be considered. These issues will be addressed in more detail in a later section.

2.3.1.2 Integrated Sensor within Single Microfluidic Chamber

In this design (Design 1), as shown in Figure 2.1, three-microelectrode biosensor systems have been configured: a working electrode for measuring the signal, a reference electrode for maintaining the working electrode at a constant potential and a counter electrode that completes the electrochemical current by supplying the current. Two stimulatory electrodes have been incorporated within the microanalytical device to produce the field to electrically stimulate the cell. All five electrodes are integrated within an electrochemical analytical chamber, where the electrochemical measurements are performed. As discussed in Chapter 1, this analytical microchamber enables more efficient transport of cellular analyte, allowing intracellular species released from single cells to be measured without loss to the bulk solution.
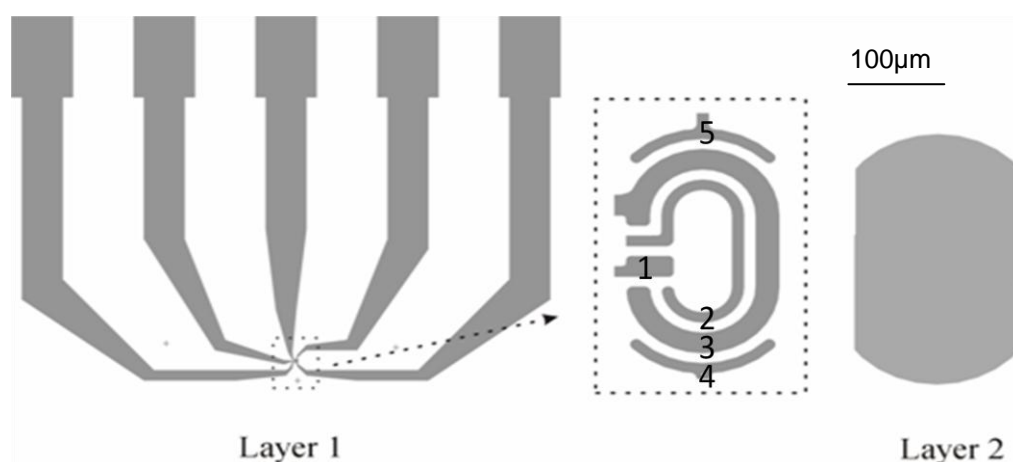
Figure 2.1 Diagrams of the design of the electrochemical devices: Layer 1: the electrode layer, including contact bands and the central configuration of five microelectrodes: 1, reference electrode; 2, working electrode; 3, counter electrode; 4 and 5, stimulation electrodes (scale 60:1); Layer 2: structure of the microchamber (scale 60:1).

There are certain key factors that must be considered in the design of the three-microelectrode biosensor system. To balance two issues, it has to be small size to reduce the double-layer capacitance that generates the major signal noise, and also has to have a large surface area, exposed to the analytes to obtain high sensitivity. The working electrode was designed with a ring structure. The spatially localised electrode geometry was designed to optimise the stimulation field and the signal-to-background ratio of the sensor. In this latter respect, the counter electrode was designed to have a sufficiently large area to ensure that the redox process at the working electrode was not limited. One further consideration was the potential toxicity of Ag^+ in order to avoid compromising the cells, the reference electrode was designed to be of small size. However, such a compact microreference design could mean that the silver layer is electrochemically deposited across other electrodes. This problem was resolved by alternatively using standard photolithography and metal evaporation to confine the area of the silver layer.

Metals with a sufficiently low overpotential used in Chapters 4 and 5 for the oxidation of hydrogen peroxide (the final product of lactate oxidation) were used in order to minimise electrochemical interference with the cell (which would be expected to occur at large redox potentials). Previous reports [116, 126] suggest that more efficient stimulation is provided when the electrical axis of stimulation is parallel to the long axis of the cardiac cell, as measured by the reduced potential required for effective cell excitation. The two stimulatory electrodes were therefore fabricated within the microchamber so that the cell could be aligned parallel to the electrical field. In this case, a sufficiently low voltage stimulatory pulse could be applied, avoiding both electrolysis and polarisation of the electrodes and minimising the ionic flux caused by stimulation, which could interfere with measurements.

2.3.1.3 Integrated Array Sensor in Microfluidic Multi-chamber

This design (Design 2), as shown in Figure 2.2, comprised an array of five planar microelectrodes, three of which are configured as a biosensor array system, while the other two are used as stimulatory electrodes. The working array (20 μm wide) and counter array (40 μm wide) were designed between the two stimulatory electrodes to obtain the dynamic cellular information when the cell is electrically stimulated. The gap between

stimulating electrodes (20 µm in width) was constrained to a maximum of 200 µm, enabling an average sized ventricular myocyte (~160 µm long, 25 µm wide) to be placed between the two stimulating electrodes while minimizing the applied potential for field stimulation. A multi-channel array (fifteen) elements was designed to run across the sensor array to create an array of microfluidic "main" chambers (40 µm pitch) for up to fifteen single myocytes. The "main" chamber has a width of 50 µm width and a length of 250 µm to provide an arena for a single ventricular myocyte while minimising the analytical volume to provide more sensitive analysis (and hence, the dilution of any signal produced by the cell). The working and counter electrodes and the two stimulatory arrays were all located within the "main chamber", which has a confined width of 50 µm, whilst the reference electrode (20 µm wide) is 100 µm away from one side of the stimulatory electrode, located within one of the connecting channels (200 µm long, 30 µm wide).
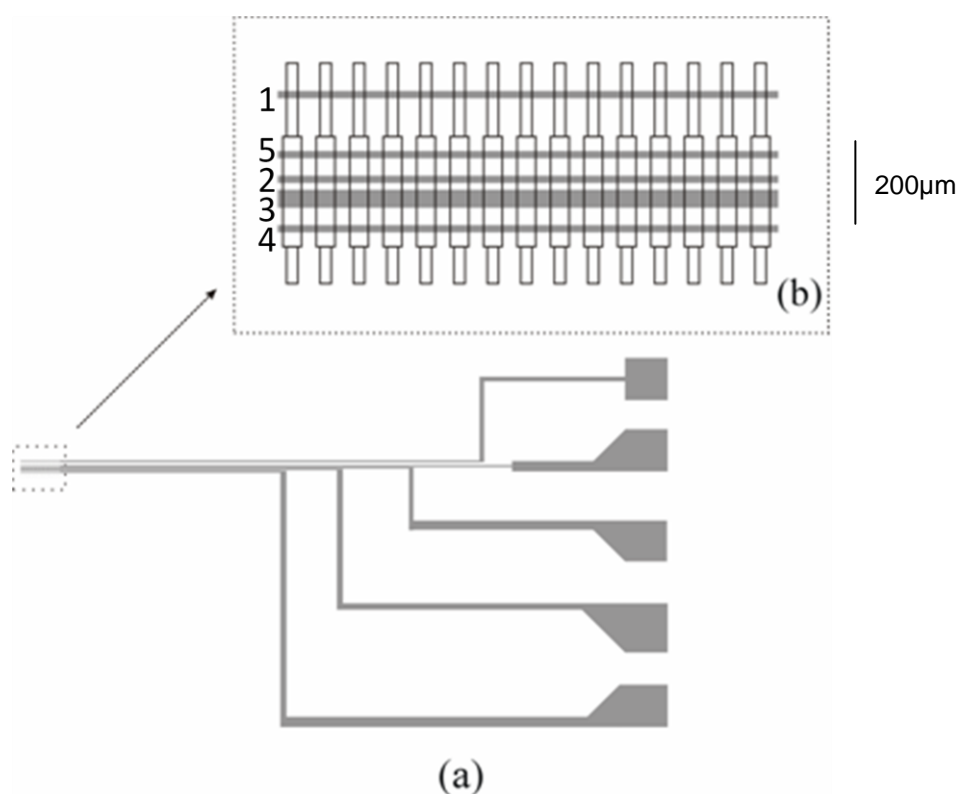
Figure 2.2 Diagrams of design for a sensor array in a multi-channel configuration: (a) layout of electrodes: 1, reference electrode; 2, working electrode; 3, counter electrode; 4 and 5, stimulation electrodes (scale 2:1); (b) central configuration of microchannels confining a sensor array (scale 30:1).

This design improved the rate of cell analysis by creating an array of microchambers within each chamber, integrated with a five-electrode sensor system, to avoid elaborately re-making the device, particularly when one chamber contains fluorescent dye or the

electrodes were fouled by cellular contents following cell lysis. Furthermore, the microreference electrode is relocated far from the main chamber to minimize the effect of the cell caused by the potential toxicity of Ag^+; additionally, this Ag|AgCl reference electrode can be of a larger size, to increase its stability. .

2.3.2 Fabrication

All microfabrication was adapted from standard photolithographic methods, including metal evaporation, electrochemical metal deposition and lift-off. Masks for all microelectrodes and microfluidic structures were designed in L-Edit[TM] and produced as chrome-coated maskplates using a Leica EPBG5-HR electron beam writer (Leica, Germany).

2.3.2.1 Substrate

Microscope glass coverslips and glass slides were used as substrates to allow the recording of intra- and extracellular fluorescence signal as well as cellular morphology with oil and water immersion lenses. Specifically, regular microscope coverslips (22 x 40mm) with thickness No.1 (between 130 and 170 μm) enable the use of lenses with a high numerical aperture and a low working distance of 300μm.

Cleaning of the substrate is essential in order to remove contamination and provide a clear surface for further fabrication processes. The glass slide was immersed in Opticlear and sonicated for five minutes. This process was repeated with acetone and then methanol. The slide was rinsed with RO (deionised) water and blown dry, removing any condensation.

2.3.2.2 Microelectrode Pattern

The microelectrodes were patterned onto the cleaned glass slide. The slide was spun using an appropriate primer, then spin-coated with S1818-positive photoresist at 4000 rpm for 30 seconds. The slide was then baked for 15 minutes (in a 90°C oven) prior to a 15-minute immersion in chlorobenzene. The chlorobenzene soak facilitates the final lift-off stage, ensuring a well-defined electrode pattern with clean and sharp edges. Following the

chlorobenzene soak, the slide was blown dry and baked for another 15 minutes at 90°C. The microelectrode mask pattern was positioned against the resist using an HTG mask aligner and exposed to UV (400 mJ·cm^{-2}, 350-450 nm) for 10 seconds. The resist was developed using a 1:1 mixture of RO water and Micro Deposit Concentrate (a suitable developer for S1818 photoresist) for 75 seconds, rinsed in RO water and then blown dry.

It is beneficial to check the development of the resist under a microscope. Excess resist can be further developed using the same method. This can be repeated until the desired pattern for the electrodes was achieved. However, care was taken not to overdevelop the pattern, as this will degrade the height and shape of the remaining resist.

Metals were then deposited using an electron beam evaporator, producing a multilayer electrode structure of Ti/Pd/Pt (10/10/100 nm). The 10 nm Ti metallic underlayer allowed for good adhesion of the platinum over-layer to the glass slide, whilst the 10 nm Pd layer acted as a diffusion barrier layer to ensure good electrochemistry by preventing the titanium from diffusing into the platinum. Finally, the platinum over-layer was evaporated to produce a coherent 100 nm thick electrode layer. After metal deposition, the microelectrode pattern was realised using a lift-off procedure in acetone, as shown in Figure 2.3.
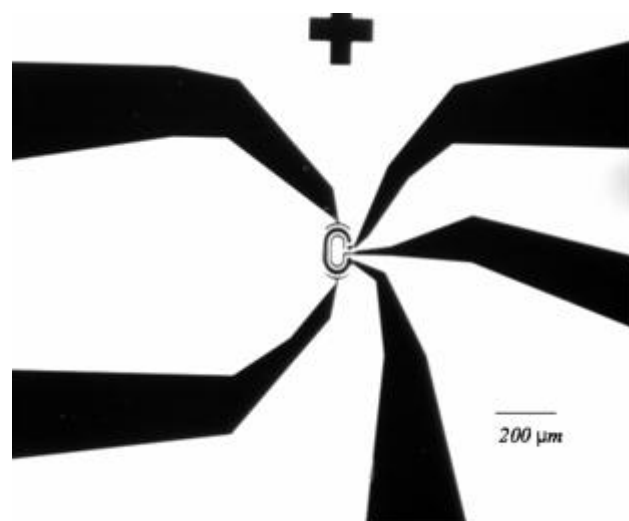
Figure 2.3 Microscope image of microfabricated electrode pattern from Design 1. Ti/Pd/Pt (10/10/100 nm) was deposited onto the glass substrate using an e-beam evaporator and patterned using photolithography to produce an electrode structure comprising five microelectrodes, three of which were used as an electrochemical sensor system, and two as stimulatory electrodes (see Figure 2.1 for details).

Alternatively, the platinum over-layer can be electrochemically deposited using a deposition solution containing 24 mM hexachloroplatinate in the presence of 2.1 mM lead acetate by the chronoamperometry method, as described in Equation 2.1. The electrode to be platinised was connected to the working electrode of the potentiostat, biased at −1.00 V using a coil of platinum wire as a common counter and reference electrode. The chronoamperometry response of platinisation on microelectrodes was shown in Figure 2.4. A greyish white layer of platinum was obtained at a deposition time of approximately 60 seconds, and a dense black layer of platinum was formed at a deposition time of approximately 100 seconds. Due to the electrochemical deposition time required, careful control was needed, otherwise excessive platinum might be deposited across the counter-electrode.
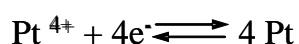
$$Pt^{4+} + 4e^- \rightleftharpoons 4\ Pt \qquad\qquad\qquad \text{Equation 2.1}$$
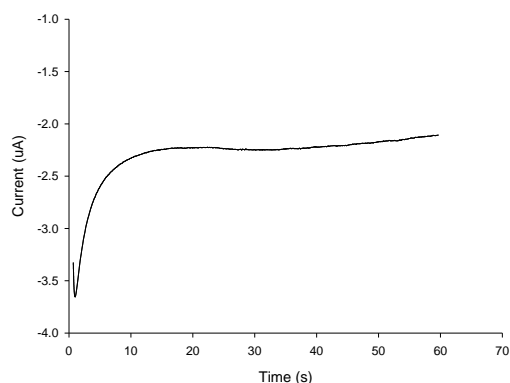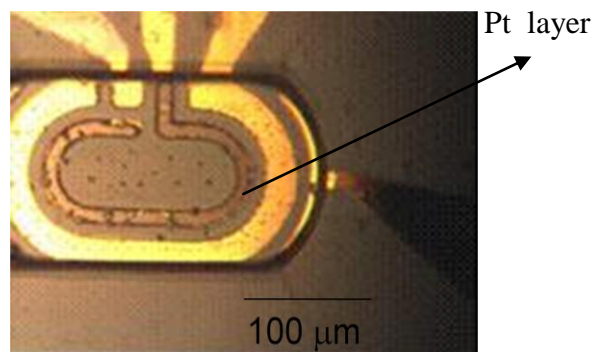
(a)   (b)

Figure 2.4 Platinum over-layer depositions: (a) Chronoamperometry response of platinisation on microelectrode biased at −1.00 V using a coil of platinum wire as a common counter and reference electrode (electrode area 1800 μm^2); (b) Microscopy image of the platinum layer upon the gold after 60s deposition.

2.3.2.3 Microreference Electrode

One of the platinum electrodes was modified with an Ag|AgCl layer to provide a reference electrode. The reason to choose Ag|AgCl as reference electrode is that the

electrode is easy to construct, inexpensive to manufacture and has stable potential. Both electrochemical methods and direct metal evaporation were used to deposit silver. Silver was electrochemically deposited onto the platinum electrode using chronoamperometry by connecting this to the working electrode lead and using a platinum wire as both counter and reference electrode. The silver layer was deposited on the microelectrode, biased at -.48 V from 300 mM $AgNO_3$ in NH_3 aqueous solution, which is made up by dissolving ca. 1.02g $AgNO_3$ in 20 ml NH_3 aqueous solution.

Alternatively, the evaporation of a layer of silver (300nm thick) was used. The mask design of an exact 20 μm × 20 μm square was made up in Corel, with white diagrams on a black background to create a positive image. The acetate mask was produced by printing the Corel file through a Postscript level 3 RIP, where it was then exposed onto Kodak 2000 ALD film via a Heidelberg Advantage Pro imagesetter, which in turn was developed to produce the final acetate mask, giving a resolution of 40,000 dpi. The acetate mask was converted to a ferric oxide copy for use. Silver was then coated using the same basic microfabrication process described above, in which the mask was used to define a 20 μm × 20 μm square over the reference electrode using an appropriate registration and alignment series.

The microreference electrode was structured following the lift-off in acetone. It was noted that the silver-coated device was usually soaked in acetone intact for 12 hours to complete the lift-off. After the deposition of Ag, a AgCl layer was galvanostatically deposited by applying +0.15 V in a solution of 0.1 M HCl (until the oxidation current decreased to background), producing a dense and coherent AgCl layer, as shown in Figures 2.5 and 2.6. Equation 2.2 is given below, describing oxidation at the microelectrode.

$$Ag + Cl^- \rightleftharpoons AgCl + e^-$$

(a)   (b)
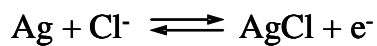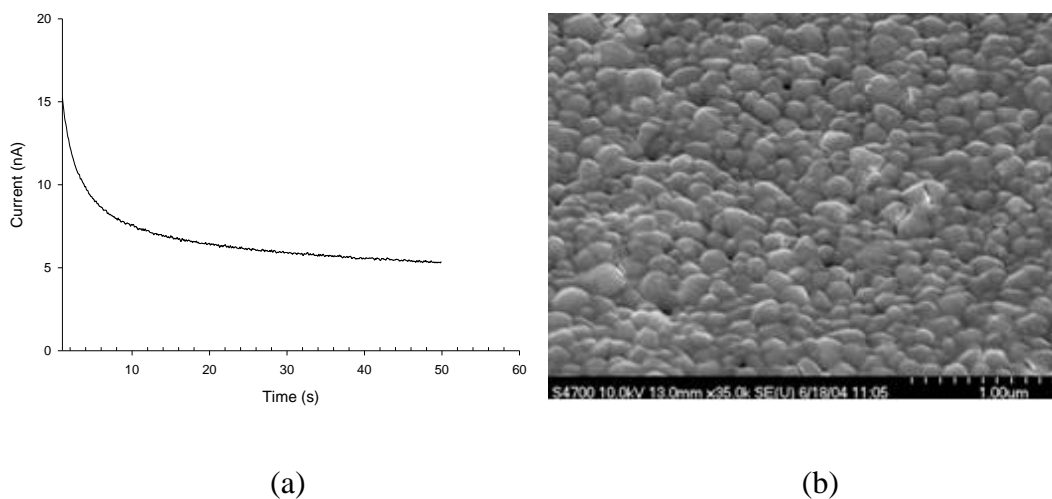
Figure 2.5 (a) Chronoamperometric response for AgCl deposition on microelectrode biased at 0.15 V using a coil of platinum wire as a common counter and reference electrode (electrode area 400 μm^2); (b) SEM micrograph of AgCl morphology at Ag|AgCl electrode surface.

100 μm

(a)   (b)
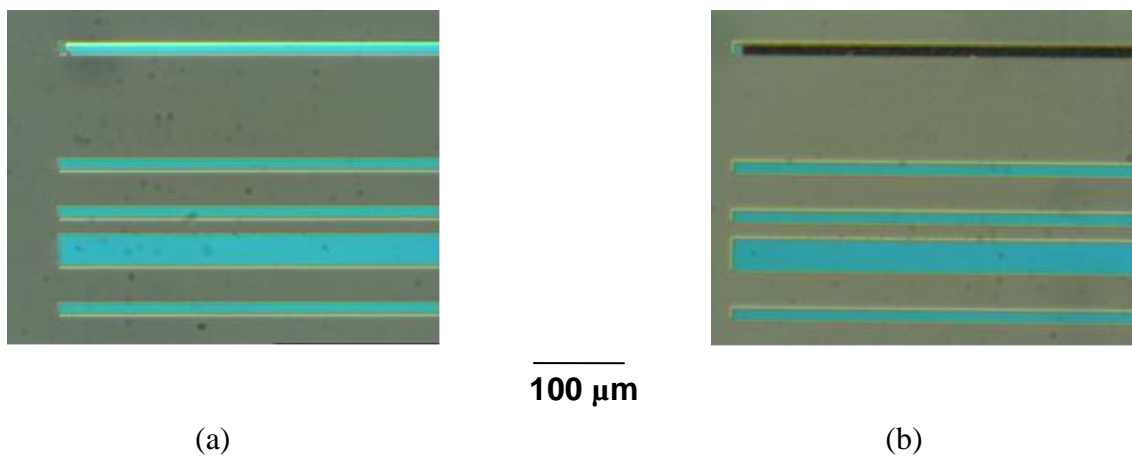
Figure 2.6 Micrograph image of Ag and AgCl morphology: (a) Before AgCl deposition, the top electrode layer was covered in shiny silver; (b) The electrode was coated with an intense dark silver chloride layer after deposition (by applying +0.15 V in a solution of 0.1 M HCl for ca. 400 s, coated electrode area 0.02 mm^2).

2.3.2.4 SU-8 Chamber

Figure 2.7 illustrates the whole microfabrication process of the SU-8 microchamber. Firstly, a layer of S1818 photoresist was patterned over the microelectrode array as a sacrificial layer, protecting the electrodes from fouling by residues from subsequent processes, using the same photolithography process described above.

A negative SU 2010 resist was then spun at 500 rpm at 100 rpm/s acceleration, to a final spin speed of 1000 rpm at an acceleration of 300 rpm/s, and held for a total of 30 seconds. Following that, the resist was soft-backed using a level hot plate to evaporate the solvent and densify the film, initially at 65 °C for 5 minutes and to a final 95 °C for another 10 minutes through ramping the temperature. The temperature is crucial to improve coating fidelity and reduce edge bead and resist-to-substrate adhesion. Later, lithography was performed using a contact aligner (400 mJ/cm², 350-450nm) with a 35 sec exposure time. The microchamber mask was carefully aligned to incorporate all microelectrodes under the microscopy. This exposure was optimised by conducting a series of tests of various exposure times. Following UV exposure, the resist was post-baked, initially at 65 °C for three minutes, then at 95 °C for five minutes, to selectively cross-link the exposed portion of the film, and then cooled down slowly. The gradual cooling minimises stress and cracking. Finally, the resist was subject to a developing process for five minutes and rinsed briefly with isopropyl alcohol, then dried with a gentle stream of nitrogen.
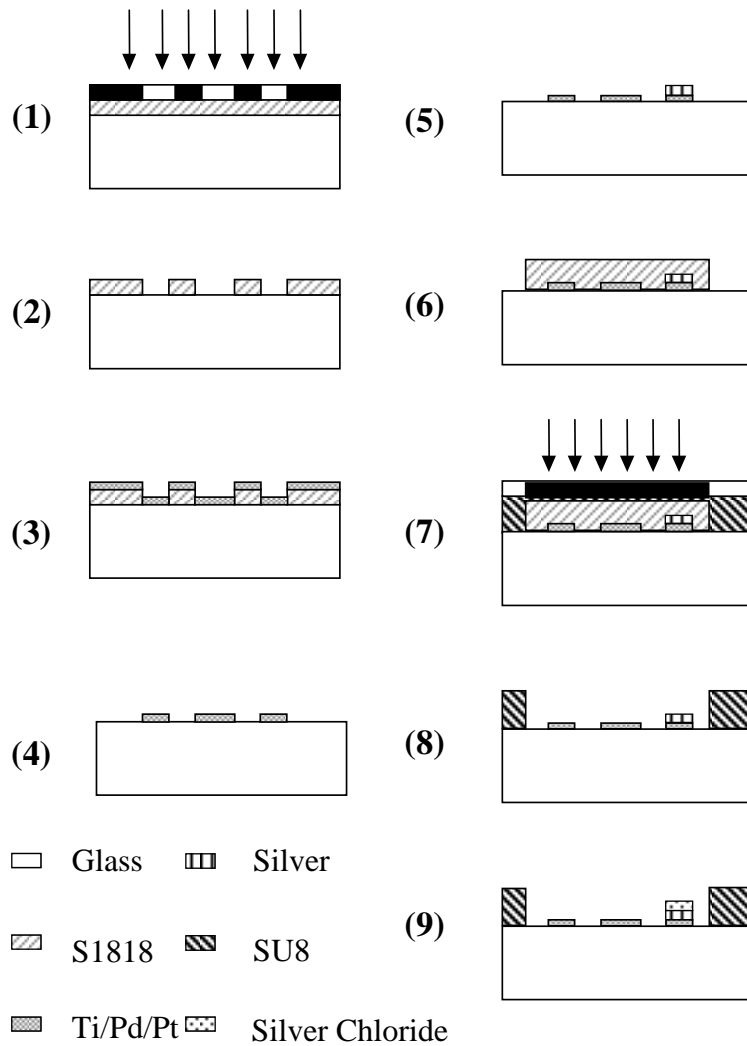
Figure 2.7 Schematic illustration of the major steps involved in the device fabrication: (1) the photoresist-coated substrate was exposed to UV radiation through a mask; (2) the photoresist was developed; (3) metals were deposited by evaporation; (4) the electrode pattern was generated by lift-off; (5) silver was deposited by evaporation; (6) spin-coating was used to generate an S1818 photoresist sacrificial layer; (7) the device was again exposed to UV radiation; (8) the SU-8 and S1818 layers were developed; (9) finally, AgCl was electrochemically deposited.

2.3.2.5 PDMS Multi-chamber

Poly(dimethylsiloxane), PDMS is a silicone rubber which was introduced in the 1960s and has unique properties that make it valuable in fabricating microscale devices: it is lightweight, hydrophobic, electrically insulating and exhibits fracture toughness. It is one of the most attractive materials for microfluidic structures, since these microstructures with sub-micron feature size can be replicated by simply pouring PDMS onto a master. PDMS was used to structure the microchamber in this work by spinning and washing it on

a sacrificial photosensitive mould such as an SU8 or AZ resist. Further, the hydrophobic nature of the PDMS surface was important, particularly when filling the microchamber and manipulating single cells. Figure 2.8 illustrates the process of microfabrication of the PDMS chamber, as detailed in the following steps:

2.3.2.5.1 AZ 4562 Photolithography

A thick positive resist (AZ 4562) was first spun at 2000 rpm for 10 sec to produce a 12 μm thick photoresist layer, then baked in the oven at 90 °C for 60 minutes, and was then exposed to UV using a mask aligner. The photomask was aligned to the microelectrodes under the microscope so that the microchannel pattern was transferred into the photoresist.

2.3.2.5.2 PDMS Preparation

The PDMS that was used for spinning is made by mixing a silicone elastomer with a cross-linker at a ratio of 10:1. It has been suggested that this mixture can be further diluted with Toluene to ease PDMS film lift-off [90]. However, in some cases, the toluene and PDMS do not mix (this is dependent on the type of PDMS) even after the mixture is sonicated for 2~3 minutes and flushed several times. Given the swelling ability of PDMS in organic solvents, N-heptane was used instead of toluene. The 4:1 diluted PDMS was spun on the device for 30secs at ca. 10000 rpm and cured in a 120°C oven for over 20 minutes to ensure that any N-heptane is removed. The device is then immersed in an oil bath for at least 24 hrs.

2.3.2.6 Finalised Device

The thin PDMS is thereby moulded against the photoresist master. Following immersion in oil, the final device arrangement is realised by applying a jet of acetone, removing the resist that remains. This latter step removes all residual resist from the microchannels and from the surface of the microelectrodes. Without the support of the photoresist, the thin film of PDMS covering the microchannels will collapse and is easily washed off. The

resist acts as a sacrificial layer as well as a master mould, enabling the appropriate contrast of a hydrophilic glass surface for the microchannel and hydrophobic top surface of PDMS between the channels.
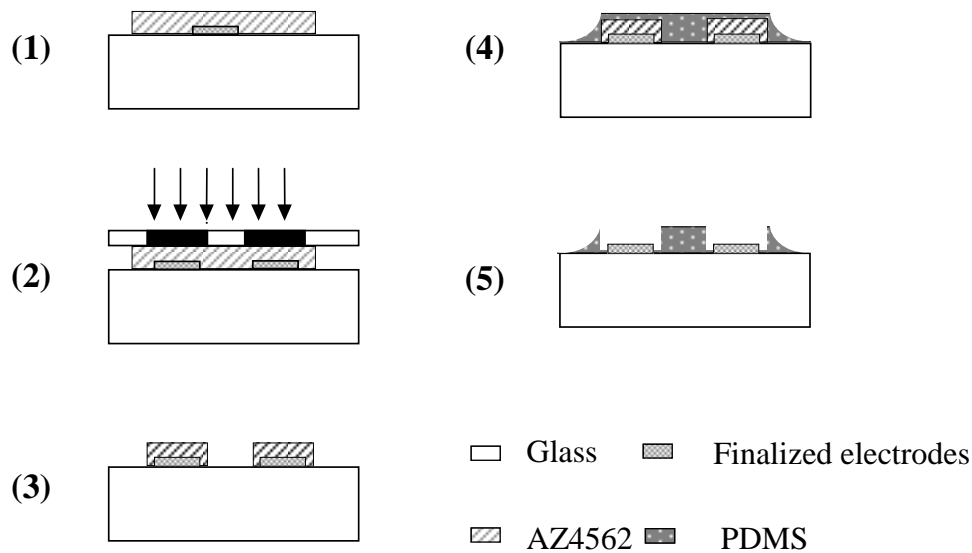
Figure 2.8 Illustration of the microfabrication processes involved in producing the PDMS chamber detailed above. This fabrication process starts with a finalised microelectrode pattern (sensor array), including structured Ag|AgCl reference (steps 1 - 5 and step 9 in Figure 2.7). (1) AZ4562 photoresist was spin-coated; (2) the photoresist-coated substrate was exposed to UV radiation through a mask; (3) thick AZ photoresist was generated by lift-off; (4) PDMS was spin-coated at a fast spinning speed (ca. 10000 rpm); (5) PDMS chamber was realised by acetone removal of AZ4562 following soaking in mineral oil.

2.4 Results and Discussion

2.4.1   SU-8 Microchamber

2.4.1.1 SU-8 Photoresist Microchamber

SU-8 is an epoxy-based, chemically amplified resist system for micromachining structures and other microelectronic applications. Due to its aromatic structure, with its highly cross-linked matrix, the exposed resist has thermal and chemical stability. The

materials have a low optical absorption in the near-UV range, and this high transparency means that high aspect ratio structures can be obtained when the polymer exposed using a standard UV aligner. In addition, a very wide range of thicknesses (from hundreds nanometres to millimetres) can be obtained with a single spin deposition by choosing from the SU-8 resist family. These characters of SU-8 make it ideally suited for single chamber fabrication for bio-analytical applications, particularly where both optical and electrochemical measurements are conducted, as in the present study.

However, SU-8 is a high stress material, and exhibits surface cracking caused by incomplete cross-linking when the exposure time dose is too low or the post-baking time is too short. Care must be taken to ensure optimised exposure and baking protocols. For film with a thickness of 20 μm, exposures of 90mJ cm^{-2} were found to produce good integrity (as evidenced by examination under SEM). Figure 2.9 shows photographs and SEM images of typical samples of final devices fabricated with SU-8 microchambers.
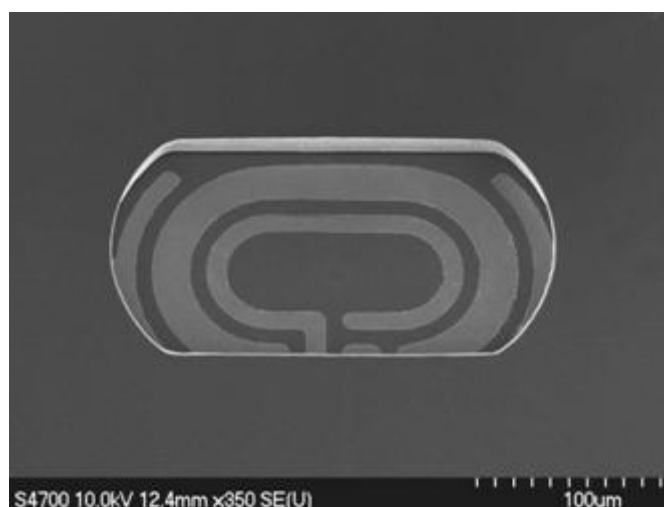
Figure 2.9 SEM of finalised device integrating five microelectrodes within an analytical microchamber fabricated using SU-8. The final realised device comprises five functional microelectrodes integrated within an SU-8 microanalytical chamber (with a thickness of 20 μm).

2.4.1.2 SU-8 Residue on Electrodes

In this study, SU-8 2010 was used to structure the microchamber, giving a geometry whose size was compatible with single cardiomyocytes.

Examination using an SEM, or by surface profilometry, revealed a residue on the microelectrodes after processing. This severely inhibited subsequent electrochemical studies due to the changed surface area of the microelectrode. In order to prevent Pt electrodes being fouled by SU-8 photoresist residue remaining after fabrication of the microchamber, a number of methods were explored: nichrome (NiCr) was initially deposited as a sacrificial layer to remove the SU-8 residue when nichrome was chemically etched. However, the wet etching solution also removed the NiCr under the SU-8 surface, undercutting the resist. Additionally, the etching chemical would damage the Ag layer deposited on the Pt. As an alternative solution, a layer of thin S1818 (1.8 µm thick) photoresist was patterned using the same photolithography process described above, which forms a sacrificial layer over the microelectrode, protecting the electrodes from fouling by residues from subsequent processes. Figure 2.10 shows examples of SU-8 microwells with residue, and without residue due to the protective layer used in the fabrication procedures.
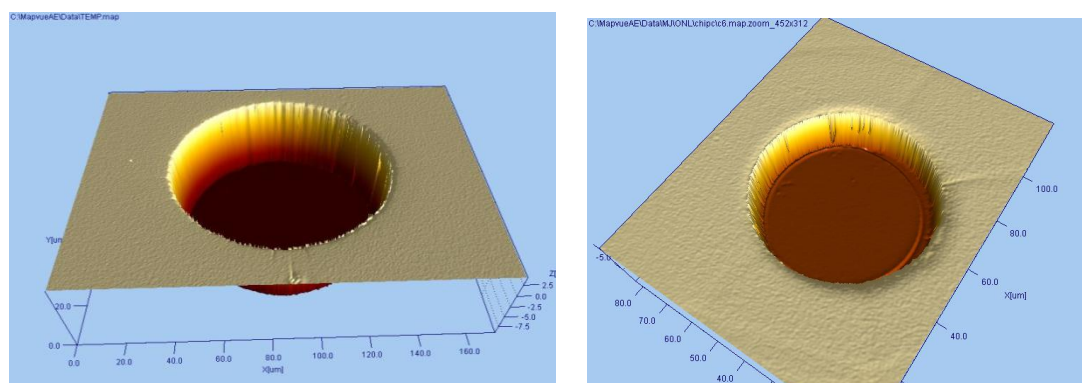
(a)   (b)

Figure 2.10 Surface profilometry of SU-8 microwells: (a) Clear surface on the bottom of the chamber when using a sacrificial layer; (b) SU-8 residue remains on the bottom of the chamber.

2.4.2   PDMS Microfluidic Chamber Array

2.4.2.1 PDMS Microchamber

In contrast to SU-8, which is a photoactive resist, PDMS is a polymer that readily lends itself to imprinting and moulding into small feature size and/or high aspect ratio microstructures. The curing of PDMS involves the addition of platinum-containing curing agents into a siloxane oligomer base followed by the heating of the pre-polymer mixture to 60-120°C for several hours. Multiple organometallic linkages ($-Si-CH_2-CH_2-Si-$) are created, forming three-dimensional polymeric networks. In this way, PDMS structures can be formed by moulding the prepolymer against a master, followed by curing and release from the master. Due to the versatility and ease of use of PDMS, enclosed PDMS channels are commonly used in microfluidic systems.

Unlike enclosed PDMS channels released from the master (see Chapter 6), in this study, a thin layer of prepolymer (1-2 μm) was moulded against the AZ photoresist master, directly forming an open chamber array, without release from the master. The thin film of PDMS covering the AZ resist master collapsed and was washed off by applying a jet of acetone, leaving a PDMS open microfluidic chamber. The PDMS film covering the bulk electrodes also served as an insulating layer to avoid short-circuits of the connecting leads through the buffer solution. After finalising the device (Figure 2.11), the PDMS channels were immediately filled with the aqueous buffer solution. The hydrophobic surface of PDMS wall was rendered more hydrophobic by immersion in a layer of mineral oil for days, which helped the cells be directed into their channels rather than adhere on the top surface of PDMS (see Chapter 5).
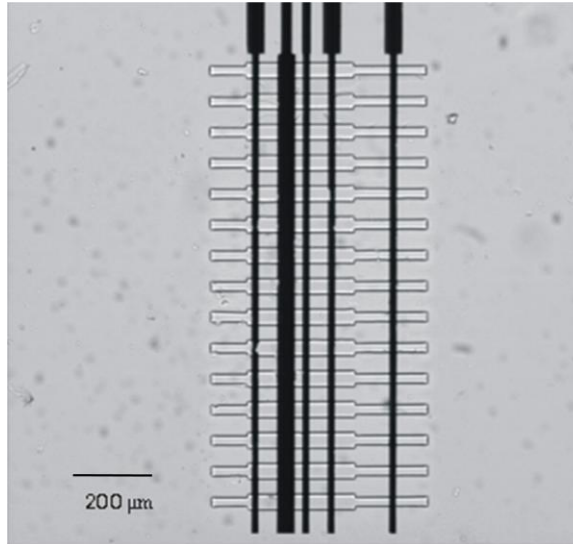
Figure 2.11 Microscopy image of finalised device with sensor array integrated within PDMS microchannel.

2.4.2.2 PDMS Chambers with Different Thicknesses

As discussed above, the thickness of the AZ resist master determines the thickness of the PDMS chamber. AZ resists with a wide range of thicknesses were achieved by optimising spin speeds and the use of multiple coatings, subsequently resulting in an equally wide range of PDMS channel depth and chamber geometries. However, there are difficulties in that by increasing the thickness of the film, the exposure dose has to be adjusted to provide sufficient energy at the bottom of the photoresist; otherwise, the pattern will not be well defined. In extreme cases, it became almost impossible to expose the resist properly and high exposure doses (above 1000 mJ/cm²) had to be applied.

On the other hand, under these conditions of high exposure dose, unwanted side effects also appear: the dose at the surface of the photoresist becomes too high and induces cross-linking of the resist, making it hard to lift off. A standard resist would also generate too much nitrogen during exposure, which, trapped in the thick layer, cannot diffuse fast enough and may lead to lifting of the resist.

In this study, a series of photolithography methods was used to pattern AZ photoresist films of varying thickness as master structures to mould PDMS microfluidic channels. When using high film thicknesses, some special guidelines have to be noted: after each coating, the resist was kept at room temperature for at least 15 minutes to allow most of

the solvent to evaporate before it is put into an oven to prebake. Otherwise, the resist surface will form bubbles and lift the resist film. The development process also has to be adapted for high film thickness. The background to this is the fact that even heavily overexposed positive photoresists only have limited dissolution rates (there is saturation at values in the order of 100 nm/s). Table 2.1 shows the optimised fabrication profile of AZ 4562 with thicknesses of 12 µm, 24 µm, and 36 µm.

After defining the thickness of the AZ resist, diluted thin PDMS was spn-coated and thereby moulded against the photoresist master to realise the open PDMS channels by applying a jet of acetone to remove the remaining resist, as detailed above. The dimensions of chambers and channels were checked using surface profilometry, DekTak ST (Veeco Instruments Inc., USA), as Figure 2.12 illustrates. PDMS chambers with varying heights/volumes have an effect on cell placement and monitoring, as will be discussed in Chapter 5.

Table 2.1 Protocol to fabricate thick AZ 4562

Thickness	Spinning Resist (1st layer)	Multiple coating (2nd layer)	Baking time	Exposure time	Developing time
12 µm	1300rpm 30s	N/A	60 min at 90°C oven	60 s	3-4 min
24 µm	2000rpm 10s	2000 rpm, 10s; 2 min hot plate baking at 85°C in between	60 min at 90°C oven	140 s	8-10 min
36 µm	1500rpm 10s	1500rpm, 10s with no baking in between	60 min at 90°C oven	200 s	18-20 min

2.4.3   Evaluation of the Device Fabrication

A number of factors must be taken into consideration when using a microfabrication or micromachining protocol for hybrid electro-analytical sensors, among which the important issues are the quality of the device and whether it can be reproducibly and reliably fabricated using the optimised protocol, as well as the character of the metals used as stable electrodes.

2.4.3.1 Microchamber

The physical characterisation of the device can generally be performed using surface profilometry. Comparison of the surface profiles (Figure 2.12) indicates that the sidewalls of the PDMS chamber in (b) have a much higher aspect ratio than those in (a). These cracked sidewalls (a) are due to the underexposure of the AZ thick photoresist. Once the optimised protocol was shown (see table 2.1), the microchamber should be produced reliably and reproducibly with a high aspect ratio and smooth vertical sidewalls, as shown in (b). This is important when considering the acute angle of the microcapillary used for access to the microchamber when microinjection is being performed under the microscope, see Chapter 3.

(a)
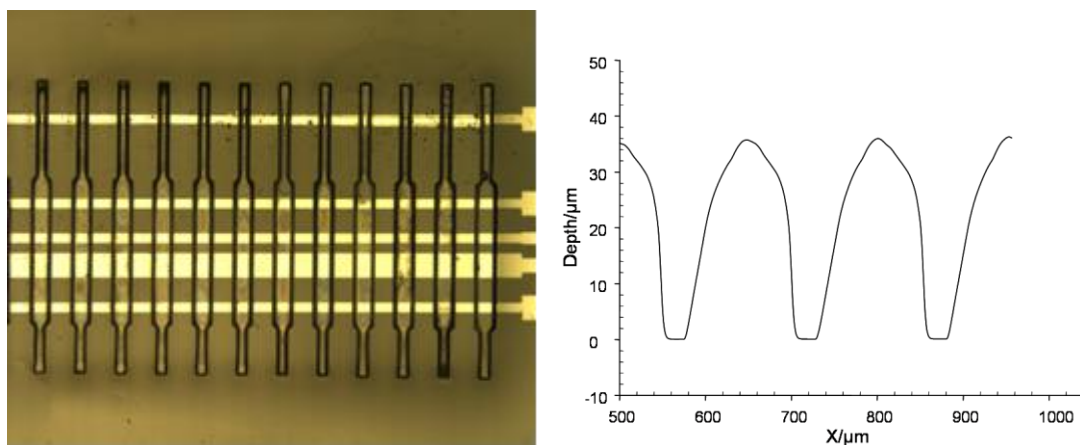
(b)
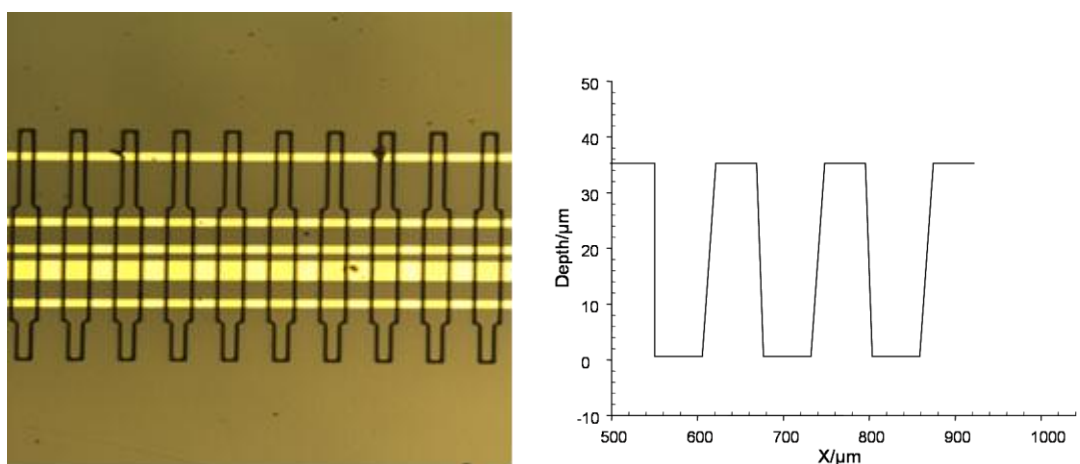
Figure 2.12 shows representative PDMS chambers: (a) photographical image and surface profile of a typical chamber array with cracked sidewalls due to the underexposure of the AZ thick photoresist. (b) photographical image and surface profile of a typical chamber array with smooth vertical sidewalls, giving a much higher aspect ratio at the optimised conditions.

2.4.3.2 Microelectrode

The platinised electrodes, which act as working electrodes, possess a large surface area and are highly catalytic for electrochemical detection processes (with a reduced overpotential for the oxidation of H_2O_2, for example.) This enhanced surface area could increase the signal/noise ratio significantly compared to the planar platinum surface, due to the increased surface area [93]. However, in order to simplify the fabrication procedure and to implement a less time-consuming protocol, the use of a 100 nm Pt sputter was investigated. Given the sensor sensitivity from the planar, a platinum surface is sufficient (see Chapter 3). As a consequence, all subsequent experiments throughout the electrochemical analysis were carried out with a 100 nm thick sputtered platinum microelectrode.

The reference electrode, which has been electrochemically deposited, has a rougher surface. Figure 2.13 gives examples of Ag|AgCl electrodes with different geometries, which were all produced using the same electrochemical methods, with the deposition of a crystallised silver layer followed by chloridisation. Due to the crystallised structure of Ag|AgCl electrodes, the enhanced surface area would improve the stability of the open circuit potential of the reference electrode, which is crucial for the reproducibility of the biosensor. The microelectrodes were fully evaluated using electrochemical characterisation, which will be detailed Chapter 3.

(a)   (b)
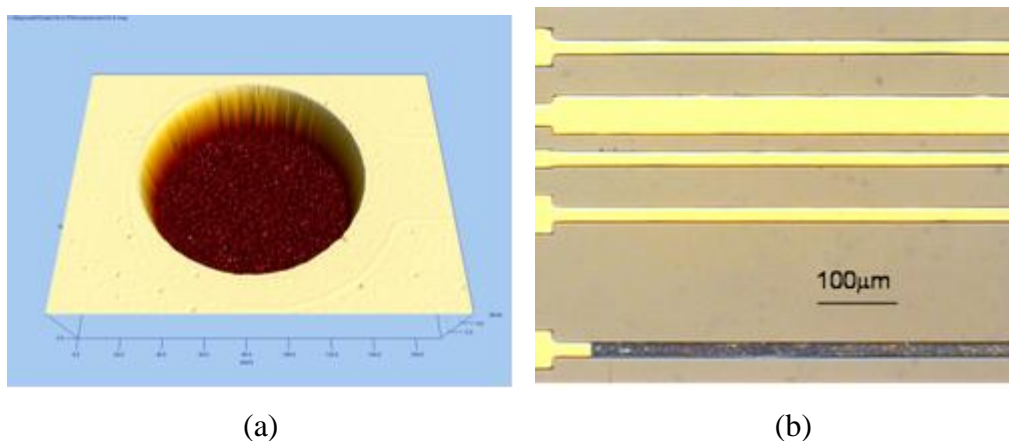
Figure 2.13 Examples of Ag|AgCl electrodes of different geometries: (a) microwell, (b) rectangle, which are both produced using the same electrochemical methods, using the deposition of a crystallised silver layer followed by electrochemical chloridisation, giving a 1 μm-thick Ag|AgCl electrode.

However, in the design of single microfluidic chamber (see 2.3.1.2), the confined reference electrode was small, (considering the poor biocompatibility with the heart cell, as will be discussed in Chapter 5), with an area of 20 x 20 μm^2. The distance between the reference electrode and either the working electrode or the counter electrode was 10 μm. At such small scales, much care is needed; otherwise, the silver can be deposited across other electrodes during electrochemical deposition. Therefore, to simplify the fabrication process, a layer of silver (300 nm thick) was evaporated on the Pt microelectrode and followed by chloridisation, used as a microreference in the SU-8 device.

2.5   Conclusion

Two designs for the following study of single beating cardiomyocytes have been proposed. One involves five microelectrodes, fully integrated within a microfluidic SU-8 chamber. The other has a sensor array integrated within a poly(dimethylsiloxane) (PDMS) microchannel array. Both devices have a five-electrode system comprised of one pair of pacing microelectrodes, used for the field stimulation of the cell, and another three microelectrodes configured as an electrochemical biosensor, containing a working electrode, a counter electrode and an internal Ag|AgCl microreference electrode.

The devices were fabricated using photolithography to give a high aspect ratio SU-8 well and a PDMS chamber array. A thin layer of photoresist was used in fabricating the SU-8

chamber (height of 20-25µm), as a sacrificial layer over the microelectrodes to protect them from fouling from SU-8 residues. AZ photoresist films of varying thicknesses were patterned as master structures to form PDMS microfluidic chambers with different thicknesses (ranging from 12µm to 36µm). Both devices are evaluated to give reproducible fabrication.

Chapter 3 Device Characterisation and Calibration

3.1 Introduction

L-lactate is of one of the most significant makers in biotechnology and biomedicine, and an automatic, sensitive and fast method for its detection is required in clinical, food and bioprocess analysis. Amperometric measurements of lactate often involve an enzyme-linked electrochemical sensor where lactate oxidise (LOD) catalyses the oxidation of lactate in the presence of oxygen to pyruvate, with the production of H_2O_2, which can be amperometrically detected.

Lactate is also one of the most important cellular metabolites, being an important fuel for the heart under aerobic conditions, and must be transported into the cell. In contrast, in conditions of hypoxia or ischaemia (e.g. infarction or cell death), the heart uses a process called glycolysis to fulfil the increased demand for ATP for ionic homeostasis and contraction; lactate production and efflux from the heart cell are increased during this process. Lactate levels can therefore be monitored to indicate the health of a cell, because diseased cells, or those in which oxygen supply is restricted, tend to produce larger amounts of lactate.

This chapter first describes the use of ferrocene monocarboxylic acid (FMCA) as a model redox compound for investigating the electrochemical characterisation of the integrated sensors. The sensitivity, response time and calibration curves for the amperometric detection of L-lactate using macro-volume solution were investigated. A pL-scale dispensation technology enabling delivery of extremely low volume (>1.3 pL) aliquots of lactate to the analytical system is also described. Using this dispensation system, 4.8 fmol lactate was amperometrically measured. It is necessary for the integrated fabricated sensor to develop a method for enzyme immobilisation with the potential to automate the continuous electrochemical analysis for *in vitro* application. The pL-scale lactate was electrochemically calibrated with a fast response time and low sensitivity, which, in future, will enable the real-time dynamic electrochemical measurements of lactate within low volumes (e.g. from single heart cells). The basic kinetics and shelf life of this enzyme-immobilised integrated micromachined sensor system were also investigated.

The opening sections of this Chapter will provide a brief synopsis of some of the underlying systems, theories and practicalities that govern the electrochemical techniques used throughout this and other chapters.

3.1.1 Three-electrode Configuration and Electrochemical System

The electrochemical cell in which the electrochemical experiment is carried out consists of a working electrode, a reference electrode and a counter (auxiliary) electrode, as illustrated in Figure 3. 1. The reference electrode (RE) should have low impedance, be capable of maintaining a constant potential and be easy to assemble and maintain. In practice, the most commonly used reference electrodes for aqueous solutions are Ag|AgCl electrodes. The Ag|AgCl electrode consists of metallic Ag coated with AgCl in contact with an aqueous solution containing a fixed concentration of chloride ions. In saturated NaCl this has a potential Eº of 0.197 V at 25°C versus the NHE, in electrochemical terminology (early in electrochemical techniques, the normal hydrogen electrode (NHE) was accepted as a standard).

The shortcoming of two-electrode system includes the difficulty for reference electrode to maintain a constant potential while passing current to counter redox events at the working electrode, which makes three-electrode system necessary with the auxiliary/counter electrode (CE) used to allow the current to flow through the electrochemical cell without affecting the reference potential. In the present study, two additional stimulation electrodes are placed so that a flow of ions may also result from applying the electrical field. The counter electrode has been employed only to supply the current between the working and counter electrodes, so that the stimulation electrodes are isolated from electrical circuit of the electrochemical one.

The working electrode (WE) is where the redox reaction or charge transfer takes place (and the opposite redoc will occur at the CE). The reduction or oxidation at the WE surface, at the appropriate applied potential, results in mass transport of the new substance to the electrode surface and the generation of a current. Within a quiescent system, the process is generated by diffusion, with new redox species moving down a concentration gradient to be depleted volume at the WE. By controlling the surface potential of the WE and simultaneously measuring the amount of current passing through it, information can

be obtained about the charge transfer processes that occur at the interface of the electrode surface and solution. The relationship between the applied potential and the behaviour of the redox process at the WE surface, which forms the basis for the application of various electrochemical techniques, can be described using the Nernst equation, as follows:

$$E = E° + \frac{RT}{nF} \, In \frac{C_{Ox}}{C_{Red}}$$

Equation 3.1

Where "Red" is the reduced form of an electroactive molecule at the WE surface, "Ox" is the oxidized form, E is the potential applied to the WE surface, E^o is the standard potential for the redox couple, R is the molar gas constant (8.3144 J mol^{-1}K^{-1}), T is the absolute temperature (K), n is the number of electrons transferred and F is the Faraday constant (96,485 C mol^{-1}).
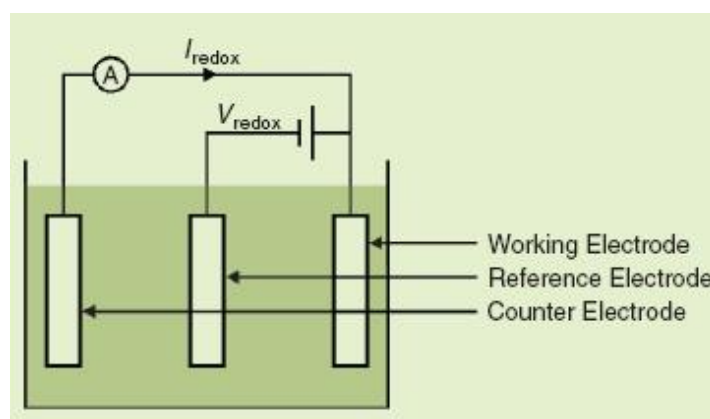
Figure 3.1 A schematic of the three-electrode system setup. In the voltammetric techniques (wherein voltage is controlled and current information is obtained), a redox potential (Eredox) is applied between the working and the reference electrode, and the resulting current is measured between the counter and working electrodes.

3.1.2   Voltammetric Methodology

While various types of voltammetric techniques may be used in different models, their fundamental principles and applications derive from the same electrochemical theory.

Here, we incorporate the kinetic concept, which links the variables of current, potential and concentration, to fully account for the observed electron transfer processes at the WE surface, as described by the Butler-Volmer equation:

$$j = -k°C_{Red}(0, t)exp \left[\frac{(1-\alpha)n_a F(E-E°)}{RT}\right]$$

Equation 3.2

where j is the flux of redox, $k°$ is the standard rate constant for electron transfer, α is the transfer coefficient, n_a is the number of electrons passed in the rate limiting step in the electrochemical reaction, F is the Faraday constant, E is the electrode potential, and C_{Red} is expressed as a function of time and distance. Described in words, the flux (contributing to the current intensity) is proportional to the electron transfer rate, the concentration of unoxidized species and the amount of overpotential (E-E°) applied to the WE surface.

In most cases, the current flow depends directly on the flux of material to the electrode surface. When the electroactive reactant is being "consumed" or transformed by electron transfer at the WE, a concentration gradient will form. Given a high exchange current density and the reaction rate (solely mass-transfer control), the current may become limited by the rate at which the reactant arrives at the electrode by diffusion. The diffusion-limited current density is therefore given by Fick's first law governing diffusion of reactants to the WE:

$$i = -FD\left\{\frac{\partial C}{\partial x}\right\}$$
Equation 3.3

Where F is the Faraday constant (C mol^{-1}), D is the diffusion coefficient (cm^2 s^{-1}), $\frac{\partial c}{\partial x}$ is concentration gradient (mol cm^{-4}) and i is current density (C cm^{-2} s^{-1}).

According to the Nernst diffusion-layer concept, the concentration gradient is assumed to be linear, namely, $\frac{\partial c}{\partial x} = \frac{C - C°}{\delta}$, where δ is defined as a certain thickness of the diffusion layer and increases with increasing electrolysis time; C^0 represent the concentration of analyte at the electrode surface. Therefore, combining these gives an expression for the diffusion-limited current density:

$$i = -FD\left\{\frac{C_{bulk} - C_{X=0}}{\delta}\right\}$$
Equation 3.4

($x=0$, indicates the maximum limited current density)

This above diffusion-limited current model assumes a high redox reaction rate, and applies to only diffusion controlled situations. In fact, in addition to diffusion, mass

transport can occur by migration or convection. Migration is the movement of a charged ion in the presence of an electric field, and convection is the movement of the electroactive species by thermal currents, or by stirring the solution. Migration and convection will account for non-Faraday current and must be controlled accurately or eliminated. This is particularly important in the context of the high electrical field across the electrodes, used to stimulate the heart cell.

Though the above concepts apply to all electrochemical techniques in which potential is controlled and the current is measured, the actual current is a more complex value affected by some additional factors, such as the size, shape and material of the electrode, the solution resistance, the cell volume and the number of electrons transferred. The various aspects of i–E behaviour during experiments will be given in more detail later, when a particular i–E curve is discussed.

3.1.3 Amperometry and Cyclic Voltammetry

Electrochemical techniques such as cyclic voltammetry and amperometry, which employ microelectrodes, are becoming recognized as the tools of choice for intracellular and extracellular monitoring at the single-cell level. The significant advantages of electrochemical techniques for intracellular monitoring include sub-millisecond temporal resolution, chemical identification of the substance being detected, non-intrusive measurements at the single-cell level, high sensitivity (detection of a few thousand molecules has been achieved even for sub-cellular events [127]) and high spatial resolution (multiple membrane regions have been examined simultaneously on an individual cell [128, 129]).

Amperometry is a technique where the potential between the WE and the RE is adjusted to a constant value. The potential is selected to be sufficiently positive or negative such that electroactive analytes are driven to the WE surface quickly, and this approach is therefore considered to be diffusion controlled. The resulting current is then measured with respect to time to observe changes in concentration that occur at the electrode surface. As discussed above, the limiting current may be related to the concentration of analytes. In amperometry, the potential at which the oxidation is diffusion controlled will

be determined by increasing the potential of the electrode until a limiting current is reached.

In cyclic voltammetry, the potential is periodically scanned against time in the form of a triangular wave, from potentials where no oxidation reactions occur to more positive potentials until the current measured is stable (diffusion controlled). The resulting current that flows between them in the solution is measured. Cyclic voltammetry provides a current-voltage curve where the characteristics of the particular molecules present at the electrode surface can be recognised.

3.1.4   Derivation of Butler-Volmer Equation and Tafel Plot

The Butler-Volmer equation for a one-step, one-electron process is simply derived as:

$$i = i_0\left[e^{-\alpha f\eta} - e^{(1-\alpha)f\eta}\right]$$ Equation 3.5

where i_0 is the exchange current, α is the transfer coefficient; $\eta = E - E_{eq}$ i.e. the over potential, E_{eq} is the equilibrium potential; $f = F/RT$, F is the Faraday constant, R is the gas constant and T is the absolute temperature. For small values of x, the exponential e^x can be approximately as $1 + x$; hence, for sufficiently small η, which means that the applied potential is close to the equilibrium potential, the equation can be expressed as:

$$i = -i_0 f\eta$$ Equation 3.6

In this case, the net current is linearly related to the over-potential in a narrow potential near E_{eq}. At large values of η, one of the bracketed terms in the equation becomes negligible. At large negative over-potential, the equation can be expressed as $i = i_0 e^{-\alpha f\eta}$ at large positive over-potential, the equation can be expressed as $i = -i_0 e^{(1-\alpha)f\eta}$.

The plot drawn from the Butler-Volmer Equation is known as a Tafel Plot, and gives the fundamental relationship between the current flowing and the applied voltage. This plot shows how the current will respond to changes in potential, and can be used to evaluate electro-analytical kinetic parameters, such as α and η.

3.2 Methods and Materials

3.2.1 Cyclic Voltammetry and Electrochemical Characterisation using FMCA

As described above, cyclic voltammetry provides a current-voltage curve where the characteristics of the particular molecules present at the electrode surface can be recognised. Ferrocene monocarboxylic acid (FMCA) has a reversible electrochemical redox couple, ferrocene/ferrocenium. An electron can be removed from the FMCA molecule by the electrode, causing the molecule to be oxidised. Alternatively, the oxidised form of FMCA in solution may accept an electron from the electrode and be reduced to the original molecule. Therefore, FMCA can be used as a model redox compound to investigate the electrochemical characterization of the integrated sensors.

3.2.2 Amperometric Detection and Calibration of Hydrogen Peroxide and L-lactate

The integrated sensor devices were firstly cleaned by cycling in acid: the microelectrode was cycled in 0.5 M H_2SO_4 between -0.2 V and +1.2 V until a steady-state voltammogram was observed. Water-insoluble FMCA was first dissolved in methanol and then dropped into the stirred phosphate buffered saline (PBS) solution at different final concentrations. The SU-8 chamber was covered using a 10 µl FMCA solution. The device was then characterised by low to high concentrations of FMCA, being washed with distilled water between experiments. Cyclic voltammetry experiments were all carried out between 0 V and 0.6 V at appropriate scan rates. The internal Ag|AgCl microreference could also be characterised by comparing to the external true Ag|AgCl reference using an external microdisk gold electrode as the working electrode.

3.2.2.1 Reaction Principle

Amperometric assays, where the potential between the WE and the RE is adjusted to a constant value, allowing electroactive analytes to be oxidized or reduced, provide temporal resolution of the addition of analytes, while the resulting current is associated with the concentration of the analytes.

The amperometric approach to L-lactate is based on the enzymatic oxidation of the analytes with lactate oxidase (LOD) according to the reaction:

$$\text{Lactate} + O_2 \xrightarrow{\text{LOD}} \text{Pyruvate} + H_2O_2 \qquad\qquad \text{Equation 3.7}$$

The hydrogen peroxide generated in this reaction is electrochemically oxidised on a platinum electrode, which is polarised at 0.64 V *vs.* Ag|AgCl microreference electrode. This equation also forms the basis for the amperometric detection of hydrogen peroxide.

$$H_2O_2 \longrightarrow 2H^+ + O_2 + 2e^- \qquad\qquad \text{Equation 3.8}$$

$$+640\text{mV} vs. \text{Ag|AgCl}$$

3.2.2.2 Measurements of Bulk and pL-scale Solution

In a standard bulk solution method, the device, with or without enzyme immobilisation, was soaked in 5 ml stirred PBS without LOD (or with 100 units/ml LOD) within a 10 ml beaker. When the background current had reached a steady state, aliquots of lactate were successively injected into the bulk solution. The final concentration of lactate could then be calculated. A 10 µl drop of solution (with or without LOD) to cover the microchamber was used to model the bulk solution used for measurements. In this case, 1 µl of 1 mM lactate was injected into the solution to give a final lactate concentration of ~ 0.1 mM. The lactate concentration could be readily determined via the electrochemical oxidation of hydrogen peroxide. The response to hydrogen peroxide at different applied potentials was investigated. The optimum potential was finally held at +640 mV (*vs.* Ag|AgCl microreference). The device microchamber was filled with PBS buffer using the method

described in Chapter 2. The dispensation of pL-lactate was made on a home-made microfluidic dispensation system.

3.2.3 Enzyme Immobilization

Immediately prior to enzyme immobilization, the microfabricated electrochemical electrode was cleaned by scanning the applied potential between -1 V and +1 V in 100 mM H_2SO_4 at 1 V/s, followed by washing in ultrapure water. The enzyme (20 μl solution containing 200 units/ml in PBS, pH 7.4) was pre-adsorbed onto the electrode surface by incubation overnight at 4°C. A poly(o-phenylenediamine) film was then deposited on the electrode to entrap the pre-adsorbed enzyme using cyclic voltammetry by scanning the applied potential at a rate of 50mV/s for 6 minutes between 0.0 and +0.80 V vs. Ag|AgCl microreference in a supporting electrolyte solution of 50 mM PBS containing 50 mM KCl and 30 mM o-phenylenediamine. The growth of non-conducting polymers is self-limiting, and typically the resultant current falls to a steady state value within a minute, producing a film of defined thickness and composition. After the polymer growth was completed, the device was washed thoroughly in the working buffer and stored in PBS buffer at 4°C.

3.2.4 Picolitre Dispensation System

3.2.4.1 Experimental Set-up

A schematic representation of the whole analytical set-up is given in Figure 3.2, comprising a low current potential, with data collected using a PC, an inverted microscope and a microinjection system, a schematic diagram of which is described in Figure 3.3. Briefly, R1, R2, R3 are pressure regulators, G1, G2 are pressure gauges, V1, V2 are needle valves and C1, C2 and C3 are three-way connectors, which both allow flow across selected ports, ESV1, ESV2 are respectively electric solenoid valves for left and right injection and balance, Port 1, 2, 3 are used to choose off/on status of the injection. More details of this microinjection system were described elsewhere [110].
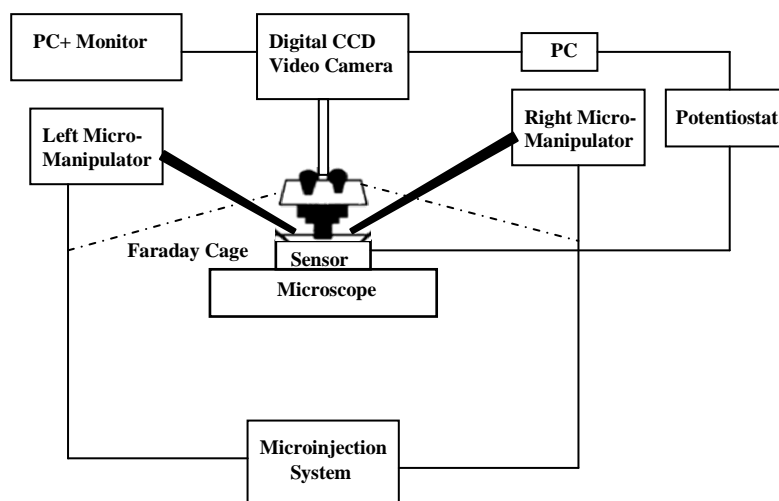
Figure 3.2: Schematic diagram of the whole electrochemical analytical system, comprising a low current potential, with data collected using a PC, an inverted microscope and a microfluidic dispensation system.
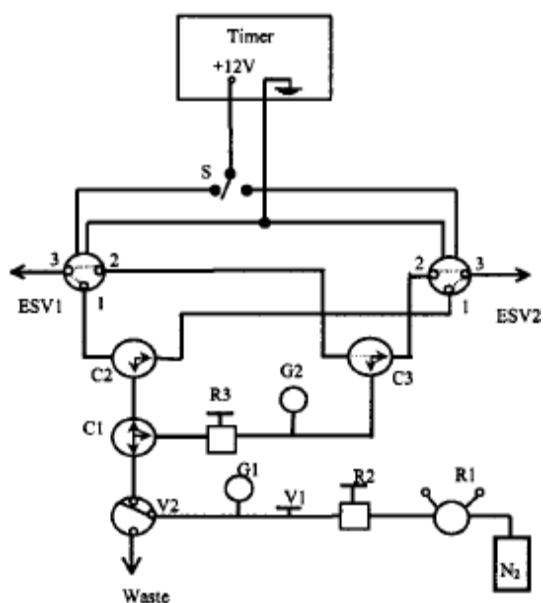
Figure 3.3: Schematic diagram of the microinjection system, in which R1 is the gas cylinder regulator assembly, R2 is a 0-60 psi pressure regulator, R3 is a 0-10 psi pressure regulator, V1 is a needle valve, V2 is an SMC three-port valve that allows flow across selected ports, G1 is a 0-60 psi pressure gauge, G2 is a 0-10 psi pressure gauge, C1 is a three-way connector, C2 and C3 are three-way connectors (which allow flow across selected ports), S is a switch, ESV1 is an electric solenoid valve for left injection (timer pulse on, 1 T 3) and balance (timer pulse off, 2 T 3), ESV2 is an electric solenoid valve for right injection (timer pulse on, 1 T 3) and balance (timer pulse off, 2 T 3). Port 1 and port 3 of the electric solenoid valve (ESV1 or ESV2) are open for dispensation when the timer pulse is set on; port 2 and port 3 of ESV1 or ESV2 are open for the balance process when the timer pulse is switched off. The left or right process is controlled by selecting the left or right ports of C2 (for left or right dispensation) and C3 (for left or right balance), as well as the left or right of S.

3.2.4.2 pL-Scale Solution Dispensation

Prior to pL-scale solution dispensation, the microchamber was first cleaned by dry etching. A thin film of mineral oil was dispensed onto the microchamber to prevent buffer evaporation. A 0.3 µl droplet of solution was placed directly onto the microchamber area. The chamber area was then covered with 30 µl mineral oil constrained within an epoxy ring wall (diameter 8-10 mm, width 2 mm, height 1 mm). The pipette, without filament (end bore 5~10 µm), was inserted into the droplet and allowed to fill by capillary action. The rate of filling was slow, such that by carefully inserting and removing the pipette, the volume of the buffer could be reduced to that of the chamber. To dispense pL-scale solution, a filament pipette with a fine tip (bore diameter 500~700 nm) was back-filled with solution. An injection pressure of 20 psi was used to dispense pL volumes. A one-shot timer was used, which could be set between 10ms and 99.99s to enable the required volume of fluid to be dispensed.

3.2.4.3 Calibration of pL-scale solution dispensation

To calibrate the volume dispensed by the system, the standard additions were carried out as follows. A fine capillary tip filled with PBS buffer (inner diameter θ_i at the end of buffer) was inserted manually through the mineral oil layer into the droplet, at a low angle (α) to the horizontal plane, as illustrated in Figure 3.3. Assuming that the fluidic length change in the tip after dispensation is L_d, then the volume V_d dispensed by the microinjection system is estimated using the following equations:

$$V_d = (cos\ \alpha)^{-1}L_d\pi(\theta_i/2)^2 \hspace{3cm} \text{Equation 3.9}$$

(Here, we assume that the sides of the micropipette are parallel, i.e., that the change of inner diameter θ_i after dispensation is close to zero)
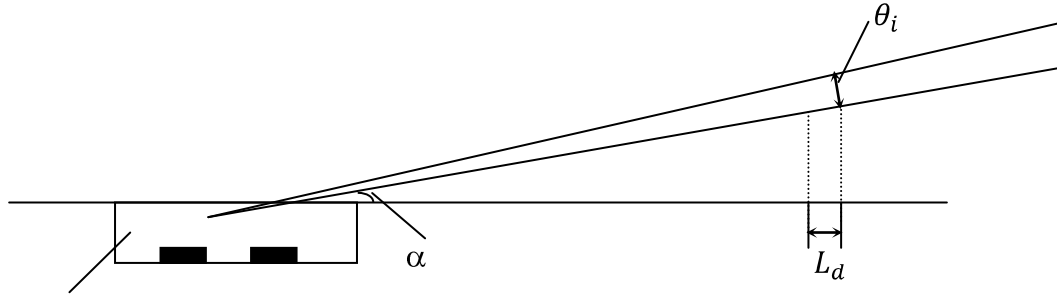
Buffer in microchamber

Figure 3.2: Schematic graph of a pulled pipette for calibration of picolitre scale solutions, where α = angle of positioned pipette to the horizontal plane; θ_i = inner diameter of pipette at the end of buffer; ΔL = fluidic length change in the tip after dispensation.

The shot time (T_d) of the one-shot timer was set to 50ms, 100 ms, 200 ms, 300 ms, or 400ms. L_d was measured using a Nikon microscope (eyepiece $\times 10$, objective $\times 10$), and for one certain shot time, the length change L of the fluid was measured three times. Table 3.1 shows the length change of the fluid after dispensation with different shot times, giving a linear relationship between T_d and L_d:

$$\boldsymbol{L_d(\mu m) = 0.2435 T_d (ms)}$$ Equation 3.10

Table 3.1 The fluidic length change in the tip after dispensation (measurement times $\boldsymbol{n = 3}$) with responses to different shot times ($\boldsymbol{T_d}$).

T_d(ms)	Ld after dispense using Tip 1 (μm)	Ld after dispense using Tip 2 (μm)	Ld after dispense using Tip 3 (μm)
50	12.2	12.1	12.2
100	24.4	24.3	24.3
200	48.7	48.6	48.6
400	97.4	97.3	97.4

Substitution of Equation 3.10 and the values of α (30°), θ_i (8 μm) as measured under the microscope into Equation 3.9 gives a final plot Equation 3.11 between dispensed volume (V_d) and shot time (T_d).

$$\boldsymbol{V_d(pL) = 0.0139 T_d (ms)}$$ Equation 3.11

A calibration table (Table 3.2) can be easily obtained from Equation 3.11 for different shot time dispensations.

Table 3.2 Calibration table for dispensed volume (V_d) with response to the shot time of dispensation (T_d) in the microinjection system.

T_d (ms)	100	200	400	1000	2000
V_d (pL)	1.3	2.6	5.2	13	26

3.3   Results and Discussion

3.3.1   FMCA Measurements and Device Characterisation

Ferrocene monocarboxylic Acid (FMCA) was used as a model redox compound to investigate the electrochemical characterization of the integrated sensors. FMCA has a reversible electrochemical redox couple between ferrocene and ferrocenium. An electron can be removed from the FMCA molecule by the working electrode, causing the molecule to be oxidised. The oxidised form of FMCA in solution may accept an electron from the working electrode and be reduced to the original molecule.

3.3.1.1 Characterisation at Varying Scan Rates

Figure 3.5 (a) shows the cyclic voltammetry responses to FMCA at varied scan rates from the integrated sensors (with an integrated Ag|AgCl microreference). Under the experimental conditions used in this study and over the range of potential scan rates between 10 and 300 mV/s in 1.0 mM FMCA (in 10 mM PBS bulk solution), FMCA gave voltammograms consistent with a reversible one-electron redox agent at the working microelectrode. The peak potential separation ($E_{pa} - E_{pc}$, 57 mV) is independent of scan rate and the anodic peak current (i_{pa}) is equal to the peak cathodic current (i_{pa}). The experimental half-wave potential $E_{1/2}$, for the redox couple was estimated as 0.27 mV, which compared favourably with the literature value of 0.26 mV. All of these factors

indicate that the redox process remains in equilibrium throughout the potential scan. The peak current function increases linearly as a function of the square root of scan rate v, as in legend of Figure 3.5, with a correlation coefficient r^2 of 0.998, as shown in Figure 3.5 (b). Each point was measured in triplicate and the mean was taken, with error bar as shown. At slow scan rates, steady-state current persisted up to a scan rate of 20 mV/s and a plateau current was present. At faster scan rates, the CV responses showed peaked behaviour.

(a)

(b)
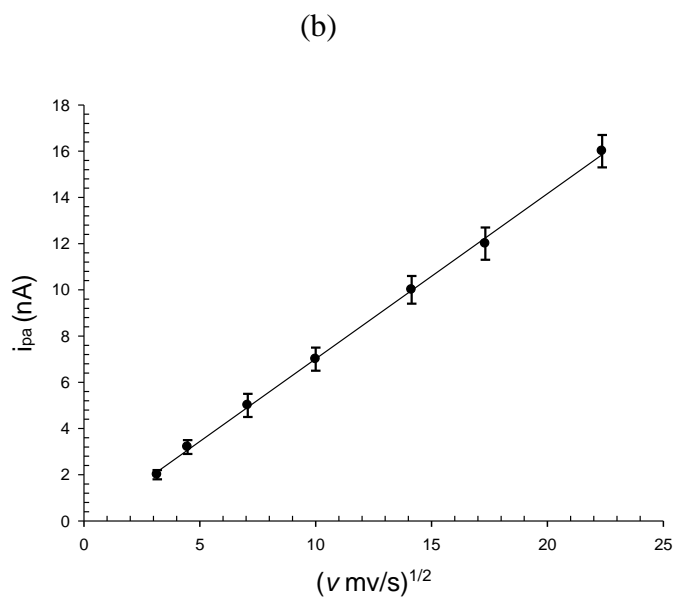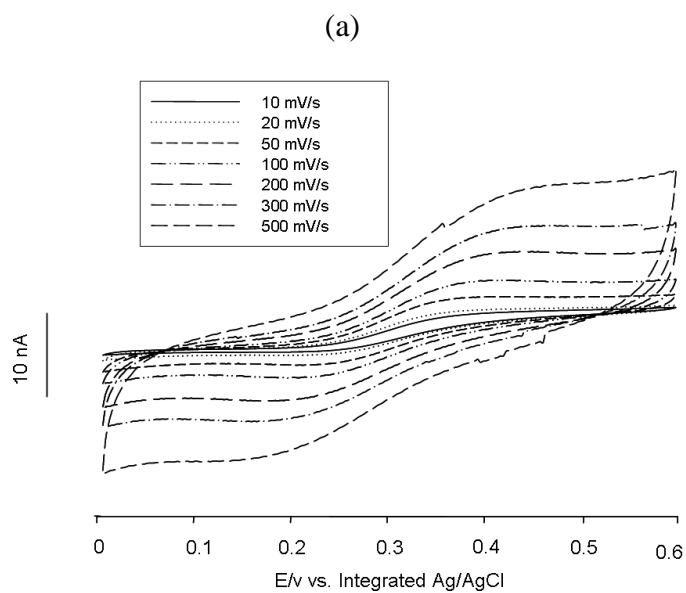
Figure 3.3 Response of a three-electrode device to 1.0 mM FMCA in 10mM PBS bulk solution: (a) the DC cyclic voltammograms at a scan rate between 10 ~ 500 mV/s; (b) the relationship between the peak current ipa and $v^{1/2}$ in (a), where v is the potential scan rate, indicating diffusion-limited reactions, $r^2 = 0.998$. Each point was measured in triplicate and the mean was taken, with error bar as shown. The surface area of the working electrode was 1800 μm^2.

3.3.1.2 Characterisation at Varying Concentrations

Figure 3.6 (a) shows DC cyclic voltammograms of the response to different concentrations of FMCA (2 mM to 0.1 mM) in 10 mM PBS at a scan rate of 50 mV/s. Figure 3.6 (b) demonstrates the plot of peak current i_{pa} against concentration of FMCA in PBS buffer. Each point was measured in triplicate and the mean was taken, with error bar as shown. The linear range of FMCA detected varied from 0.1 to 2.0 mM with a correlation coefficient r^2 of 0.993. Interestingly, it was noted that the correlation coefficient r^2 would decrease at increased concentrations of FMCA when using sputtered gold as a working electrode material (data not shown), due to adhesion of FMCA onto the gold surface.
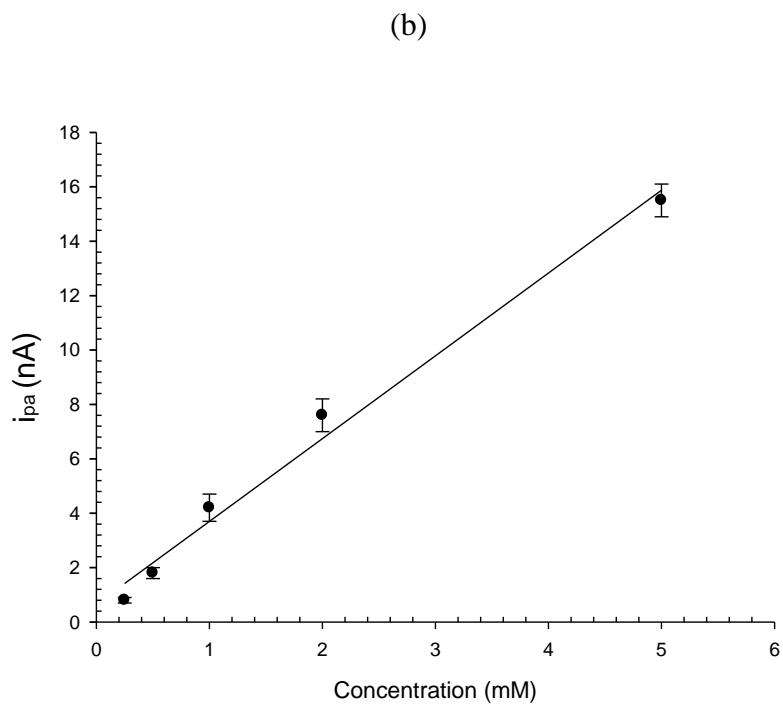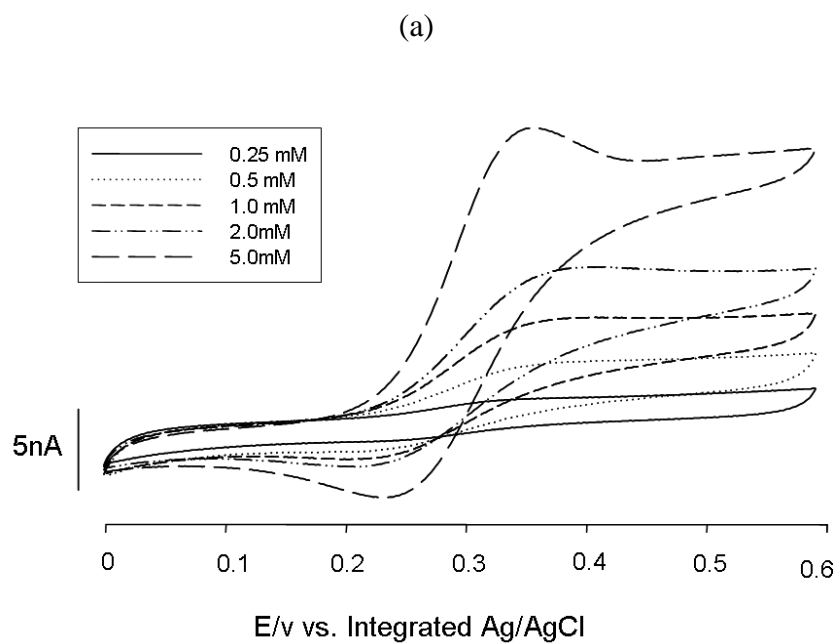
Figure 3.4 Three-electrode sensor response to FMCA in 10mM PBS bulk solution at a scan rate of 50 mV/s: (a) DC cyclic voltammograms response to different concentrations of FMCA; (b) the plot of ipa against concentrations of FMCA, $r^2 = 0.993$. Each point was measured in triplicate and the mean was taken, with error bar as shown. The surface area of the working electrode was 1800 μm^2.

3.3.2   Microreference Evaluation

3.3.2.1 Characterisation of Internal Microreference Electrode using FMCA

As described previously in Chapter 2, a thin layer of AgCl was electrochemically deposited onto Ag, which was electroplated or evaporated onto a Pt electrode. This Ag|AgCl film formed a micro-quasi reference electrode. The actual potential of the microreference electrode *vs.* a true macro-reference electrode, Ag|AgCl (BAS), was calibrated in order to evaluate the performance of the microreference electrode. The calibration was simply achieved by measuring the formal redox potential of FMCA/FMCA$^+$, E$^\circ$ $_{(FMCA/FMCA+)}$ *vs.* a micro-quasi reference. The formal redox potential of FMCA/FMCA$^+$ was known *vs.* a macro Ag|AgCl reference under the same conditions. An approximation to the formal redox potential of FMCA/FMCA$^+$, E$^\circ$ $_{(FMCA/FMCA+)}$ was derived by measuring the mid-point potential of anodic and cathodic peaks (E$_{1/2}$). Figure 3.7 shows that E$_{1/2}$ was estimated to be +295 mV *vs.* the micro-quasi reference Ag|AgCl, and +310 mV *vs.* the true reference Ag|AgCl, indicating that the actual potential of the micro-quasi reference Ag|AgCl *vs.* Ag|AgCl (BAS) was about +15 mV. (Figure 3.8)

(a)

(b)
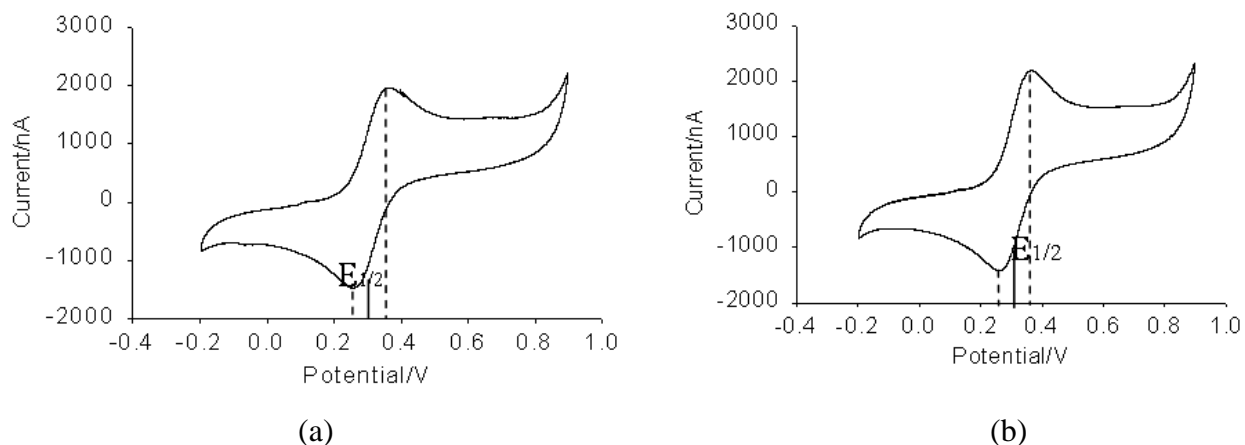
Figure 3.5 Cyclic voltammetric responses in 2.0 mM FMCA in 10mM PBS (pH 7.4); ionic/compositions were equivalent in both experiments: (a) the potential of an external microdisk gold electrode was scanned with reference to a microreference Ag|AgCl. The formal redox potential of FMCA/FMCA$^+$, E° $_{(FMCA/FMCA+)}$ is estimated to be +295 mV *vs.* micro-quasi reference; (b) The potential of the same external microdisk gold electrode was scanned with reference to a true reference electrode Ag|AgCl (BAS): E° $_{(FMCA/FMCA^+)}$ is estimated to be +310 mV *vs.* macro Ag|AgCl (BAS) reference electrode.
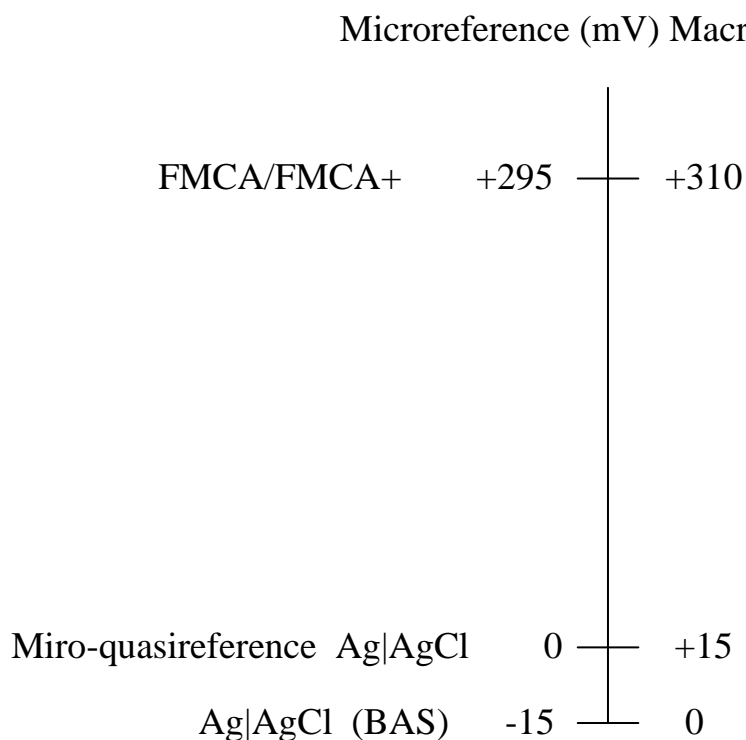
Figure 3.6 Potential of redox couples FMCA/FMCA$^+$ and the reference electrode in 10 mM PBS (pH 7.4). Potentials *vs.* the microreference Ag|AgCl electrode are plotted on the left; potentials *vs.* the macroreference Ag|AgCl electrode are plotted on the right.

3.3.2.2 Potential Stability of Internal Microreference

As a consequence of the thin layer of AgCl, the most influential factor with regard to the durability and potential stability of the internal microreference electrode is dissolution (K_{sp} in aqueous media is $\sim 1.8 \times 10^{-10}$ M^2 of the AgCl layer). DC voltammograms of the potential of an external microdisc gold electrode *vs.* a microreference Ag|AgCl (20×20 μm^2) electrode were examined for 2.0 mM FMCA in 10 mM PBS, in the same conditions as in Figure 3.7 (a). The experimental half-wave potential $E_{1/2}$ obtained during the course of 15 hours (Figure 3.9) shows that a stable and reproducible potential of Ag|AgCl microreference was obtained over this period. After each test, the microreference electrode was dried and stored in foil paper in the dark. This microreference electrode can hence be applied to this research and used as a miniaturised reference electrode for general use, although the stability and cleanliness of the reference electrode would be compromised during its application for mammalian cells analysis, as will be discussed in Chapter 4.
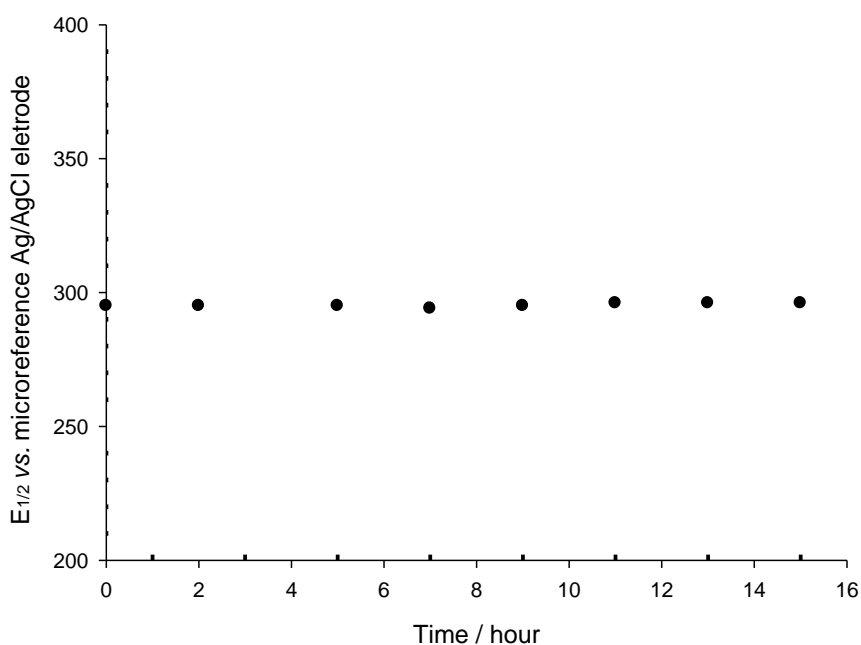
Figure 3.7 Eexperimental half-wave potentials $E_{1/2}$ *vs.* a microreference Ag|AgCl electrode tested over 15 hours.

3.3.3   Lactate Measurements and Sensor Calibration

3.3.3.1 Response to Macro-volume Lactate

Biosensors for the measurement of lactate can be produced by modifying the microsensor with the enzyme lactate oxidase (LOD). Lactate may then be determined amperometrically using the enzyme-linked assay described in Equations 3.1 and 3.2.

The microwell device was filled with 5 µL 120 units/mL LOD in 10 mM PBS (pH 7.4). After the background residual current settled to a constant value, microlitre scale lactate was injected into the microwell using a micropipette. Figure 3.10 (a) shows the i-t plot in response to successive additions of 2 µL lactate of increased concentrations (5~160 µM) at different time points (marked by arrows). Each addition was made after the steady-state current was achieved. The steady-state current output as a function of lactate concentration is illustrated in Figure 3.10 (b), and shows a linear relationship between 9 µM and 110 µM of lactate with a correlation coefficient of r^2 0.986 and response sensitivity of 0.012 nA/µM. Each point was measured in triplicate and the mean was taken, with error bar as shown. The detection limit (defined as the concentration corresponding to a signal three times the noise level of the background) that can be achieved using this protocol, is 18 µM lactate.
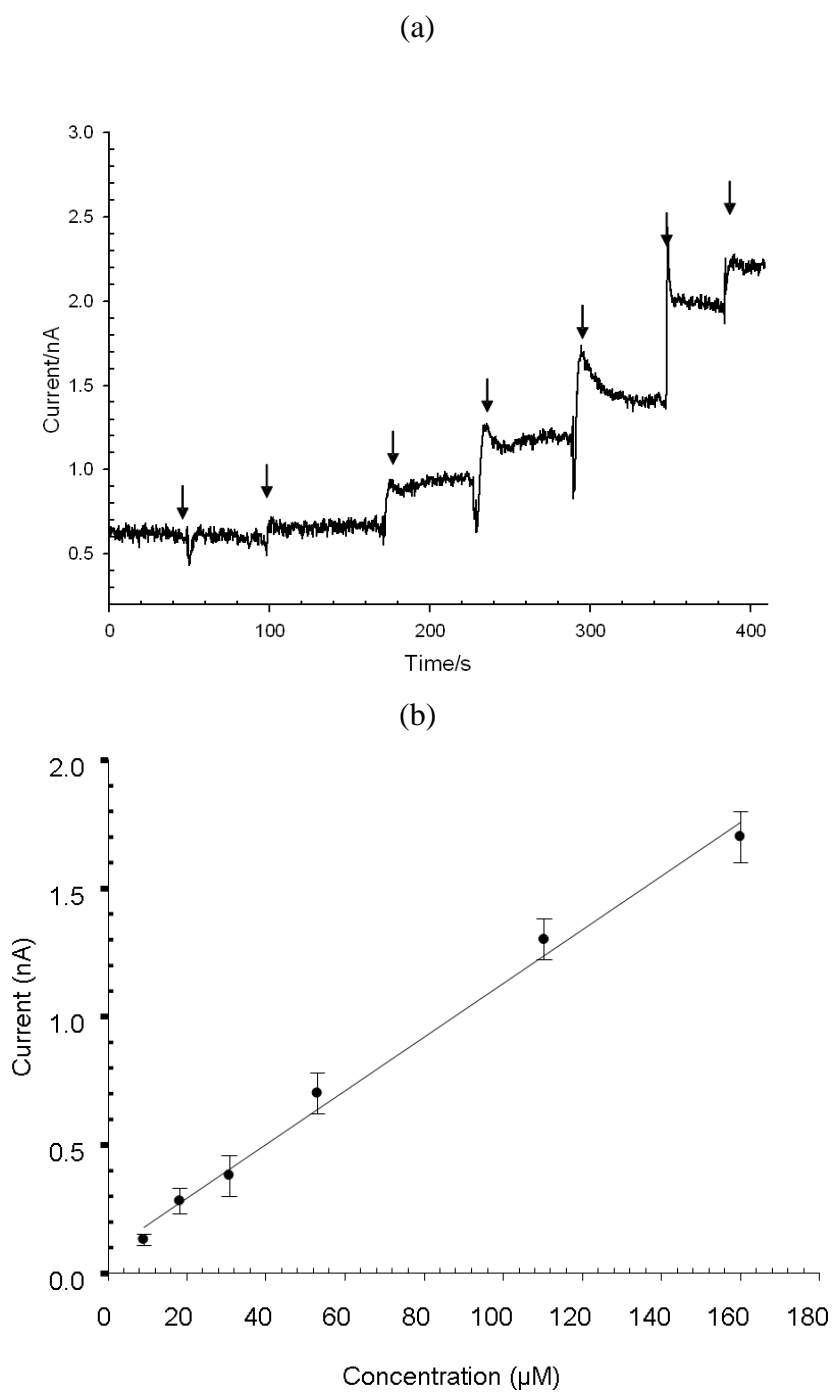
Figure 3.8 (a) Typical current-time behaviour in response to successive additions of lactate of increased concentrations. The working potential was held at +0.64 V *vs.* the internal Ag|AgCl reference electrode. The microwell device was filled with 5 μL of 120 units/mL LOD in 10 mM PBS (pH 7.4). 2 μl aliquots of lactate (5.7 μM, 9 μM, 18 μM, 31 μM, 53 μM, 110 μM, 160 μM) were successively injected into the well (the time points when lactate was injected are marked with arrows); (b) plot showing the linear regression analysis of steady-state current output of the lactate sensor as a function of lactate concentration. Each point was measured in triplicate and the mean was taken, with error bar as shown. The surface area of the working electrode was 1800 μm^2.

The steady state currents in response to the addition of lactate could be disturbed, as noted in Figure 3.10 (a). This disturbance might have been caused by manual variations of each injection and the consequent perturbation of the electrode double layer, which would contribute to the non-Faradic current. To minimise the errors during injection, a more consistent microinjection system has been developed, as described (see Chapter 3.2), and will be used for precise control of pL-scale lactate calibration.

3.3.3.2 Lactate Response at Varying Potentials

The response of the sensor to lactate at different applied potentials was investigated. The Pt working electrode was held at the indicated potentials versus the integrated Ag|AgCl electrode. Figure 3.10 shows the amperometric response of the integrated enzyme-modified sensors to microlitre lactate injection at different applied potentials. The microchamber was filled with 5 µL of 120 units/mL LOD in 10 mM PBS (pH 7.4), and then 0.1 µl of 1.2 mM Lactate was injected. Figure 3.11 (a) shows the plot of amperometric current against time at different potentials. Figure 3.11 (b) shows the real Tafel plot of current peak against applied potential, obtained from the data from Figure 3.11 (a). With a correlation coefficient r^2 of 0.983, the regression can be expressed as $\log I = -1.25 + 3.12E$. Comparing with the Butler-Volmer Equation, we can obtain $3.12 = (1 - \alpha)F/2.303RT$, in which $F/RT = 38.9$ at 25 °C. Therefore, the transfer coefficient α is then calculated as 0.73.

$$\log I = -1.25 + 3.12E$$
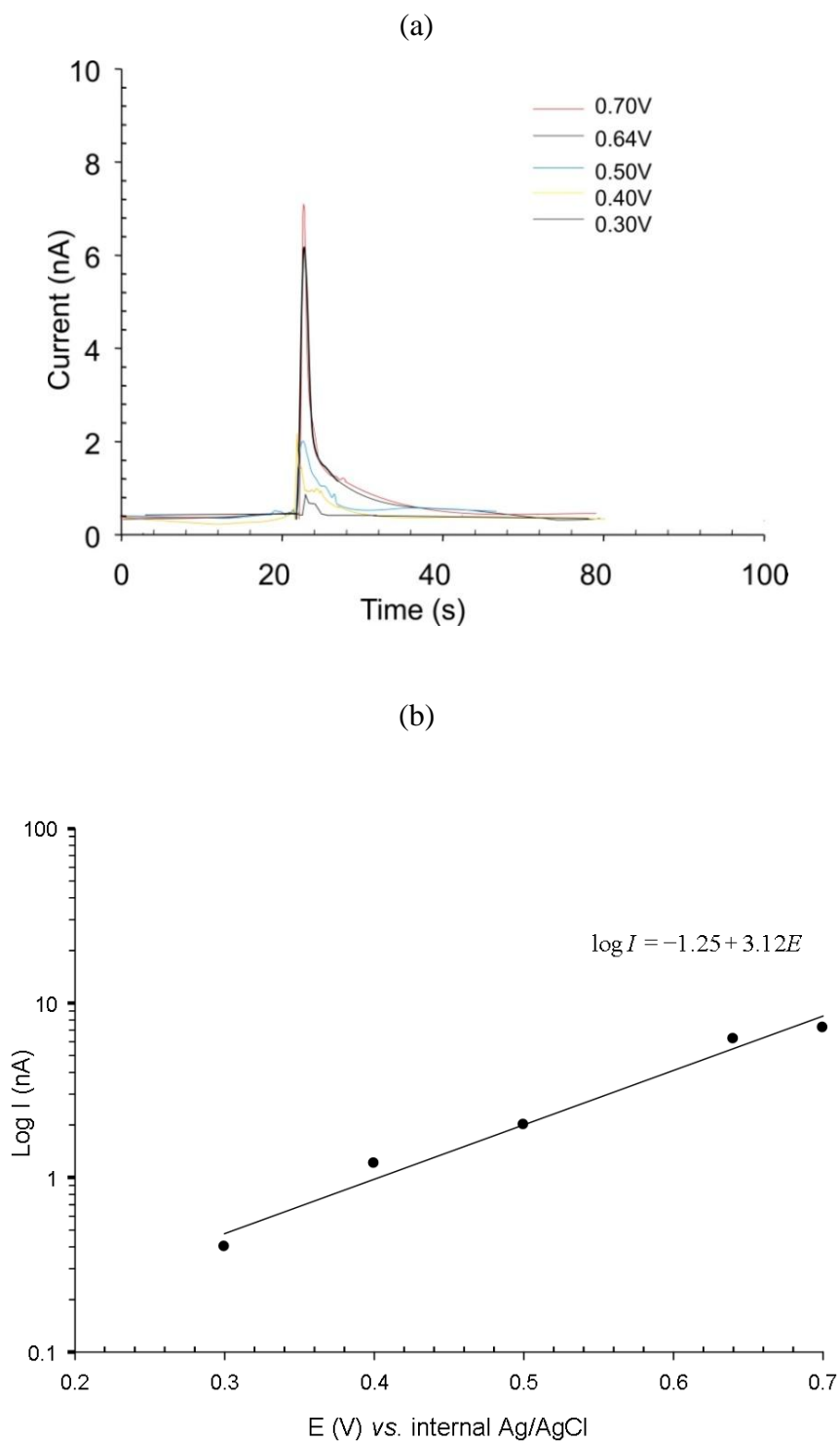
Figure 3.9 "Macro-volumetric" characterisation of three-electrode sensor response to lactate at different applied potentials. The Pt working electrode was held at the potentials indicated *vs.* the internal Ag|AgCl reference. The microwell of the device was filled with 5 μL of 120 units/mL LOD in 10 mM PBS (pH 7.4), and then 1 μl of 1.2 mM lactate was injected: (a) Plot of current against time; (b) Tafel plot of current peak against applied potential, obtained from the data from (a). The surface area of the working electrode was 1800 μm^2.

3.3.3.3 pL-scale Lactate Measurements

Results of the pL-scale lactate measurements using the microinjection system are given in Figure 3.12. The microchamber was filled with 120 units/ml LOD, using a pulled capillary of sub-micro-bore size, as described previously (see Chapter 2). Then, 1 mM lactate was injected in 5.6 pL, 11.2 pL, 22.4 pL, 44.8 pL, 89.6 pL amounts. Each of the injections was controlled by the corresponding dispensation shot time using the pL-scale dispensation system. The signal from each addition was allowed to return to the baseline before the next addition, indicating that all the injected lactate was completely oxidised with LOD. The response of current transients to the addition is faster than in macro-detection of lactate (ca. 2 sec to arrive at the peak current). The increased speed of response to the injected lactate is a consequence of the reduced diffusion length to the sensor, due to the much shorter distance between the injection point and the microchamber achieved by the pL-scale dispensation system.

(a)   (b)
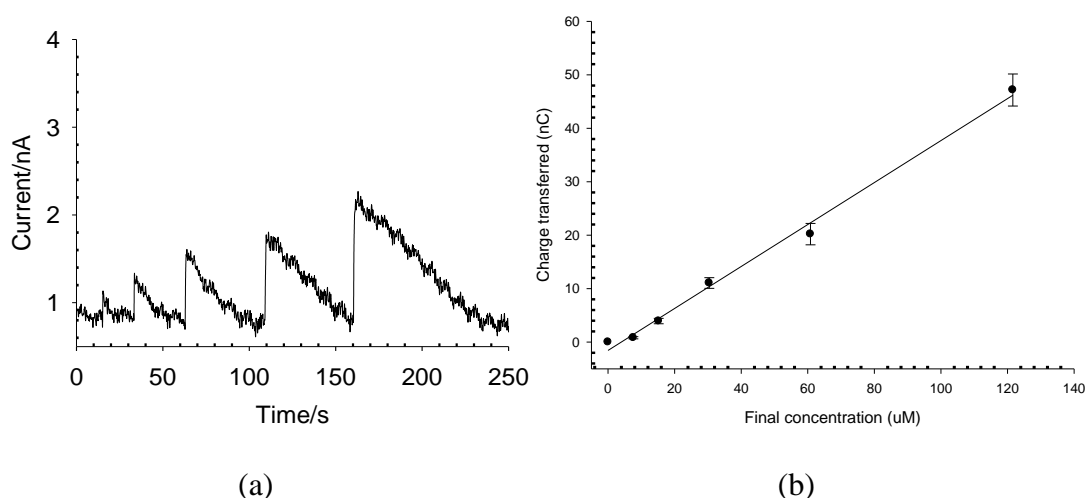
Figure 3.10 (a) The current-time plot in response to injection of pL-scale lactate. The device was filled with 650 pL 10 mM PBS containing 120 units/ml LOD. 5.6 pL, 11.2 pL, 22.4 pL, 44.8 pL, 89.6 pL volume of stock solutions of 1 mM lactate were injected. The oxidised current was recorded. (b) Lactate calibration plot of the charge transferred to the working electrode and the final concentration of injected lactate.

As illustrated in Figure 3.12 (a), each injection resulted in a measurable electrochemical oxidation current and between injections the electrochemical signal returned to the baseline. Figure 3.12 (b) gives a measurement of the charge, Q, corresponding to lactate oxidation. A linear relationship between the charge transferred to the working electrode

and the injected lactate final concentration (7.6 µM, 15.2 µM, 30.4 µM, 60.8 µM, 121.6 µM) was obtained, $r^2 = 0.996$.

3.3.4   Enzyme Immobilised Microfabricated Sensor

3.3.4.1 Enzyme immobilised sensor

Immobilization of bio enzyme onto a solid surface is an important part of amperometric or potentiometric sensor design. The methods of enzyme immobilisation include physical adsorption, covalent binding, entrapment in a porous matrix and confinement behind a dialysis membrane. The immobilisation leads to a change of enzyme structure, which consequently may cause a difference in the kinetics, stability and specificity from that of enzymes in a homogeneous solution. Electrochemical polymerisation has been used to immobilise enzymes at the electrode surface by depositing a porous membrane to entrap the enzyme on the electrode surface. The flexibility and simplicity of implementation of this approach provide significant advantages over other methods [130]. Specifically, the electrochemical immobilisation is suited to the spatially localised deposition of the enzyme onto the miniaturised structure, such as microelectrodes and microelectrode arrays, as the polymer can be electrochemically locally deposited on the electrode surface. In this way the immobilisation of enzymes onto the microelectrode can be used to produce biosensors for *in vivo* application and for small sample volumes. Both conducting and non-conducting polymers can be used with this method, among which conducting polymer can produce a thickness controlled by the electrochemical deposition parameters, while the growth of non-conducting polymer is self-limited.

The use of electropolymerised phenol film has received attention because the pre-adsorption of the enzyme onto the electrode surface provides some degree of molecular self-assembly and because the growth of the polymer is self-limited [130]. In addition, the insulating phenolic film may reduce interference and fouling of the electrode to some degree [131]. There is improvement in the collected signals from the use of enzyme-immobilised microelectrodes over free enzyme electrodes, which may include much quicker response times and improved signal-noise ratio [131].

3.3.4.2 Enzyme Modification

The first five cyclic voltammograms obtained during the oxidation of o-phenylenediamine in 50 mM PBS buffer (pH = 7.4) containing supporting electrolytes are shown in Figure 3.13 (a). The last five cyclic voltammograms are shown in Figure 3.13 (b). These cyclic voltammograms during polymerization of o-phenylenediamine indicate that after the third scan, the oxidation current has almost decreased to background, indicating little further deposition of polymer film (i.e. the process is self-limiting, as the polymer film is insulating). From cyclic voltammograms during the oxidation of o-phenylenediamine, the amount of charge passed was estimated using the sum of the integrals of scans 1 to 5 by subtraction of the integration of the background current of from scan 6 to 10. Considering this, together with the molecular volume $104.85 cm^3$/mol of the polymer, a film thickness of ca. 110 nm of poly(o-phenylenediamine) was estimated.

(a)

(b)
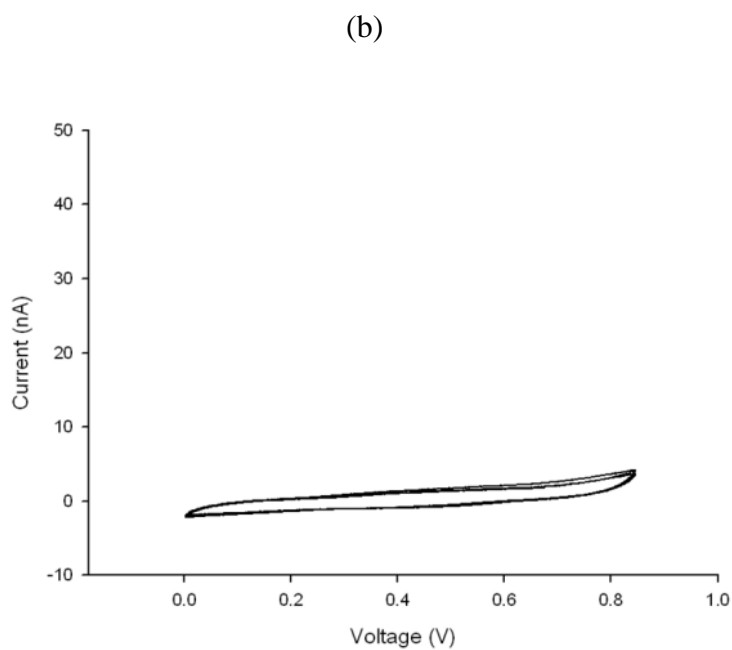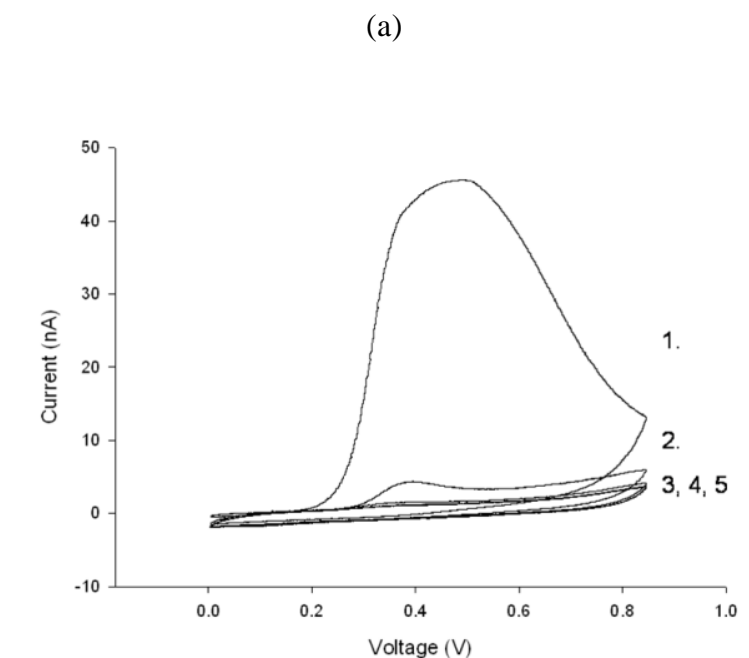
Figure 3.11 (a) Typical cyclic voltammograms showing the deposition of the polymer film (scan rate at 50mVs^{-1}) obtained using the microfabricated enzyme-modified sensor in PBS buffer (pH = 7.4) containing 30 mM *o*-phenylenediamine. The sensor surface area was 1800 μm^2. Cycle numbers (1-5); (b) The last five cyclic voltammograms obtained during the oxidation of *o*-phenylenediamine in 50 mM PBS buffer (pH = 7.4). Cycle numbers (1-6).

3.3.4.3 Measurements and Calibration of LOD-immobilised Sensor

The measurement of lactate using enzyme-modified biosensors can be amperometrically determined through the enzyme linked assay, described in Equations 3.1 and 3.2. After the adsorption of enzyme and its subsequent entrapment in the polymer film, the sensors were characterised by the addition of standard aliquots of pL-amounts of L-lactate using the nanopipette system. The microchamber was filled with 650 pL of PBS buffer (pH = 7.4) and, using pre-determined injection time intervals, 1.2 mM L-lactate stock solution was injected to give final lactate concentrations of 7.4 μM, 18.5 μM , 36.9 μM, 55.4 μM, 101.5 μM, 221.5 μM and 443.1 μM. Each injection immediately resulted in a measurable electrochemical oxidation current with the electrochemical signal returning to the background within 5-10 s, as shown in Figure 3.14 (a).

The measured charge (Q) corresponding to total H_2O_2 oxidation showed a linear relationship with the quantity of injected lactate (x) up to a maximum of 101.5 μM (specifically, Q (nC) = 0.1835x (fmol), r^2=0.986). The precision of measurement was investigated using four repetitive measurements with standard deviations of <5.2 %.

<div align="center">(a)   (b)</div>
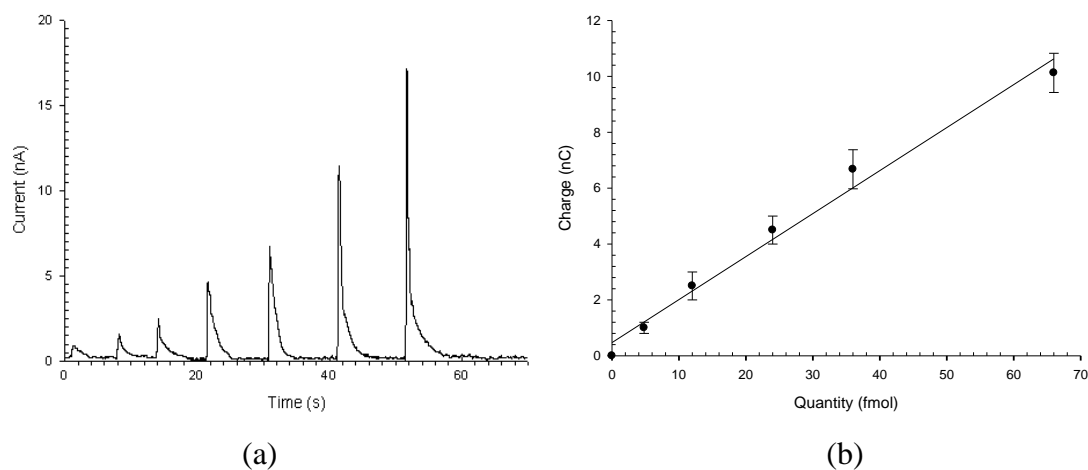
Figure 3.12 (a) Representative current-time response to successive additions of pL lactate, as described in the text. (b) The relationship between Q and the amount of lactate added was linear between 4.8 and 66.0 fmol with a correlation coefficient r^2 of 0.986. The sensor surface area was 1800 μm^2.

To account for the non-Faradic current caused by the injection pulse perturbing the electrode double layer, a number of control experiments were performed involving the addition of identical volumes of buffer and the injection of lactate in the absence of enzyme (before the sensor was modified by enzyme). There was a very small background

signal, and the integral of total Q was always <2% of the equivalent titre of lactate, measured under identical experimental conditions (data not shown).

A low detection limit of 4.8 fmol was obtained (equivalent to the detection of ca. 7.4 μM, considering the chamber volume of 650 pL), which compared favourably with other immobilised macro and microelectrode biosensor systems [132, 133]. The increased sensitivity in this integrated biosensor might result from efficient transport of lactate to the pL-scale microchamber, with little loss to the bulk solution. The fast response of the sensors (5-10 s) is also noted, especially when compared to the response times found when using free-enzyme sensors (50-100 s). The high temporal resolution and sensitivity are crucial for real-time monitoring of metabolites, particularly from single cells, in which trace amounts of intracellular sample (zeptomoles to femtomoles) and millisecond scales of reaction time take place.

3.3.4.4 Kinetics of LOD-immobilised Sensor

The Michaelis-Menten equation gives the enzyme kinetics as follows:

$$V = \frac{V_{max}\,[S]}{K_M + [S]}$$
Equation 3.12

V is the reaction rate, V_{max} is the maximum reaction rate, $[S]$ is the substrate concentration and K_M is the Michaelis-Menten constant. K_M represents the substrate concentration at which the reaction occurs at half of the maximum rate. K_m is an important indicator of the affinity that an enzyme has for a given substrate, and hence of the stability of the enzyme-substrate complex. At low $[S]$, the availability of substrate is the limiting factor: as more substrate is added, there is a rapid increase in the rate of the reaction. When $[S]$ reaches higher levels, at which all the enzyme is substrate-bound, adding more substrate will not increase the rate of the reaction.

The microchamber was filled with 650 pL of PBS buffer (pH = 7.4) and, using pre-determined injection time intervals, 1.2 mM L-lactate stock solution was injected to give a lactate quantity of 4.8 fmol, 12.0 fmol, 24.0 fmol, 36.0 fmol, 66.0 fmol, 120.0

fmol, 200.0 fmol, 288.0 fmol, 384.0 fmol. In this case, the Michaelis-Menten response was observed, as shown in Figure 3.15 (a). In the experiments described in this study, it is clear that no steady state current can be achieved, due to the restricted volumes of both lactate and the analytical chamber, where the lactate is completely consumed by the enzyme. Therefore, rather than using the steady state current, we derived kinetic expressions for the charge arising from the reaction in terms of the enzyme kinetics and substrate quantity rather than concentrations:

$$\boldsymbol{Q = \frac{Q_{max}\,[q]}{K_M + [q]}}$$

<div align="right">Equation 3.13</div>

where Q is the charge passed during the lactate enzyme reaction, Q_{max} is the maximum charge passed under saturating conditions, K_M is the apparent Michaelis-Menten constant and $[q]$ is the quantity of added lactate. As shown in Figure 3.15 (b), the slope and intercept of the relation curve between $1/Q$ and $1/[q]$ can give a value of K_M of 29.5 fmol, indicating that 50% of active enzyme sites were lactate bound when 29.5 fmol lactate was added. The total transferred charge no longer increased linearly with respect to the quantity of lactate when a large amount (>66.0 fmol) of lactate was injected. Integration of the current at the working microelectrode during electrochemical oxidation indicated that the charge transferred at the injection of 120 fmol, 200 fmol, 288 fmol lactate accounted for 72.8%, 55.8%, 45.2 %, respectively, of the theoretical total charge, working on the assumption that all the lactate within the chamber is completely consumed by an electrochemical reaction. This result shows that when a large amount of lactate was added not all lactate can be assumed to have been consumed in a given a period of time. It indicates that the lactate reaction in this case might be limited by the saturated enzyme-substrate kinetics (as discussed above). It is also likely that this reaction may be partly limited by the amount of oxygen in the buffer, considering that the moles of oxygen within the microchamber are 812 fmol, which is not far greater than the lactate amount, although there is oxygen diffusion from the air to the buffer through oil layer.

(b)
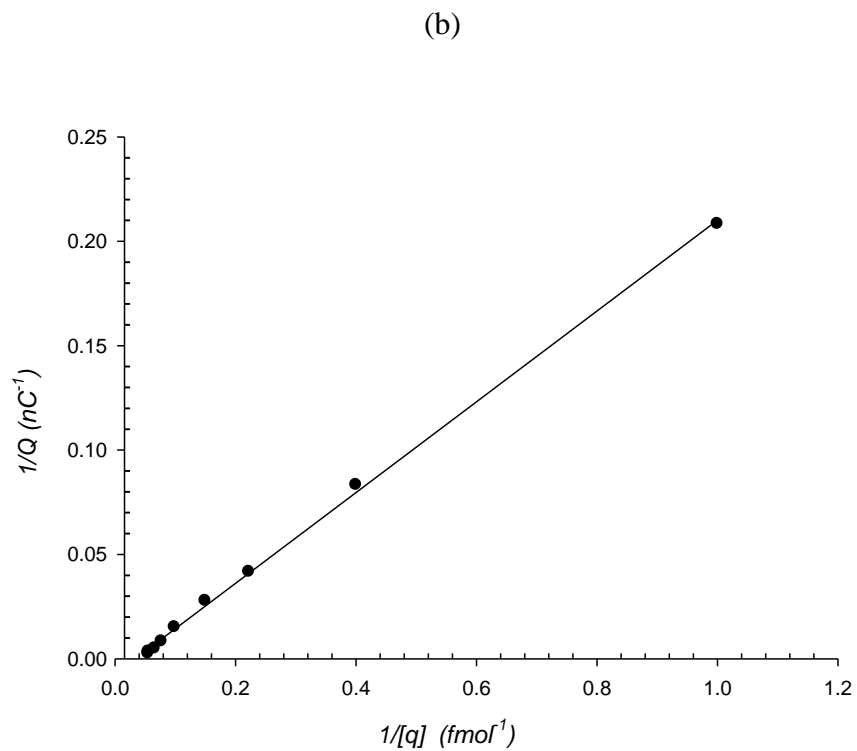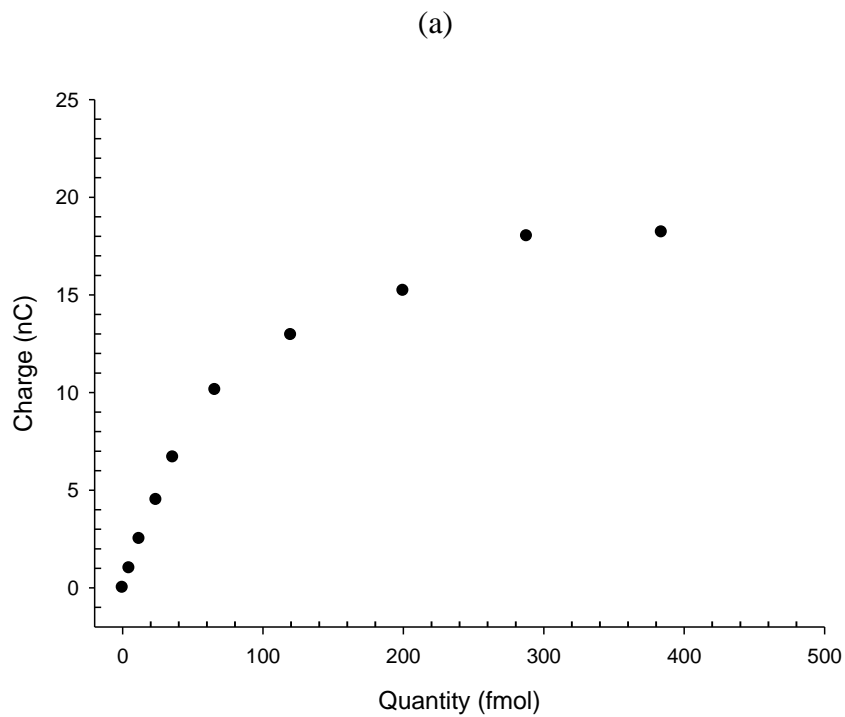
Figure 3.13 Response of LOD immobilised integrated sensor to increased amount of dispensed pL-lactate in the microchamber. (a) Michaelis-Menten response to successive additions of pL lactate, as described in the text.; (b) The relationship between $1/Q$ with respect to $1/[q]$ ([q]: the amount of lactate added) with a correlation coefficient r^2 of 0.998. The sensor surface area was 1800 μm^2.

3.3.4.5 Stability of Enzyme-modified Sensor

The enzyme-modified sensors were stored in a PBS buffer at 4 °C. Stability of the sensor was studied, with a shelf life time of at least 4 days being obtained with no significant decrease in response to pL-scale lactate. As shown in Figure 3.16, the response will decline to 60 % after 8 days. The decrease in response is in part due to changes in the partition of lactate into the film and the loss of enzyme activity. Therefore, fresh enzyme was always immobilised onto the new or cleaned (cyclic cleaning in H_2SO_4 followed by oxygen dry etching) device no more than three days before performing lactate assay experiments.
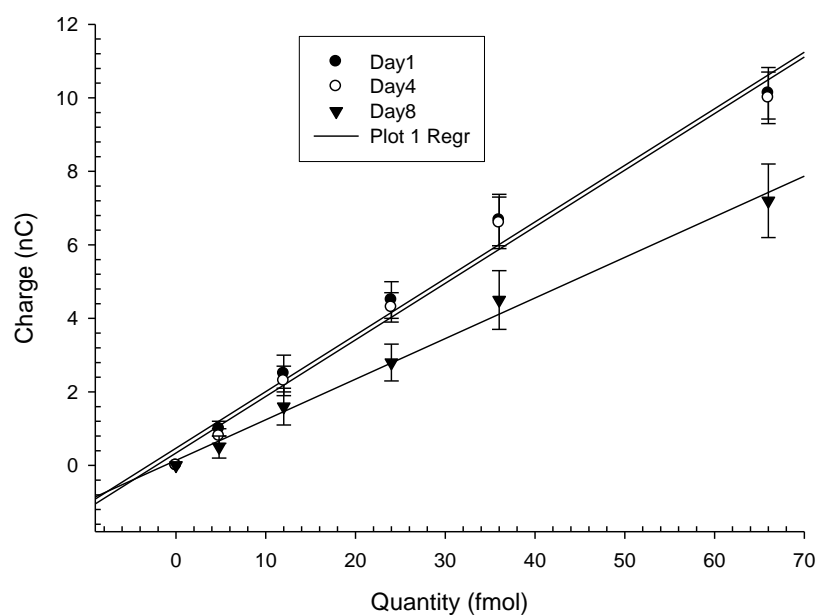
Figure 3.14 Stability of enzyme-modified integrated sensor. The device was stored at 4°C in the background buffer (pH=7.4). Responses were measured to successive additions of pL lactate, giving quantities of 4.8 fmol, 12.0 fmol, 24.0 fmol, 36.0 fmol, 66.0 fmol.

3.4 Conclusion

The microelectrodes were electrochemically characterised using FMCA to give the cyclic voltammetry responses to FMCA at varied scan rates from the integrated sensors, and the response to different concentrations of FMCA in 10 mM PBS. The internal Ag|AgCl was evaluated by using FMCA as a calibrating redox couple, and the actual potential of the

internal micro-pseudo-reference Ag|AgCl *vs.* a true Ag|AgCl reference electrode was determined to be +15mV, showing a stable potential within 15 hours. Microvolume and pL-scale lactate measurements using the micromachined integrated sensor were carried out, with real detection limits of 18 µM and 7.6 µM lactate respectively. The response of the sensor to microvolume lactate at different applied potentials was investigated, giving a plot of current peak against potential. An immobilised microfabricated enzyme-modified sensor was achieved using an electrochemically polymerised film to entrap lactate-oxidized enzyme onto the working electrode. The enzyme-immobilised lactate sensor was electrochemically characterised using a microinjection system to dispense volumes as low as 1 pL, producing a linear calibration curve for the charge transferred *vs.* the amount of the injected lactate, in the range from 4.8 up to 66 fmol, with a detection limit equivalent to 7.4 µM. The fundamental kinetics of the sensor were also investigated. These LOD enzyme immobilised lactate sensors were found to be stable for ~four days. The rapid response and high sensitivity of the LOD enzyme-immobilised lactate sensor provide a generic method based on oxidase-reductase enzymes to make a wide range of sensors for future use as single cell measurements in pL-scale volumes.

Chapter 4 Real-time Monitoring of Metabolites from a Single Beating Heart Cell

4.1 Introduction

4.1.1   Cellular energy and lactate metabolism

In muscles, energy from the breakdown of adenosine triphosphate (ATP) to adenosine diphosphate (ADP) and inorganic phosphate (Pi) by myosin ATPase activates specific sites on the contractile elements, causing the muscle cell to contract. The hydrolysis of ATP yields approximately 31 kJ of free energy per mole of ATP degraded to ADP and inorganic phosphate (P_i) [134]:

$$ATP + H_2O \longrightarrow ADP + H^+ + P_i \text{ (31 kJ per mole of ATP)}$$

Equation 4.1
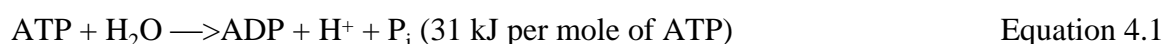
There are three different mechanisms involved in the resynthesis of ATP for muscle force generation: aerobic glucose breakdown, phosphocreatine (PCr) breakdown and glycolysis.

The first of these is aerobic metabolism involving the conversion of glucose, free fatty acid and amino acid into the end products: carbon dioxide (CO_2), water (H_2O) and ATP. For example, up to 38 molecules of ADP can be phosphorylated to ATP when one molecule of glucose is broken down completely to carbon dioxide and water.

The PCr breakdown pathway refers to energy that is provided by the breakdown of phosphocreatine (PCr) to resynthesize adenosine triphosphate (ATP):

$$ADP + PCr + H+ \longleftrightarrow ATP + Cr \text{ (43 kJ per mole of PCr)}$$

Equation 4.2
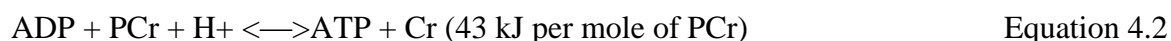
However, the ATP released in this way is exhausted quickly, after only 6-10 seconds of intense muscular contraction, but the energy made available by anaerobic glycolysis allows the performance of high intensity exercise that would otherwise not be possible.

During glycolysis, glucose is broken down into pyruvic acid and some of the energy released is used to form small amounts of ATP, which provides the energy required by the

muscles to contract. In some situations, such as during high intensity exercise when aerobic glycolysis cannot produce ATP quickly enough to supply the demands of the muscle, As a result, anaerobic glycolysis becomes the dominant energy producing pathway as it can form ATP at high rates, which involves that the pyruvate is removed by conversion to lactate, a reaction that does not involve oxygen [134]. During this anaerobic metabolism or diffusion-limited oxygen supply, two molecules of lactate are formed for each molecule of glucose. Therefore, lactate can be a significant bio-maker to indicate the cellular metabolism of cardiomyocytes, and thus chosen as one of the metabolic analytes in this study.

4.1.2   The anoxia model

As a model for anoxia where there is a total decrease in the level of oxygen, heart cells were positioned in contact with carbonylcyanide p-(trifluoromethoxy)-phenylhydrazone (FCCP), cyanide or azide. These substances inhibit aerobic glycolysis. In this model, the anaerobic system will be used to generate ATP with the net production of lactate. As glycolysis proceeds, it will result in the production of lactate.

A second anoxia model, which does not involve the addition of inhibitors, occurs when cells are actively contracting intensely, and the energy produced from aerobic glycolysis does not allow the performance of high intensity exercise. As discussed above, anaerobic glycolysis is used to generate ATP with the net production of lactate. Lactate production will hence be in proportion to the metabolic rate of the cell.

4.2 Chemicals and Materials

All solutions were prepared using high-purity deionized water (Millipore Elix 10) and analytical reagent grade chemicals, without further purification. Unless otherwise stated, all chemicals were obtained from Sigma-Aldrich (Dorset, UK). Lactate solutions, for sensor calibration, were prepared as stock solutions in appropriate buffers immediately prior to their use. The supporting electrolytes were 10 mM phosphate buffered saline, PBS (10 mM phosphate buffer containing 2.7 mM KCl and 137 mM NaCl, pH 7.4). Single adult rabbit ventricular myocytes were isolated from the left ventricle by perfusion of the heart with collagenase solution. Cells were maintained in Krebs Base Solution (KBS) containing 120 mM NaCl, 20 mM sodium *n*-hydroxyethylpiperazine-n'-2-ethane

sulphonic acid, 5.4 mM KCl, 0.52 mM NaH$_2$PO$_4$, 3.5 mM MgCl$_2$, 6H$_2$O, 20 mM taurine, 10 mM creatine, 11.1 mM glucose, 0.1% BSA, and 1.8 mM CaCl$_2$, pH adjusted to 7.4 with 100 mM NaOH. Extra-cellular medium was also used, which contains appropriate ionic concentrations to allow excitation-contraction of cells.

4.3 Methods

4.3.1 Fabrication

Masks for all microelectrodes were designed in L-Edit^{TM} and produced as chrome-coated maskplates using a Leica EPBG5-HR electron beam writer (Leica, Germany) (refer to Section 2.2). All microfabrication was adapted from standard photolithographic methods, including metal evaporation, electrochemical metal deposition and lift-off, as detailed in section 2.3.

4.3.2 General Experimental Protocol

All experimental work was performed on a microscope stage, which was housed in a Faraday cage, as a platform onto which the microfabricated device was fixed. The five bonding pads on the microelectrodes (both electrochemical electrodes and stimulation electrodes) were wire-bonded to a PCB board and subsequently connected to the potentiostat and the stimulator. Throughout the course of an experiment, the temperature was maintained at 25°C. Dry etching was used to regenerate passivated electrodes after cellular assay experiments using an ET Plasmofab 505 Barrel Asher (Electrontech) for 30-60 s with 2 L min^{-1} oxygen, 6 psi nitrogen, 50 mT base pressure, and 100Wrf power. The extent of electrode regeneration, after cellular assays, was characterised through experiments involving the redox compound ferrocenemonocarboxylic acid.

4.3.3 Single Heart Cell Experimental Protocol

4.3.3.1 Single-Cell Selection

200 μl cell suspension was dropped into a PDMS microreservoir containing two platinum macroelectrodes connected to a signal generator (isolated stimulator, Digitimer, Welwyn

Garden City, UK). A 0.5 Hz square wave signal was used to field-stimulate the cells. The amplitude of the input signal was gradually increased from zero until excitation-contraction of ca. 80% of the cells was observed. The myocyte has a clear striation within its sarcomere and IonWizard software was used to determine the extent of cell shortening. A single cell was selected if it contracted in response to a low amplitude stimulus (ca. 5 V cm^{-1}) with regular and uniform shortening.

4.3.3.2 Single-Cell Handling

The microsystem for single-cell manipulation involved a micropipette (with a pulled capillary tip with a diameter of ~60 μm) coupled with a microfluidic connection with a 500 μl gas-tight microsyringe, which was controlled using a micro-precision screw in a custom-built holder. The system was fixed on three-axis micromanipulators (x-y-z movement) and filled with KRB buffer before cell handling.

The micropipette was positioned above and close to the selected cell, and, by gentle expulsion and suction of the capillary, the cell was introduced into the capillary tip. This micropipette was then brought over the microchamber and a tiny droplet containing the cell was deposited into the microchamber, such that it was aligned longitudinally to the axis of the chamber. The cell was observed to sediment to the bottom of chamber. As previously described, the volume of the medium was then reduced to a fixed volume represented by the geometric dimension of the analytical microchamber using a second micropipette.

4.3.3.3 Single-Cell Metabolic Monitoring

Individual cells were stimulated within the microsystem by applying a biphasic rectangular pulse of alternating polarity, using a custom-built electric field stimulator coupled with a frequency generator. The amplitude, duration and frequency of each rectangular pulse applied to the cell through the pair of stimulatory microelectrodes which was connected to the stimulator through a PCB board. The pH sensitive dye BCECF (10 μM, Molecular Probes, Eugene, OR) was added to the microchamber to monitor the extracellular pH change during field stimulation using the same filter set as for Fluo-3, as described below. The change in pH could arise either through the cell's metabolic process or from electrolysis events owing to the stimulating microelectrodes (hydrolysis would be

expected to occur at potentials 0.8 V *vs.* Ag|AgCl, and in all field stimulation experiments, absolute applied potentials were maintained below this value).

Cells were loaded with Fluo-3 by incubation for ~ 30 minutes in 20 μM Fluo-3 AM solution (Molecular Probes, Eugene, OR) for the recording of intracellular Ca^{2+} transients. Intracellular Ca^{2+} was monitored using the fluorescence-contractility system of IonOptix (Milton, MA). The Fluo-3 indicator was excited at 490 nm with a TILL monochromator (T.I.L.L. Photonics, Martinsried, Germany), which was mounted on a Zeiss Axiovert 200 (Zeiss, Germany) equipped with the x63 C-Apochromat water immersion lens, NA 1.2.

The contraction of the cell was recorded by passing the light of the halogen lamp through a 680 nm bandpass filter and imaging the striation of the sarcomere onto a 240 Hz frame shift charge-coupled device (CCD), (IonOptix, Milton, MA). Sarcomere length changes were recorded with the IonWizard Version 5.0 software, and then converted to give a measure of relative cell length. Alternatively, the cell shortening was measured using off-line edge detection on recordings of cell contraction. The sarcomere length of the cardiomyocyte is ca. 2.0 μm diastolic to 1.6 μm systolic, so 100% contraction with respect to the sarcomere length at rest is ca. 0.4 μm. In all the experiments, a ceiling of mineral oil was immediately placed over the microchamber to stop evaporation after cell loading.

A low-current potentiostat (CV-37, BAS) with data acquisition software was used to characterise the microfabricated enzyme-modified electrodes and to monitor the lactate produced from a single cell. The lactate response was measured amperometrically at +640 mV *vs.* Ag|AgCl, recording the oxidation of enzymically produced H_2O_2.

4.3.3.4 Single-Cell Electropermeabilisation

Single isolated cells were placed in the chamber, and following experimentation, were electropermeabilised by the application of electric fields of 500 V cm^{-1} (equivalent to 10 V/ 200 μm) with 40 μs duration.

4.3.4   Light Microscopy Fluorescence Imaging Setup

A schematic drawing of an imaging fluorescence microscope was shown in Figure 4.1.
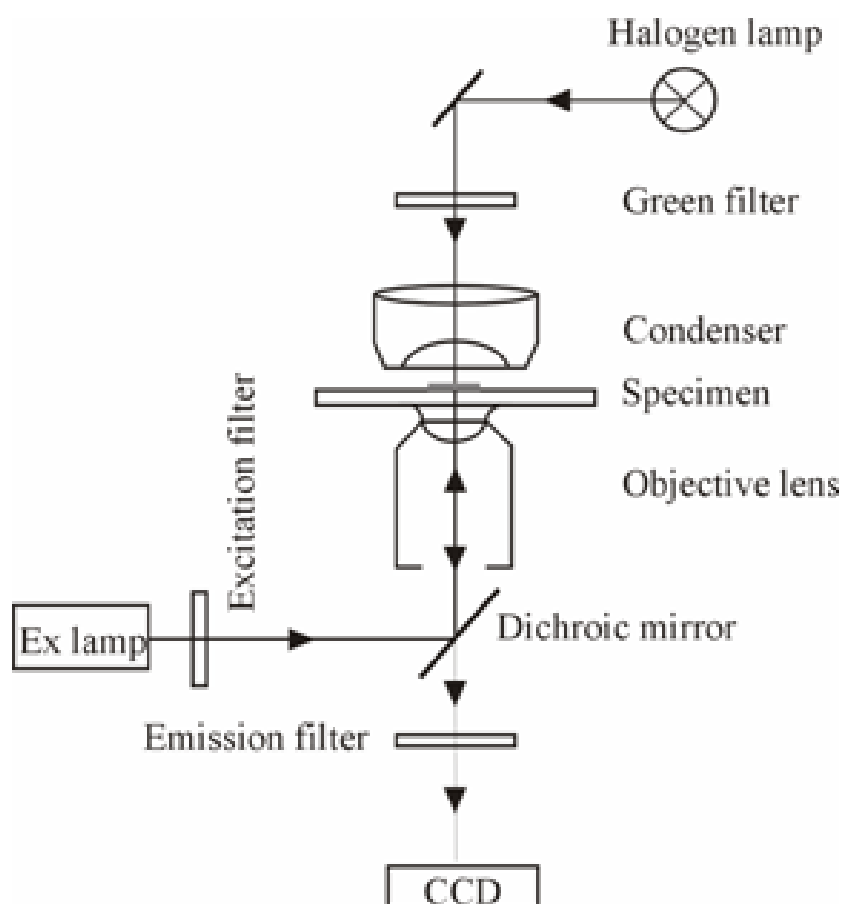
Figure 4.1 Schematic drawing of an imaging fluorescence microscope. Light from the excitation lamp (Ex lamp) was filtered by an excitation filter and reflected towards the objective lens by a dichroic mirror. Fluorescence emitted by the sample was collected by the same objective lens and focused onto a CCD camera after passing through the dichroic mirror and the emission filter.

The design of this setup was characterised by the use of a single objective lens, through which excitation light is focused onto the subject of interest and the emitted fluorescence light is collected and transmitted to the detector. This is made possible by the use of a dichroic mirror, which reflects some specific wavelengths but transmits fluorescence light of other wavelengths. Background is minimised by using possible filter sets comprising an excitation filter, an emission filter and a dichroic mirror. The optical conditions were optimised for the specific fluorophore of interest. Efficient excitation can be achieved using light sources of high power, such as halogen or mercury lamps or laser sources. By using a high objective lens, both efficient excitation and efficient collection of the emitted fluorescence light are ensured. Finally, efficient detection of the fluorescent light emitted

within the bandwidth of the emission filter was ensured by the use of highly sensitive detectors, such as photomultiplier tubes and a CCD camera.

4.4 Results and Discussion

4.4.1   Design and Fabrication

A micrograph of the device is shown in Figure 4.1(a). The five-electrode-system comprises a three electrode microbiosensor with working electrode (A), reference electrode (B), and counter electrode (C), together with the two stimulating electrodes (D, E). A single cardiomyocyte is shown within the microchamber. Considerations for the design and fabrication of these electrodes have been discussed in Chapter 2. Noticeably, direct contact with the reference electrode would result in immediate hypercontraction of the cell, as shown in Figure 4.2 (b), the cell balled up rapidly after a few minutes beating and contracture, due to the toxicity of Ag^+, which might compromise the original cell membrane of the heart cell. Therefore, this must always be avoided by manipulating the cell to the desirable position before it finally settles down. And, in the feature of design, the reference electrode was designed with a small size.

(a)
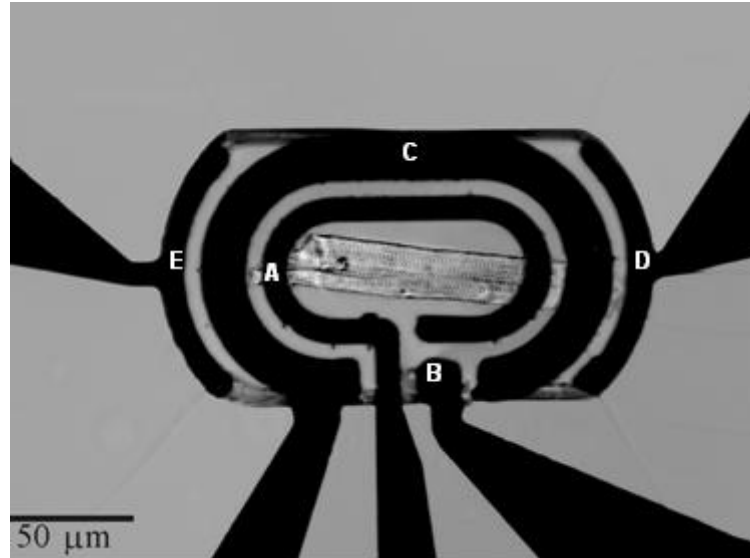
(b)
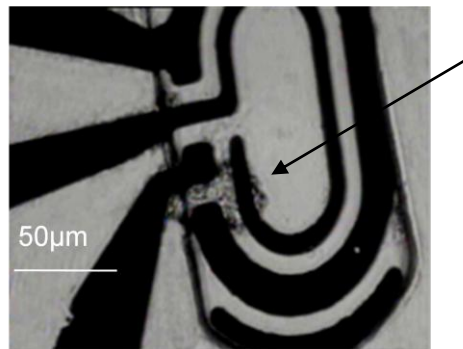
Figure 4.2 (a) micrograph of microelectrodes and microchamber pattern (depth 20 µm) with different functional microelectrodes indicated as A, B, C, D, E. A quiescent cardiomyocyte was transferred into the microchamber; (b) single-cell hypercontraction (the cell, indicated by arrow, balled up after a few minutes beating and contracture by the contact of Ag|AgCl microelectrode, due to the toxicity of Ag$^+$.

4.4.2 Single-Cell Contraction by Field Stimulation

Isolated ventricular myocytes were stimulated with monophasic or symmetric biphasic pulses (1.5–2.0 V per phase). After cell placement, with the myocyte in contact with either the glass or metal surface, there is ca. 1 minute before cell adhesion starts. During this time, the cell could be readily manipulated into an orientation with respect to the axis

of the stimulatory electrodes. It was found that the threshold voltage to enable the cell to be paced electrically was ca. 1.5 V (ca. 75 V/cm). Immediately after adhesion to the surface, the cell was forced to beat continuously by applying electrical fields (1.5 V/ 200 μm) of varying frequency (0.5–2.0 Hz) across the stimulating electrodes.

4.4.2.1 Conditions for Stimulation of Single Myocytes

To enable electrical stimulation of adult ventricular myocytes within such a format, there are a number of important criteria: (i) the current density within the extracellular space should be sufficient for an action potential to be achieved with voltage amplitudes below the threshold for electrolysis of water (which is above 1.5 V, indicated by local pH change in Figure 4.3) ; (ii) the current pulse should be charge-balanced to avoid electrolysis and polarization of the electrodes; (iii) the polarization of the cell membrane away from rest should not exceed 200 mV to prevent electropermeabilisation [135].

In addition, the two stimulatory electrodes were fabricated within the microchamber so that the cell could be aligned parallel with the electrical field in order that a sufficiently low-voltage stimulatory pulse could be applied (thereby avoiding both electrolysis and polarisation of the electrodes, and minimising the ionic flux caused by stimulation, which might interfere with the measurement) [116].

4.4.2.2 Characterisation of Local pH during Stimulation

The pH change evoked by the high stimulus voltages and electrolytic by-products has the potential to inhibit the metabolism of the cell. To measure the local pH change during the field stimulation, the microchambers were filled with the pH-sensitive dye BCECF (10 μM) buffered with 20 mM HEPES (N-2-Hydroxyethylpiperazine-N'-2-ethanesulfonic acid). Biphasic rectangular pulses of 4 ms duration of alternating polarity with amplitudes between 1.5 V (field strength 75 V/cm) and 2.5 V (field strength 125 V/cm) were applied at 1.0 Hz to the stimulatory electrodes. It was noted that there was no change in the local pH under conditions of lowest field (1.5 V, 75 V/cm), although at increased field strengths 100V/cm and 125V/cm, there were small local changes, as shown in Fig. 4.3. Similarly, as the polarity of the stimulatory pulses was reversed after 25 seconds, the pH

did not change at the low stimulatory field strength of 75 V/cm, whilst the pH was seen to return to more neutral pH at the higher electrical field strengths of 100 V/cm and 125 V/cm. The calculated field strength for a biphasic pulse of 1.5 V across the electrode distance of 200 μm was 75 V/cm for each phase, which exceeded the threshold of 50 V/cm for membrane electroporation [116]. However, electroporation (indicated by the irreversible leakage of Ca^{+2} into the cell) was only detected at 150 V/cm per phase, so the effective field strength at the cell surface was therefore assumed to be a fraction of that calculated, due to attenuation within the chamber.
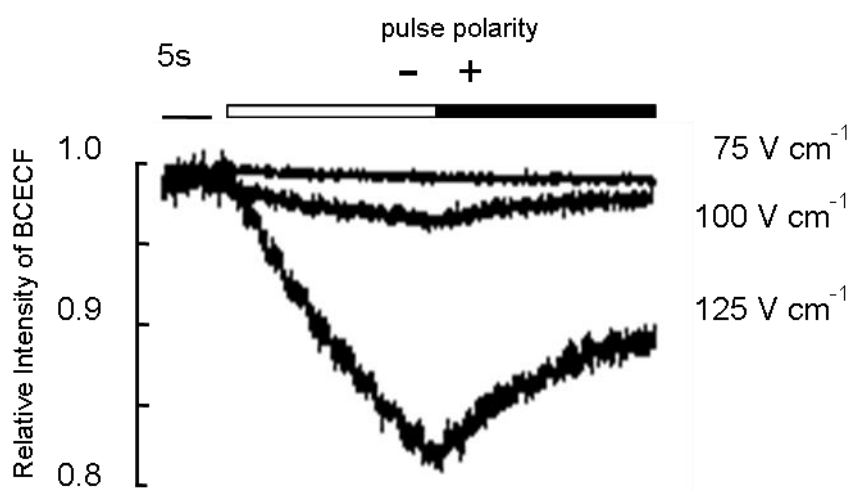
Figure 4.3 Time course of local pH change within the 650 pL microchamber buffered in 20 mM HEPES at field strength above the threshold for electrical stimulation of single myocytes. The change in emission of BCECF was related to the initial emission and plotted as the relative intensity against time. The pH was monitored from a region of 4 μm × 4 μm located 2 μm away from the initial anode within the microchamber. After 25 s of continuous pulsing, the polarity of the pulses was reversed.

4.4.2.3 Continual Pacing of Single Heart Cell

After the single cell had settled down, the optimised stimulus voltage (1.5 V) was applied to pace the cell. The single cardiomyocyte was placed into the microchamber and made to contract with stimulatory pulses at 0.5 Hz, followed by an increased pacing rate of 1 Hz. Cell contraction was simultaneously recorded as the change of the sarcomere length (Figure. 4.4). The regular change of the sarcomere length at any given frequency demonstrated the ability of the cell to produce an action potential upon electrical stimulation within the microfluidic structure.
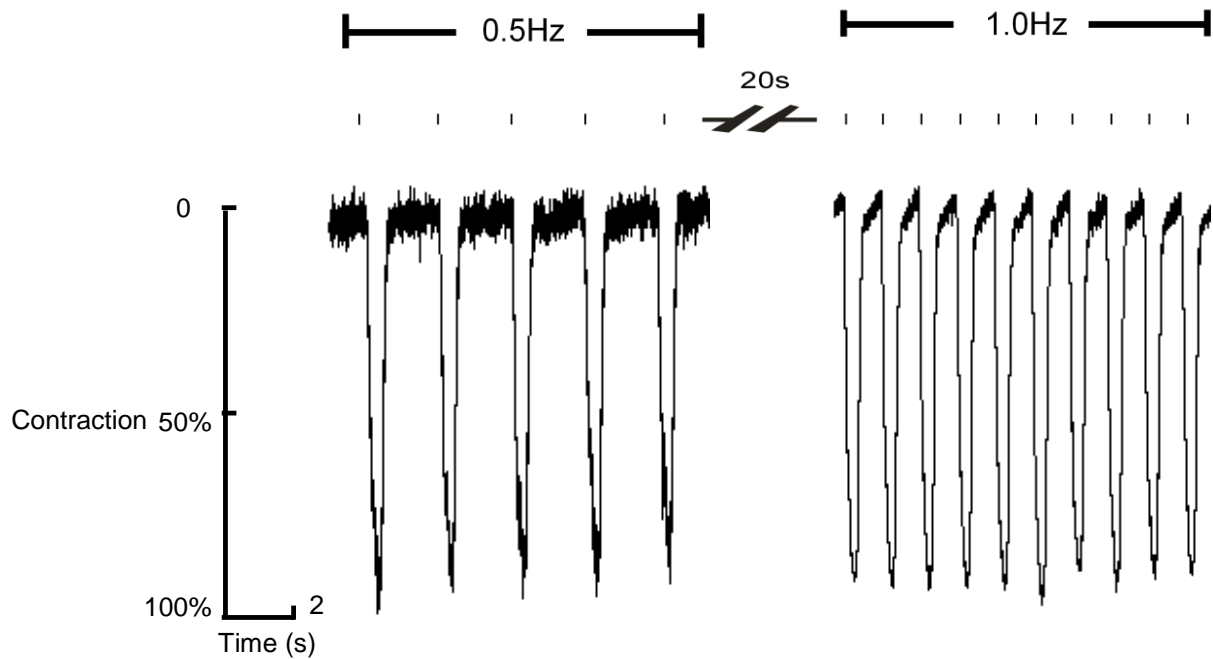
Figure 4.4 The relative mean sarcomere length recorded from the same cardiomyocyte within the microchamber, where 100% indicated the maximum relative degree of contraction with respect to the resting cell. The vertical bars along the horizontal axis indicate the start of each pulse.

4.4.2.4 Anaerobic Metabolism during Stimulation

By applying pulses with higher frequency (2 Hz), the single cardiomyocyte can be "forced" to exercise intensely. Pulses with gradually increased frequency were applied to pace the cell. The frequency of cell contraction was able to keep pace with the frequency of stimulation when the stimulus frequency was less than 2 Hz (as shown in Figure 4.4); however, contraction frequency could not increase further when even higher stimulation frequencies were applied (>2 Hz). Under the condition where the cell was stimulated at extremely high frequency (at 2~3 Hz), the cell could be continuously paced, although with a quickly decreased amplitude of cell shortening, and contraction ceased after a short time (3~5 minutes). Interestingly, the cell could still retain its ability to respond to stimulus when its frequency was set back to a lower level (<2 Hz). This observation indicated that when an extremely high frequency (> 2 Hz) was applied to pace the cell over a short period of time, the rate of ATP production was not sufficient to allow cell contraction at this frequency.

In this case, it could be assumed that anaerobic glycolysis dominates the energy production at higher frequencies (the diffusion rate of oxygen through the layer of mineral oil into the cell buffer is more than sufficient according to previous reports [110], suggesting that there is excess oxygen supply in the microchamber). Therefore, by making the cell undergo intense activity determined by stimulus frequency for a period of time, it is possible that the cell can be effectively simulated as a model of ischemia.

4.4.3   Intracellular Ca^{2+} During Continuous Pacing of the Aerobic Cell

To investigate further the pacing of the aerobic cell, Ca^{2+} transients from single, continually paced cardiomyocytes were recorded using Fluo-3 emission. An isolated Fluo-3-loaded cardiomyocyte was placed into the microchamber and made to contract with stimulatory pulses at 0.5 Hz, followed by an increased pacing rate of 1 Hz (Fig. 4.5). The cell shortened in response to the rise in intracellular $[Ca^{2+}]$ and relaxed after the reuptake of the released Ca^{2+}, indicating normal excitation-contraction coupling (EC coupling). The time course of the Ca^{2+} transients and the sarcomere length change were similar at 0.5 Hz and 1.0 Hz.
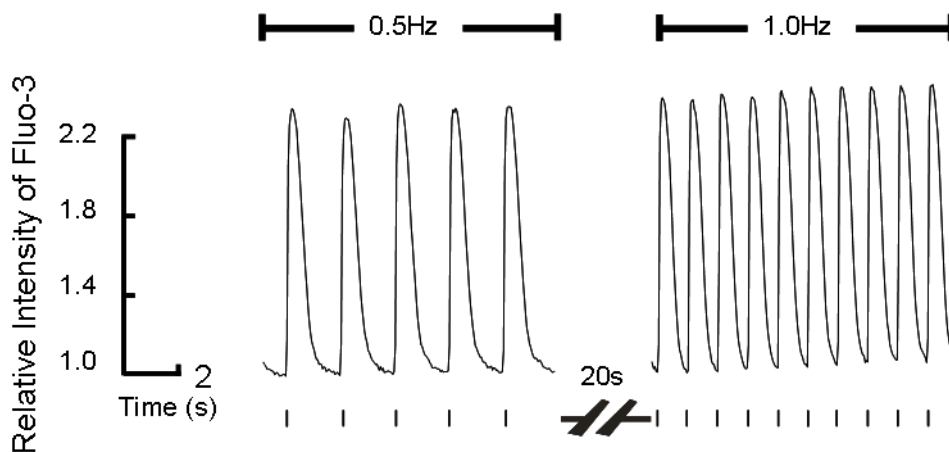
Figure 4.5 Intracellular Ca^{2+} transients from Fluo-3 indicator-loaded single cardiomyocytes stimulated at a field strength of 75 V/cm and frequencies of 0.5 Hz and 1.0 Hz. The vertical axis gives the relative fluorescence intensity, and the vertical bars along the horizontal axis indicate the start of each pulse.

4.4.4 Continual Pacing and Stimulated Metabolism of the Anaerobic Cell

4.4.4.1 Shortening of Contractility

Single cardiomyocytes were continually stimulated in the microchamber by pulses of electrical field strength 75 V cm^{-1} at 1.0 Hz. The effect of continual pacing on the contractility of single myocytes was investigated as the relative amplitude of cell shortening with respect to that at rest (100 %), as shown in Fig. 4.6. Within the restricted extracellular volume of 650 pL, the myocyte was continually stimulated for ~20 minutes, during which time the amplitude decreased to ca. 20% of maximum.
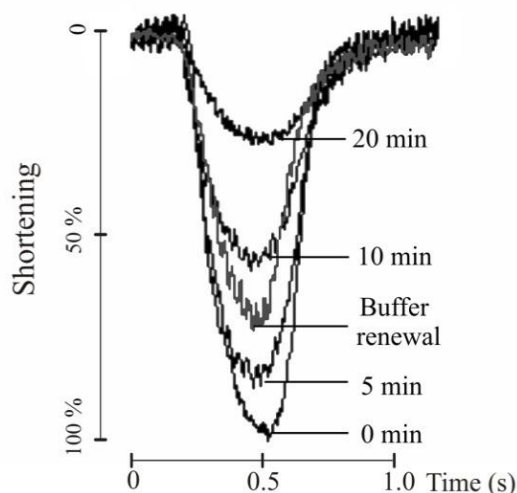
Figure 4.6 Myocyte contractility measured as the change of the sarcomere length within the chamber when stimulated with an electrical field strength of 75 V/cm at 1.0 Hz. Single representative transients from a continuous record are shown. The values on the right-hand side represent the period from the development of steady-state shortening.

The fall in the contractility of the cell could be caused by the acidification of the intracellular or extracellular space. As discussed previously in this Chapter, there was evidence that anaerobic glycolysis would be involved to provide most of the adenosine triphosphate (ATP) required for cell contraction after a period of continual contraction. When glycolysis proceeds rapidly, the proton builds up as a by-product. The consequent decrease in intracellular pH would inhibit further glycolysis and contraction. The cell is

able to restore the intracellular pH by alternative pH regulatory mechanisms, one of which involves lactic acid transport out of the cell [136, 137]. We do not presume that the lactate is the cause of the decreased intracellular pH or the reverse, though intracellular lactate also accumulates during glycolysis. The relation between intracellular pH and lactate will form a further discussion). However, the defined volume of the microchamber utilised in this study does not allow the proton that is transported out of the cell to be carried away, which could explain why partial recovery (60 % relative to that at the rest) of shortening amplitude was achieved after renewal of the buffer: buffer renewal could help carry away the released proton and partly balance the falling pH of the extracellular space.

4.4.4.2 Real-time Extracellular pH during Cell Continuous Contraction

To investigate whether there was acidification of the extracellular space after continuous pacing of the cell, as described above, the extracellular pH was monitored in real time during 20 minutes of continuous cell contraction using semi-quantitative single wavelength fluorescence of BCECF (Figure 4.7. a, b). It was found that after 10 minutes of continuous pacing, the relative extracellular pH decreased by ~2%, and by ~5% after 20 minutes of continuous pacing. If we assume the resting extracellular pH is 7.4, the extracellular pH decreased to ~7.2 after 10 minutes and ~7.0 after 20 minutes. Accordingly, the contractility of the same cell was measured in real time using edge detection measurement as a function of contraction time. It was also noted that after 10 minutes of continuous pacing, the relative shortening decreased by ca. 25%, and by over 40% after 20 minutes of continuous pacing, indicating that the decrease in the contractility of the cell could be associated with the fall in extracellular pH. Again, renewal of the extracellular buffer led to partial recovery of the shortening amplitude (60 % relative to that at the rest).

Considering there was no electrolytic acidification within the microchamber (as shown in Figure 4.3), it might be expected that the acidification of the extracellular space would be contributed to by the efflux of protons from the intracellular into the extracellular space, as the number of protons increases dramatically as a by-product of anaerobic glycolysis and they accumulate within the intracellular space.
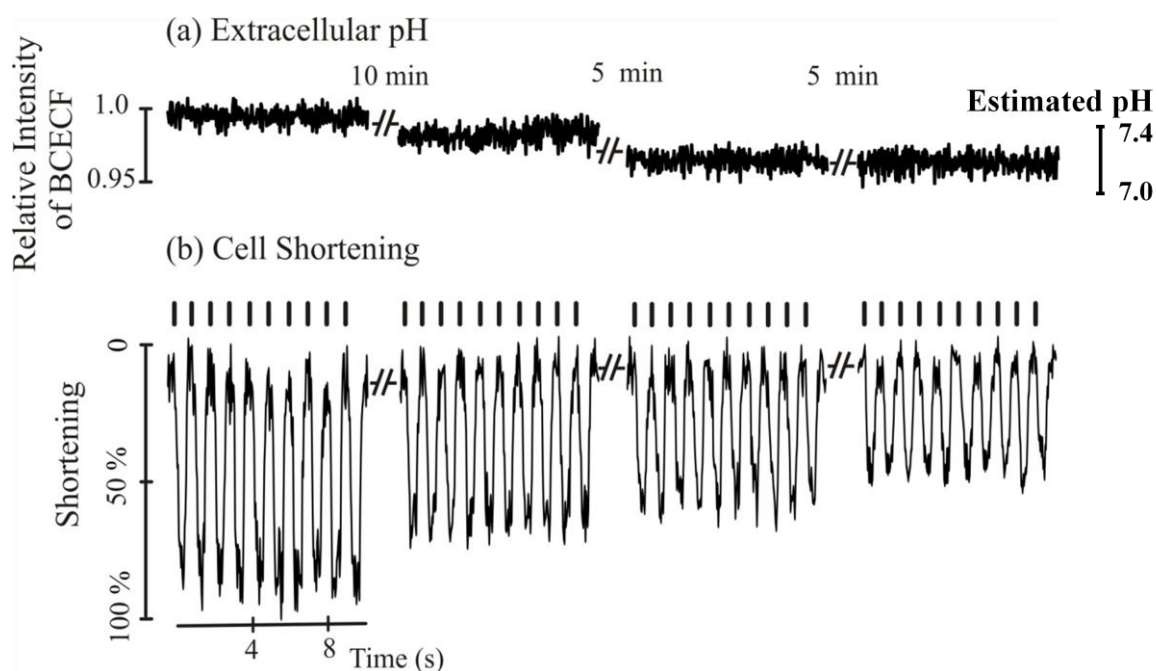
Figure 4.7 (a) Recordings of extracellular pH during continuous contraction with a field strength of 75 V/cm and a frequency of 1.0 Hz (as indicated by vertical bars, which mark the point of electrical stimulation), using semi-quantitative single wavelength fluorescence of BCECF. (b) Simultaneous recording of cell contraction with field strength of 75 V/cm and a frequency of 1.0 Hz, using edge detection measurement.

4.4.5 Detection of Ultra-low Amounts of Intracellular Lactate from Single Heart Cells

Evidence has been shown in Section 4.4.4 that the contractility of a single heart cell was associated with extracellular pH change during continuous contraction. In the following section, we investigate the cause of this extracellular pH decrease. The real-time measurement of intracellular pH during continuous stimulation will be discussed in the next chapter to advance our understanding of this acidification mechanism. As discussed in earlier sections in this Chapter, lactate may also be a possible factor to contribute to the intracellular acidification mechanism. When glycolysis proceeds anaerobically, the production of lactate also increases and it accumulates within the intracellular space. The cell attempts to restore the local pH, involving lactic acid transport out of the cell. Here, we use a successfully established novel electrochemical micro-fabricated device involving a system of three enzyme-modified micro-fabricated electrodes, achieving a minimum detection limit for lactate of 4.8 fmol (equivalent to the detection of ca. 7.4 µM

considering the chamber volume of 650 pL, or ca. 0.12 mM considering the single cardiomyocyte volume of 10 pL – as described in Chapter 3), to directly monitor intracellular lactate from single heart cells.

4.4.5.1 Single-Cell Permeabilisation

Permeabilisation of the cell plasma membrane was achieved by exposing the cell to large electric fields of short duration. This technique, known as electroporation or electropermeabilisation, enabled the investigation of the intracellular chemistry of an isolated cell [138]. Several applications of cell permeabilisation have been identified, with *in vitro* reversible electropermeabilisation widely used to transfect cells by introducing DNA and proteins and to enable the local delivery of relatively membrane-impermeable anticancer drugs. Electrical pulses of amplitudes that are too high, however, lead mostly to irreversible permeabilisation (electroporation) and therefore to cell death. In order to investigate intracellular lactate, in this study, a voltage pulse of 10 V with 0.04 ms duration was applied across the microelectrodes (separation of 200 μm) irreversibly to permeabilise the single cell. This resulted in cell hypercontraction, allowing intracellular lactate to diffuse freely into the extracellular surroundings without an active pump mechanism.

4.4.5.2 Lactate Released from Single Permeabilised Heart Cells

The concentration of intracellular lactate usually present during aerobic respiration is ~2 mM within a cardiomyocyte of 10–20 pL volume [139]. To understand the nature of the ionic currents resulting from the stimulation pulse, control experiments were carried out by applying the same electrical pulse but in the absence of the cell (Fig. 4.8 (a)). The integral of the i-t curve (giving the charge Q) obtained was below that of the equivalent titre of lactate, as illustrated in Figure 4.8 (b).

Lactate was released from the cell immediately after the high pulse was applied. Fig. 4.8 (b) shows a typical electrochemical response of lactate released from a single myocyte after electropermeabilisation.
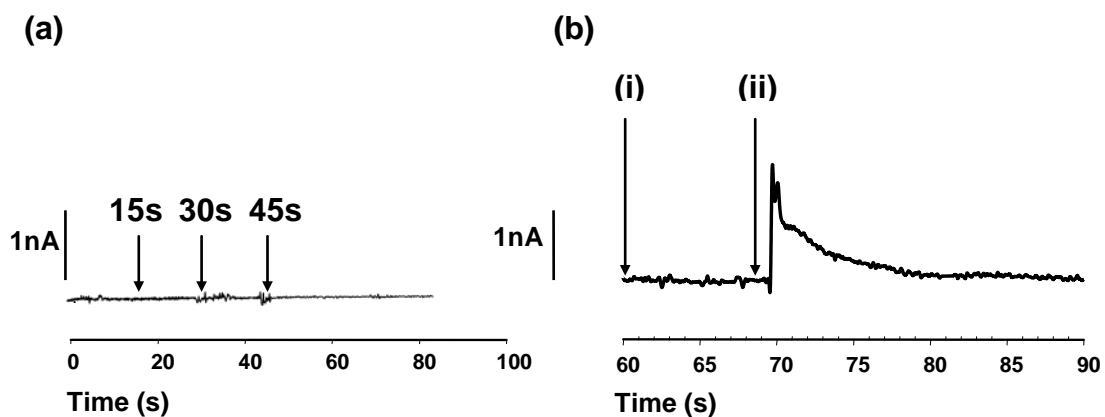
Figure 4.8 (a) The effect of applying short high-voltage pulses (10 V, 0.04 ms) at 15 s, 30 s, and 45 s in the absence of the cell. (b) Typical responses to lactate released from an electropermeabilised cell: (i) in the absence of pacing, when no lactate was present in the extracellular space; (ii) electrochemical response as lactate was released from the single cardiomyocyte after electropermeabilisation. The modified sensor was poised at 0.64 V *vs.* integrated Ag|AgCl microreference.

Using the calibration curve, as demonstrated in Figure. 4.8, we estimated that in total ca. 20 fmol lactate was detected. Assuming that all the intracellular lactate was released and constrained within the microchamber, the average concentration of intracellular lactate is estimated to be 2.0 ± 0.1 mM (n = 3, assuming a myocyte volume of 10 pL), consistent with the normal values obtained from single healthy aerobic cells [110, 139].

Table 4.1 shows the responses of individual cells (3 cells) to electropermeabilisation.

	Total quantity of measured lactate (fmol)	Estimated intracellular lactate concentration (mM)
Cell 1	19	1.9
Cell 2	21	2.1
Cell 3	20	2.0

4.4.5.3 Preliminary Study of Lactate Monitoring from Single Anaerobic Cells

In order to produce a model of anoxia, a single myocyte was poisoned by microinjecting carbonylcyanide p-(trifluoromethoxy)-phenylhydrazone (FCCP) into the chamber, inhibiting aerobic glycolysis. The anaerobic system would then be used to generate ATP, with a net production of lactate.

Figure 4.9 shows the lactate production from a single myocyte, electropermeabilised after metabolic inhibition by injection of FCCP (2 mM). The working electrode was poised at 0.64V *vs.* an integrated Ag|AgCl pseudo-reference electrode. The cell contracted slightly in response to the injection of 2 mM FCCP. Lactate efflux was not observed until the cell membrane was electropermeabilised by the application of electric fields of 500 V cm^{-1} (equivalent to 10 V/200 μm) with 40 μs duration, at which point the cell immediately shortened and balled (indicate the cell death). The lactate signal after electroporation corresponded to the efflux of ca. 150 fmol (corresponding to an intracellular concentration of ca. 15 mM) lactate into the extracellular space. This data with cells equilibrated with the mitochondrial inhibitor FCCP indicated that lactic acid production was considerably increased: the lactate signal after electroporation was ~8x larger than that from electropermeabilised healthy cells.

(a)
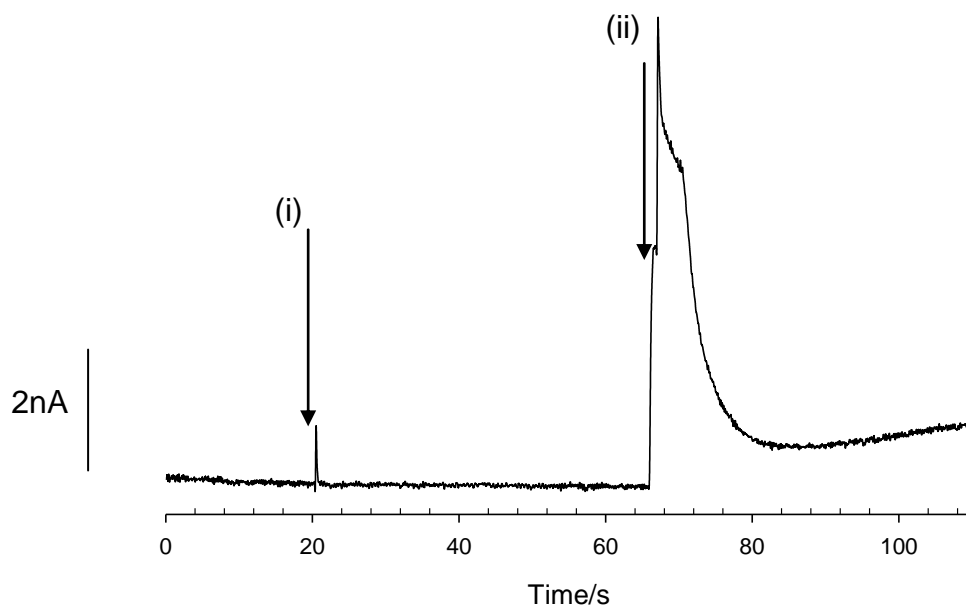
(b)
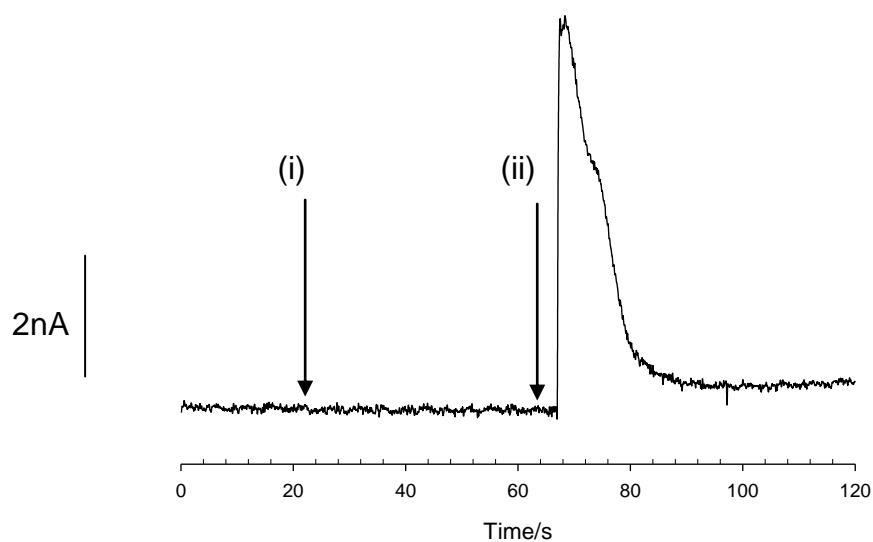
Figure 4.9 (a), (b) Typical electrochemical monitoring of lactate released from a single rabbit myocyte electropermeabilised after metabolic inhibition, imposed by injecting 2mM FCCP. The working Pt electrode was poised at 0.64 V *vs.* an integrated Ag|AgCl pseudo-reference electrode. (i) Injection of FCCP, at which point the cell contracted a little in response to the injection. (ii) Electrochemical response as lactate is released from the single cardiomyocyte after electropermeabilisation by the application of electric fields of 500 V cm^{-1} with 40 μs duration, at which point the cell immediately shortened and balled.

117

4.4.6 Device Fouling and Regeneration

4.4.6.1 Passivation of Electrode

The adsorption of electro-inactive species on an electrode surface occurs frequently. Such adsorption can inhibit an electrode reaction by the formation of an impervious layer that blocks a portion of the electrode surface. Both the Pt working electrode and Ag|AgCl reference were fouled by the released cellular debris after a number of cell experiments. The fouling of the working electrode could be identified by higher signal noise levels (>100 pA) and a smaller active electrochemical area, which can be ascribed to the build-up of adsorbed impurities on the electrode surface. Direct contact of the strongly oxidizing AgCl layer with a single myocyte causes the myocyte to die rapidly. This poor biocompatibility of Ag|AgCl electrodes leads to the degrading of the Ag|AgCl, indicated by a shift in the reference potential after a cell assay. Cell assays were therefore only conducted for 1 hour.

4.4.6.2 Regeneration of electrodes

Both the Pt working electrode and the Ag|AgCl reference electrode were therefore cleaned using a lower power dry etching. Figure 4.10 is a typical comparison of the device DC cyclic voltammograms at 100 mV/s with 1 mM FMCA before and after a dry etching process (oxygen plasma). Prior to the etch, the device had been used for extensive cell tests and was completely passivated by debris and oil, as shown in curve (i). After dry etching, its DC cyclic voltammogram returned to a normal response (ii), showing increased response currents to the same concentration of FMCA, indicating the working electrode was regenerated.
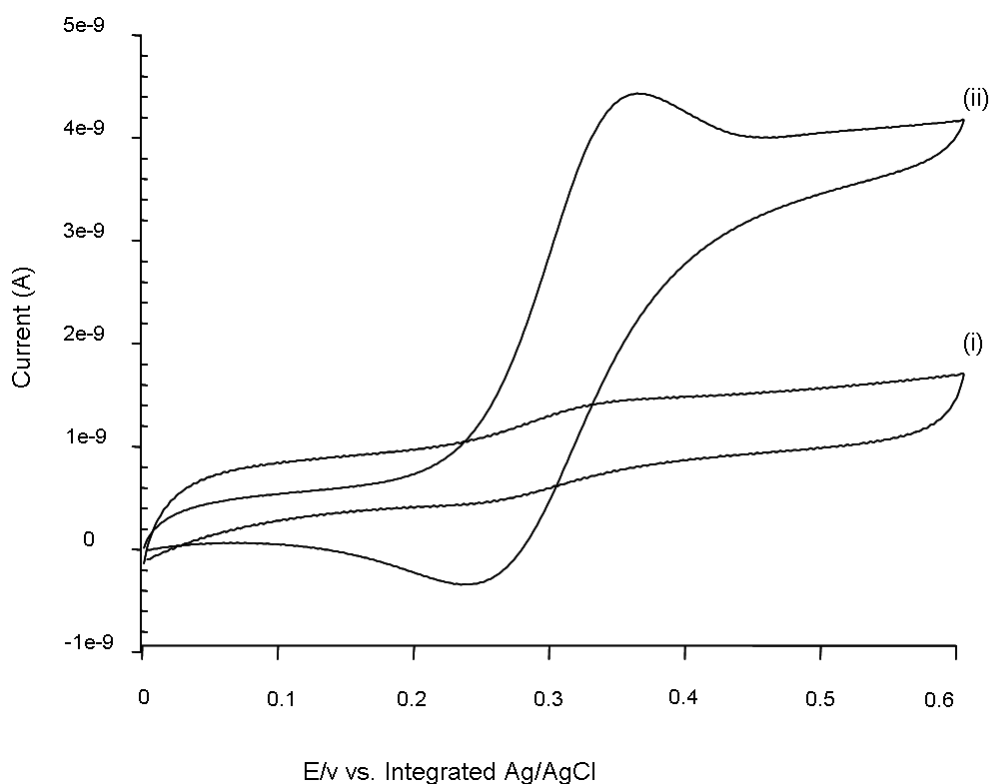
Figure 4.10 Comparison of the device DC cyclic voltammograms at 100 mV/s with 1mM FMCA before (i) and after (ii) a dry etching process (oxygen plasma). The device had been used for extensive cell tests and was completely passivated by debris and oil, as shown in curve (i); (ii) after dry etching, its DC cyclic voltammogram returned to a normal response.

Not only was the working electrode surface cleaned, but the contaminated Ag|AgCl reference electrode was also partly re-activated by the dry etching followed by the electrochemical deposition of a new thin layer of AgCl. Device regeneration was repeated after each cell assay, such that the regenerated device was able to respond repeatedly to lactate whilst the passive device failed. A complete solution to circumvent the electrode fouling would involve the development of a sensor array by using a large common Ag|AgCl of relatively large area and an array of working electrodes separated by multiple microreservoirs, with each containing a single heart cell to be analysed (discussed in Chapter 5).

4.5 Conclusion

In this chapter, we describe the study of ionic and metabolic fluxes from single active, beating heart cells on the microfabricated device. A single myocyte was manipulated within the SU-8 microchamber and paced at the optimised field stimulation (75 V/cm) without local pH change. Cell contraction was simultaneously recorded as the change of the sarcomere length upon the electrical stimulation within the microfluidic structure. The change in intracellular $[Ca^{2+}]$ from a single Fluo-3-loaded cell in response to the cell shortening upon stimulatory pulses of low frequency was monitored optically, indicating normal EC coupling. In a model of anoxia, the amplitude of cell shortening decreased to ca. 20% of the maximum after 20 minutes of continuous stimulation. Accordingly, the relative extracellular pH was optically monitored in real time as a function of the amplitude of cell shortening, with a ~2% and ~5% decrease after 10 and 20 minutes of continuous pacing respectively, indicating that the decrease in the contractility of the cell could be associated with the fall in extracellular pH.

Further, the integrated microelectrodes were configured as an enzyme-linked lactate microbiosensor, and were used to measure the amounts of lactate produced by the heart cell. We demonstrated the efflux of lactate into the extracellular space after the single cell was permeabilised. In total, ca. 20 fmol lactate was detected from a single aerobic myocyte, giving an estimated average concentration of intracellular lactate of 2.0 ± 0.1 mM. In a preliminary study of an anoxia model, in total ca. 150 fmol lactate – equivalent to an intracellular lactate concentration of 15 mM – was detected from the extracellular space with a cell equilibrated with 2 mM of the mitochondrial inhibitor FCCP. The electrodes of the device needed to be regenerated by dry etching after each cell assay. The integrated Ag|AgCl electrode particularly showed poor biocompatibility with the cell assay, causing the degrading of the reference electrode. A sensor array is proposed to circumvent this problem in the next study.

Chapter 5 Monitoring Single Electrically Stimulated Heart Cells within Arrays

5.1 Introduction

Following the single-cell assay based on the microfabricated device, in this Chapter we present a robust microfluidic array, where the sensor arrays are integrated within an array of PDMS chambers. There are two significant advantages over the single chamber device, namely: firstly, the array of hydrophobic PDMS chambers structured on a hydrophilic glass substrate enabled easy manipulation and location of single heart cells with the potential for the parallel handling and analysis of single cells; secondly, the device has a large single common Ag|AgCl reference electrode and an array of working electrodes separated by multiple microreservoirs, with each separate analytical chamber containing a single heart cell to be analysed. The device's working and reference thus does not require the regeneration when obtaining multiple measurements from single cells.

In this Chapter, we first describe a microperfusion system, which we used to manipulate a single heart cell in the microfluidic device, and which we coupled to the detection system to characterise the sensor array when lactate was microperfused or dispensed with extremely low volumes (13 pL), into the analytical system. The single heart cell was manipulated in the microfluidic system in such a way that the hydrophobic character of the PDMS microchamber efficiently allowed direction of the cells into their chambers. The single heart cells were electrically stimulated to contract for a prolonged time. The amplitude of the cell shortening as well as the intracellular Ca^{2+} fluxes from the continuously contracting single heart cells were then studied. The monitoring of intracellular pH using fluorescence was also undertaken from a single beating heart cell whose electrical and metabolic state was controlled. The mechanism of intracellular H^+ change is then discussed in relation to extracellular pH change. In an attempt to measure lactate release from the electrically stimulated contracting cell, the possible cause of intracellular pH changes was investigated. The underlying relationship between intracellular pH and lactate in a single heart cell with a controlled metabolic state was also investigated.

5.2 Materials and Methods

5.2.1 Materials

All solutions were prepared using high-purity deionized water (Millipore Elix 10) and analytical reagent grade chemicals, without further purification. Unless otherwise stated, all chemicals were obtained from Sigma-Aldrich (Dorset, UK). Lactate solutions, for sensor calibration, were prepared as stock solutions in appropriate buffers immediately prior to their use. The supporting electrolytes were 10 mM phosphate buffered saline, PBS (10 mM phosphate buffer containing 2.7 mM KCl and 137 mM NaCl, pH 7.4). Single adult rabbit ventricular myocytes were isolated from the left ventricle by perfusion of the heart with collagenase solution. Cells were maintained in Krebs Base Solution (KBS) containing 120 mM NaCl, 20 mM sodium *n*-hydroxyethylpiperazine-n'-2-ethane sulphonic acid, 5.4 mM KCl, 0.52 mM NaH_2PO_4, 3.5 mM $MgCl_2$, $6H_2O$, 20 mM taurine, 10 mM creatine, 11.1 mM glucose, 0.1% BSA, and 1.8 mM $CaCl_2$, pH adjusted to 7.4 with 100 mM NaOH. Extra-cellular medium was also used, which contains appropriate ionic concentrations to allow excitation-contraction of cells. All the dyes (including Fluo-3 and BCECF-AM) are purchased from Molecular Probes (Eugene, OR, USA).

5.2.2 Fabrication

All procedures for the microfabrication of the microelectrode array and PDMS multi-channels have been detailed in Chapter 2. Briefly, masks for all microelectrodes and microchambers were designed in L-Edit™ and produced as chrome-coated maskplates using a Leica EPBG5-HR electron beam writer (Leica, Germany); the mask design was described in Section 2.3.1. The microelectrodes were patterned onto the cleaned glass slide using standard photolithographic methods including metal evaporation, electrochemical metal deposition and lift-off, as detailed in Section 2.3.2. The process of fabrication the PDMS multi-chamber started with a finalised microelectrode array pattern including an electrochemically structured Ag|AgCl reference electrode. The PDMS multi-chamber was realised by spin-coating a thin PDMS layer (using 12, 24, 36 μm thick AZ4562 master mould) followed by dissolution, leaving the microchamber structure, as detailed in section 2.4.2.

5.2.3 pL-Scale Microperfusion System

A single fused silica capillary was pulled to produce a tip with ~10 μm inner diameter to fill the PDMS microchamber. However, the size and shape of the droplet were affected by a multitude of factors such as pressure as well as pipette tip radius and shape, making the dispensed volume difficult to control. If the droplet from the tip was too large and covered the top surface of PDMS between two channels, the top surface of PDMS became less hydrophobic, making the buffer spread over the surface rather than fill the channel when refilling in the future. Leakage of a large droplet from the capillary was thus always avoided. A dual pipette system, which involved an inner and outer capillary, was developed to resolve this problem. In this dual pipette, flexible fused silica capillary tubing with bore sizes of 100 μm and 536 μm respectively (Composite Metal Services Ltd, Ilkley, UK) were pulled on a custom-built puller to produce tapered tips with an opening of ~5-10 μm for the small capillary and of ~30-100 μm for the large capillary.

The small capillary was filled through its tip with the saline solution, which was then pressurised by using a syringe pump (<10 mbar) or by hydrostatic pressure, and inserted into the larger capillary so that the tip extruded <20 μm. The inner tubing contacted the inner wall of the outer tubing, thus generating a capillary with filament with the resulting strong capillary forces. The excess fluid from the inner tip was aspired into the outer pipette by the strong capillary force without the need for another pump. This arrangement restricted the range of the efflux to a half circle of ~20 μm around the inner tip, and at the same time generated a continuous flow from the inner to the outer tip. This dual pipette system has two possible applications in this study: the first use was to fill the PDMS channel without excess buffer; the second application was to characterise the sensor array when the analytical chamber was microperfused with electrochemical analytes such as lactate. Both applications will be discussed in the following sections.

5.2.4 PDMS Chamber Filling

A layer of mineral oil was placed over the array of microchannels to prevent rapid evaporation of any buffer that is placed into a channel. A fused silica capillary was pulled to produce a very small tip with ~10 μm inner diameter. Cell buffer solution was loaded into the microfluidic tubing with a syringe. The tubing was coupled to the

capillary tip. The tip was brought into the microchannel, against the glass substrate surface and a small expulsion of pressure was applied to the syringe, which allowed a droplet to be expelled from the tip of the capillary and, by the insertion and removal of the tip, to wet one portion of the channel. The tip was then moved to a proximal channel, and by expulsion of another droplet, the region was wetted. By repeating this wetting, this eventually attracted to the wetted areas and enabled the array to be filled. Though this wetting process appears elaborate, the buffer evaporates over a few hours leaving a layer of ionic salts and proteins, and this hydrophilic surface of substrate formed by the "priming filling" allows easy re-filling of the channel by simply expelling a small droplet from the capillary tip, which sits on the side wall of the microchannel. The small droplet can then be reduced and moved away using the tip, leaving a filled microchannel.

During the filling of the PDMS channel, excess saline solution would be generated and would accumulate on the PDMS channel; without it being removed sufficiently, it could render the top surface of PDMS between the channels hydrophilic, making the single cell adhere on the top surface of PDMS between the channels rather than be directed inside the channel and sediment to the glass surface. Excess saline solution can be avoided by using the dual micropipette system described above. In this system, the inner (thinner) tubing contacts the inner wall of the outer (thicker) tubing, thus generating a capillary with filament with the resulting strong capillary forces. These forces are sufficient to aspire the excess fluid during the course of the experiment without the need for another pump.

5.2.5   Enzyme Immobilisation

The enzyme was immobilised on the electrode using the exactly same method as described in Chapter 3. Briefly, PBS buffer (pH 7.4) containing LOD enzyme (200 units/ml) was pre-loaded into the PDMS channel using the methods described, such that the enzyme was pre-adsorbed onto the working microelectrode surface at 4°C over-night. A supporting electrolyte solution of 50 mM PBS containing 50 mM KCl and 30 mM *o*-phenylenediamine was then loaded into the PDMS channel. A thin film of poly(*o*-phenylenediamine) was then electrochemically deposited on the electrode to entrap the

pre-adsorbed enzyme using cyclic voltammetry by scanning the applied potential at a rate of 50 mV s^{-1} for 6 minutes between 0.0 and +0.80 V *vs.* Ag|AgCl quasi-microreference. Due to the resistance of the polymer film, the growth is self-limiting, and typically the resultant current falls to a steady-state value within a minute, producing a film of defined thickness and composition. After the polymer growth was completed, the device was washed thoroughly in the working buffer and stored at 4°C.

The cyclic voltammograms obtained during the oxidation of *o*-phenylenediamine in 50 mM PBS buffer (pH = 7.4) containing supporting electrolyte are shown in Figure 5.1. These cyclic voltammograms during polymerization of *o*-phenylenediamine show that after the fifth scan, the oxidation current has decreased almost to background levels, indicating little further deposition of polymer film.
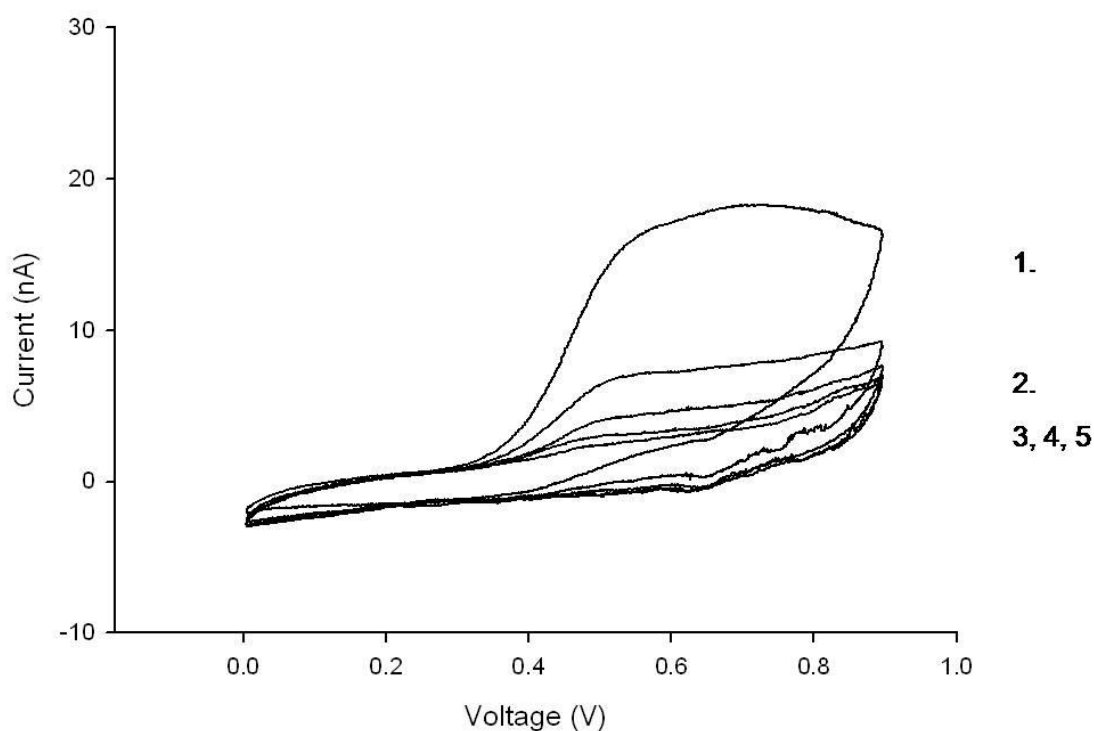
Figure 5.1 Cyclic voltammograms at scan rate 50mV/s obtained during the oxidation of o-phenylenediamine in 50 mM PBS (pH = 7.4) containing 50 mM KCl and 30 mM o-phenylenediamine.

Immobilisations of enzyme on the microelectrode array at the same time before PDMS channels are patterned have been attempted. However, it was found that in this way, enzyme was more likely to be denatured by the series of procedures used to pattern the PDMS and eventually became inactive. Therefore, enzyme was immobilised on each electrode in an individual microchannel, as required.

5.2.6 Device Calibration

The array sensor can be characterised and calibrated for L-lactate using the methods, basically based on the enzymatic oxidation of the analytes with lactate oxidase (LOD), discussed in Chapter 3.

A pL-microinjection system has been developed for precise control of pL-scale lactate dispensation (Chapter 3); however, this dispensation system requires relatively high pressure (>100mbar), which is likely to damage the PDMS array structures. Therefore, in this study, a micropipette pressurized with a manually driven syringe pump to <10mbar was used with a pL-scale fountain pen for the positional precision of the fluid aspiration and dispensation from the micropipette. This feature allowed for not only pL-scale dispensation of lactate, but also microperfusion when a dual micropipette was coupled. The dispensed amount can also be estimated using the electrochemical response of lactate.

5.2.7 Experimental Set-up for Cellular Assay

5.2.7.1 Selection of Cells

200 μl cell suspension was dropped into a PDMS microreservoir containing two platinum macroelectrodes connected to a signal generator (isolated stimulator, Digitimer, Welwyn Garden City, UK). A 0.5 Hz square wave signal was used to field-stimulate the cells. The amplitude of the input signal was gradually increased from zero until excitation-contraction of ca. 80% of the cells was observed. A single cell was selected if it contracted in response to a low amplitude stimulus (ca. 5 V cm^{-1}) with regular and uniform shortening.

5.2.7.2 Pacing of Cells

Individual cells were stimulated within the microsystem by applying a biphasic rectangular pulse of alternating polarity, using a custom-built electric field stimulator coupled with a frequency generator. The amplitude, duration and frequency of each rectangular pulse applied to the cell through the pair of stimulatory microelectrodes which was connected to the stimulator through a PCB board.

Sarcomere length changes were recorded with the IonWizard Version 5.0 software, and then converted to give a measure of relative cell length. Alternatively, the cell shortening was measured using off-line edge detection on recordings of the cell contraction. Isolated ventricular myocytes were stimulated with monophasic or symmetric biphasic pulses (1.5–2.0 V per phase).

5.2.7.3 Cell Manipulation and Isolation

The microsystem for single-cell manipulation involved a micropipette (170μm outer diameter, 100μm inner diameter, pulled capillary tip of diameter ca. 60 μm) coupled with a microfluidic connection to a 500 μl gas-tight microsyringe. The syringe was controlled by a micro-precision screw in a custom-built holder. The capillary tip was guided by a glass tube for vertical access to the microscope stage. The system was fixed on three-axis micromanipulators (for x-y-z movement) and filled with KBS buffer before cell handling. The handling of cells in the array will be discussed in details in "Results and Discussion" Section.

5.2.7.4 Investigation of Extracellular Volume

The effect of continual pacing on the contractility of single cardiomyocytes in these three defined volumes (240 pL, 480 pL, 720 pL) was investigated. A 0.5 Hz square wave signal was used to field-stimulate the cells. Relative cell length with respect to stimulation time length was given in these different volumes by recording sarcomere length changes.

Unless specific stated, all the standard cell assay experiments were performed in volume of 480 pL.

5.2.7.5 Dye Loading in Cells

Cells were loaded with Fluo-3 by incubation for ~30 minutes in 20 μM Fluo-3 AM solution (Molecular Probes, Eugene, OR, USA) for the recording of intracellular Ca^{2+} transients. Intracellular Ca^{2+} was monitored using the fluorescence-contractility system of IonOptix (Milton, MA, USA). The Fluo-3 indicator was excited at 490 nm with a TILL monochromator (T.I.L.L. Photonics, Martinsried, Germany), which was mounted on a Zeiss Axiovert 200 (Zeiss, Germany) equipped with a 40x 0.8 N.A. Achroplan PH2 water immersion lens. The contraction of the cell was recorded by passing the light of the halogen lamp through a 680 nm bandpass filter and imaging the striation of the sarcomere onto a 240 Hz frame shift CCD (IonOptix, Milton, MA). In addition, cells were incubated for ~30 minutes in 10 μM BCECF-AM solution (Molecular Probes, Eugene, OR, USA) for recording intracellular pH using the same filter set as for Fluo-3, described previously.

5.2.7.6 Electrochemical Measurement

A low-current potentiostat (CV-37, BAS) with data acquisition software was used to characterise the microfabricated enzyme-modified electrodes and to monitor the lactate produced from single cells. The lactate response was measured amperometrically at +640 mV *vs.* Ag|AgCl, recording the oxidation of enzymically produced H_2O_2.

5.3　　Results and Discussion

5.3.1　Response of Dispensation of pL-levels of Lactate

The PDMS channel was filled with 10 mM PBS buffer using the pulled capillary of sub-micro-bore size, as described above. 1 mM lactate was applied in amounts manually controlled using the pL-scale "fountain pen" dispensation system. The response from each addition was allowed to return to the baseline, indicative that all the injected lactate was completely oxidised with LOD. Results of pL-scale lactate measurements are given in Figure 5.2.
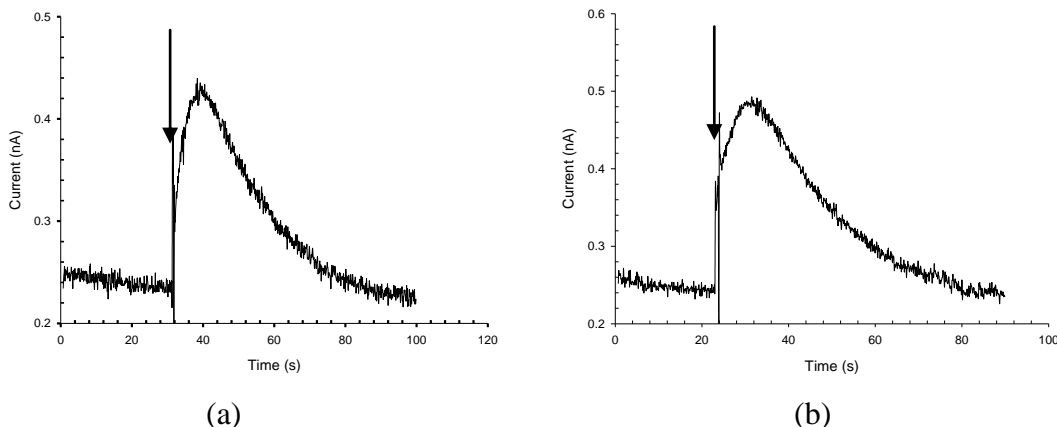
Figure 5.2 (a), (b) Representative current-time response to additions of lactate dispensed by micropipette system, as described in the text. The injection points are marked by arrows. The microelectrode surface area was 1000 μm^2.

As seen in Figure 5.2, each addition resulted in a measurable electrochemical oxidation current with the electrochemical signal returning to the background within 60-70 s, indicating that all of the injected lactate was "consumed" by the enzyme. The diffusion time to achieve the maximum limit current (peak current) is ca. 15s, which is consistent with the theoretical calculation as followings: if assuming the maximum thickness of diffusion layer is 200 μm, which is the maximum distance from one end of the channel to the working electrode; diffusion coefficient of lactate is 8.8 x 10^{-10} m^2 s^{-1} [140], according to the derived equation from Fick's second law for semi-infinite diffusion model [141] $\delta = \sqrt{\pi D t}$ (δ, thickness of diffusion layer; D, diffusion coefficient constant; t, diffusion time), we can estimate that diffusion time to achieve the maximum is ca. 14.5s.

Injection perturbs the electrode double layer, as indicated by the initial spikes, but this perturbing pulse is much less evident than with the equivalent titre of lactate (Faraday current). The charge, Q – corresponding to lactate oxidation, which involves the transfer of two electrons – with respect to the quantity of injected lactate can be calculated with the following equation based on Faraday's constant F (magnitude of electric charge per mole of electrons), assuming that all the transferred charge are attributed by consummation of lactate ($x\ fmol$), with each reaction of one lactate molecular requiring two electrons)

$$\mathbf{Q(nC)} = \mathbf{F\ (nC/fmol)} \times \mathbf{2x(fmol)} = \mathbf{0.1930x\ (fmol)}$$ Equation.5.1

By measuring the total passage of charge, the volume of lactate for each injection can be estimated as 13.0 pL and 26.1 pL in Figure 5.2 (a) and (b) respectively. The detection of levels of lactate as low as 13 fmol can be achieved, indicative of the ability of the device to record the intracellular lactate (>20 fmol) from a single heart cell.

5.3.2 Response to Microperfusion of Lactate

Dual-perfusion pipettes and pL-scale fountain pens were used to provide a microperfusion system, allowing the continuous perfusion of a microchannel without affecting the adjacent channels in the array (in spite of the pitch of 40 μm). During this experiment, the perfusion pipette could be positioned near the surface of a PDMS channel through the linear motion of a piezo translator oriented in the z-direction. When operated in the stepping mode, the inner pipette could be moved in and out of the channel upon a programmed trigger.

A PDMS channel was filled with 10 mM PBS buffer using the pulled capillary of sub-micro-bore size, as described above. 1 mM lactate was perfused through a micropipette pressurised with a manually driven syringe pump to <10mbar. The corresponding flow rate was estimated as 1.4 pL/ms through calibration of the amount of lactate dispensed by the syringe pump.

Figure 5.3 (a) and (b) shows a typical response to perfusion of 1 mM lactate. The arrows marked (i) to (iv) indicate the state of the perfusion pipette (in or out of a microchannel). The continuous perfusion of a microchannel started at (i), at which point the inner pipette was inserted into the microchannel. A steady-state current with a value of ca. 400 pA was then achieved within 20 s, indicative of the steady perfusion by 1 mM lactate at this stage. Removal of the perfusion pipette at time point (ii) saw the current transient gradually return to the background after 80 s.

Perfusion could be re-activated by re-insertion of the perfusion pipette at time point (iii) and a similar steady state current (380 pA) was reached after ca. 10s. Removal of the perfusion pipette at time point (iv) eased the perfusion and saw a gradual return of the current transient to the baseline. The precision of measurement was investigated from three repetitive measurements, where the standard deviation was found to be <6.2 %.
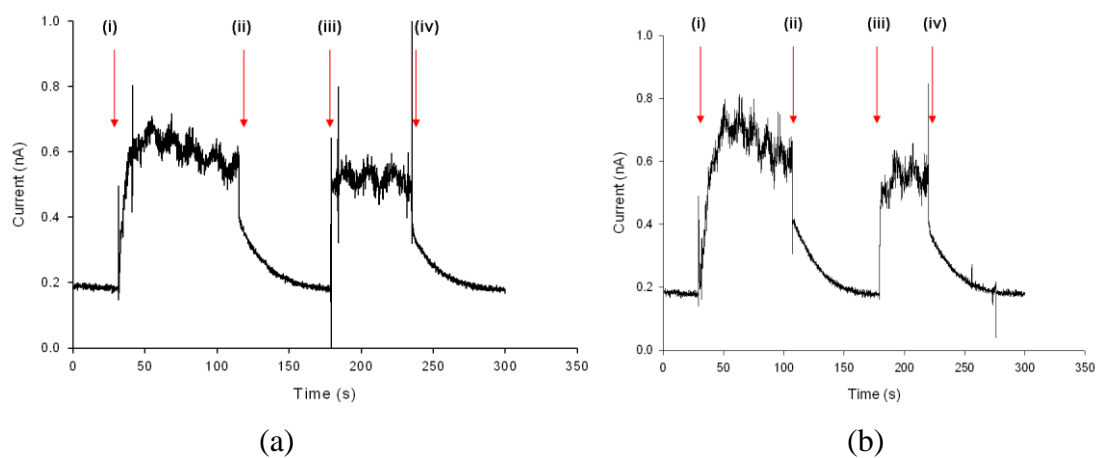
Figure 5.3 a), (b) Response to microperfusion of 1 mM lactate. (i) Insertion of perfusion pipette; (ii) removal of perfusion pipette; (iii) re-insertion of perfusion pipette; (iv) removal of perfusion pipette. The microelectrode surface area was 1000 μm^2.

5.3.3 Single Cardiomyocyte Placement within PDMS Channel

The top surface of PDMS between the microchannels was rendered hydrophobic by an over-layer of mineral oil before cell handling. Compared to the SU-8 chamber, the hydrophobic character of the top surface of PDMS after oil immersion allows easier direction of the cells into their chambers.

Using the methods described previously, the PDMS channel was filled with cell buffer using a dual pipette, as illustrated in Figure 5.4a (A). This filling can be seen as priming the channel since the buffer will evaporate over a few hours, leaving a layer of ionic salts and proteins which allow easy refilling of the channel using the same method, as illustrated in Figure 5.4a (B). A small droplet was then expelled from a capillary tip loaded with cell buffer (pulled to give a diameter ~50 μm) which sat on the PDMS microchannel walls. Using the same capillary, the tip was brought into the PDMS reservoir above the selected cell. Cells were selected as described in Chapter 4. By careful pressurisation and suction of the capillary, the cell could be sucked into the capillary tip. This tip was then brought over the device and placed in the droplet over the microchannel. The cell was expelled into this droplet and, as a consequence of the repellent force of the hydrophobic top surface of PDMS between the channels, was directed into the

microchannel, illustrated in Figure 5.4a (C). By easily removing the excess droplet from the hydrophobic top surface of PDMS between the channels, the myocytes were guided to sediment in the cavity of the microchannel, as shown in Figure 5.4b.
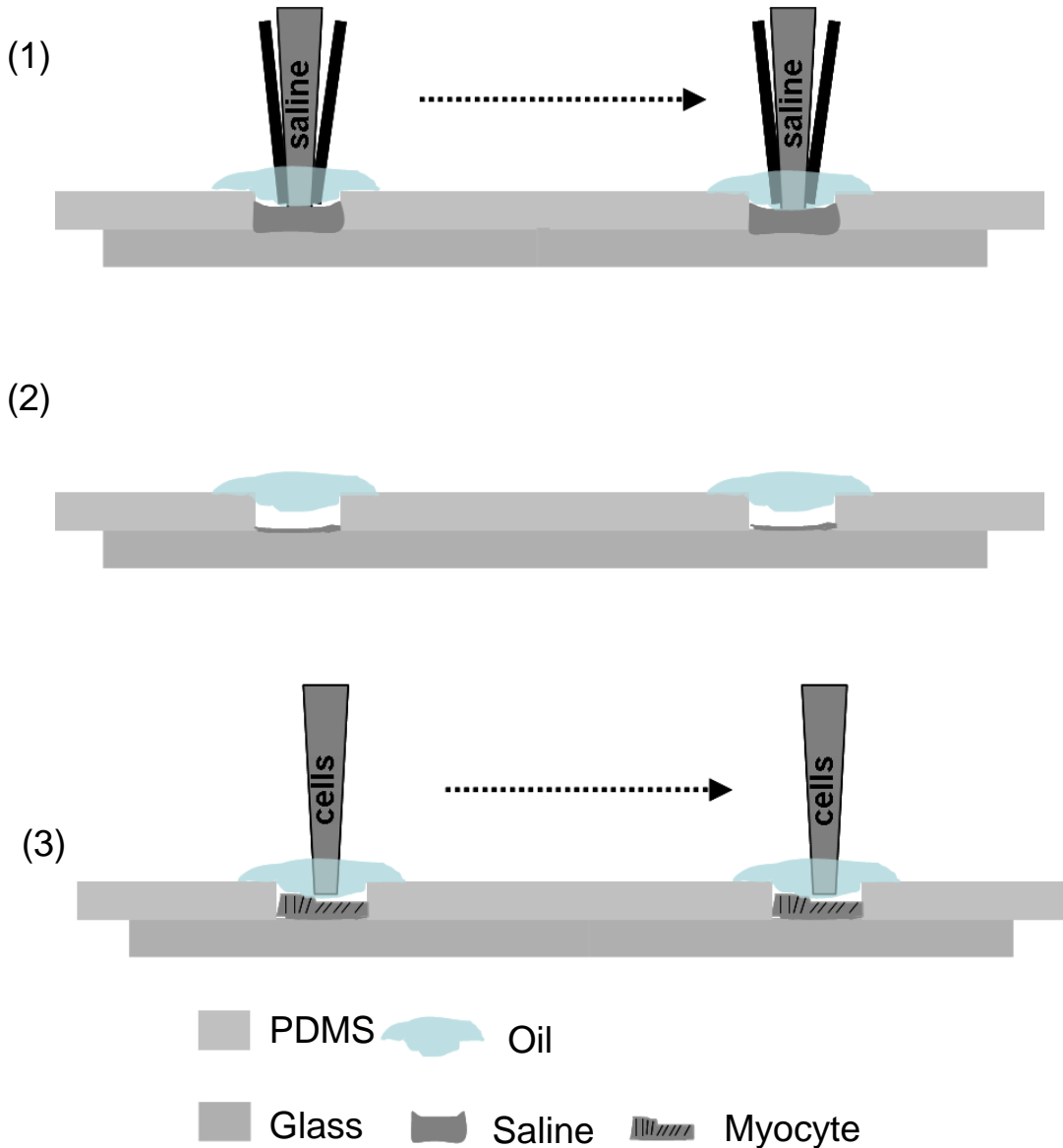
Figure 5.4 Single-cell placement in the PDMS array chamber

(a) Sketch of the single-cell placement procedures: (A) PDMS channel is filled with cell saline using a dual pipette, and covered by a ceiling of mineral oil. (B) Priming the channel with saline leaves a layer of ionic salts and proteins, which allow easy refilling after the buffer evaporates over hours. (C) The cell is expelled from a pipette and settles into the channel as a consequence of the repellent force of the hydrophobic top surface of PDMS and hydrophilic glass surface.
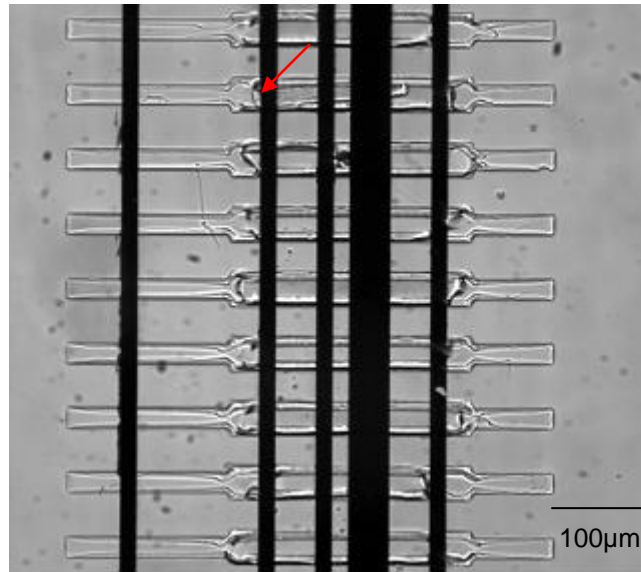
(b) Micrograph of PDMS channel array filled with cells and buffers. A single cardiomyocyte was sedimented into the cavity of the microchannel, as indicated by the arrow.

5.3.4 Electrically Stimulated Contraction of Single Cells

5.3.4.1 Electrolytic Limit to Stimulus Field Strength

After the single cardiomyocytes had settled in the array, as shown in Figure 5.4, rectangular biphasic symmetric pulses were applied between the two stimulatory electrodes to electrically stimulate the cell. Compared to the monophasic pulse, the biphasic symmetric pulse was beneficial due to the charge balancing, to avoid electrolysis and polarization of the electrodes.

As discussed previously (Section 4.4.2), there are several important criteria to enable electrical pacing of ventricular myocytes without side effects, among which the amplitude of the stimulatory pulse is most crucial. The current density within the extracellular space should be sufficient for an action potential but with the voltage amplitude as low as possible to avoid electrolysis of water and cell membrane electropermeabilisation. Further, single cardiomyocytes should be aligned parallel to the electrical field to enable much more effective stimul ation compared to vertical orientation in the electrical field under the same pulse.

In order to account for the possible accumulation of H^+ ions during field stimulation, the pH-sensitive dye BCECF (20 mM) was used to monitor the local pH variation in the

microchannel, which was filled with 240 pL 1 mM HEPES buffer. As shown in Fig. 5.6, the pH did not change using stimulus voltages (1.0 V across two stimulatory electrodes 200 μm apart) close to the theoretical threshold for electrolysis (1.25 V). Although no gassing or signs of pH-dependent dissolution of the Pt were observed during the experiment when pulsed with amplitudes of 2.0 V at 1.0 Hz (100 V/cm), the pH gradually dropped and reached a steady state within 5 minutes of continual pulsing and did not recover after the pulses were stopped. In addition, with a biphasic pulse of 1.0 V, no cell membrane electroporation (indicated by the irreversible leakage of Ca^{2+} into the cell) was detected; 1.0 V was thus selected as the stimulus voltage.
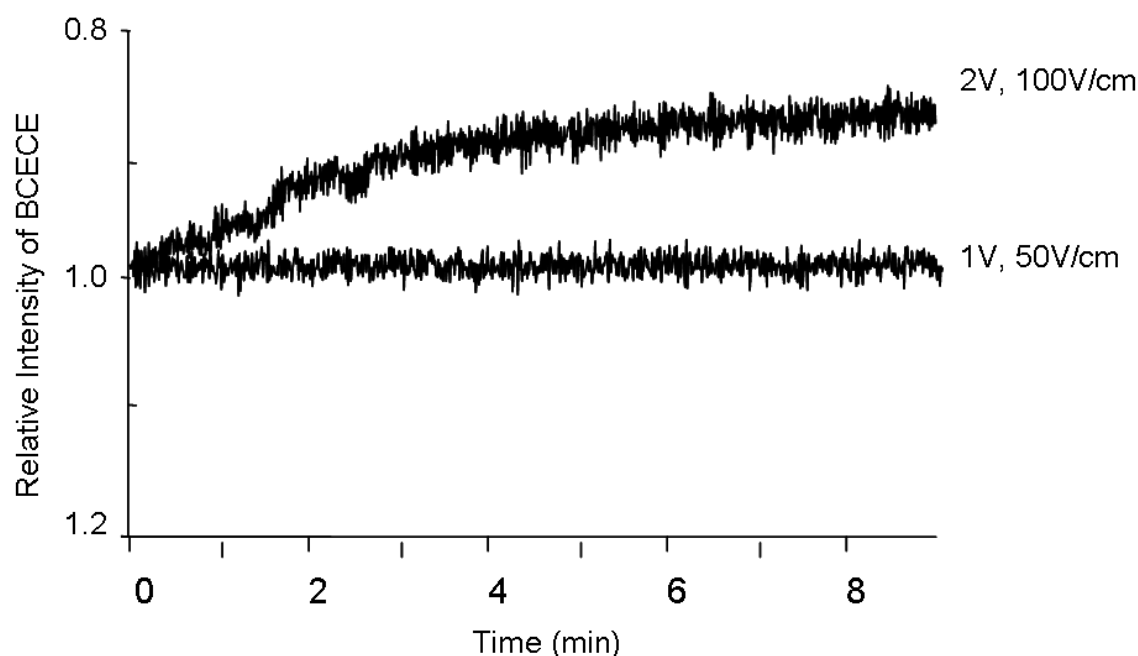
Figure 5.5 Local pH change within 240 pL microchannel buffered with 20 mM HEPES at different field strengths for electrical stimulation of single myocytes. The change in emission of BCECF was related to the initial emission and plotted as the relative intensity against time. The pH was monitored from a region of 4 μm × 4 μm located 2 μm away from the stimulatory anode electrode within the channel.

5.3.4.2 Prolonged Stimulation within a Microchannel

The application of a charge-balanced low-stimulus voltage minimised the acidification of the microchannel, as discussed above. The ability to field-stimulate single adult ventricular myocytes in an unstirred, non-perfused bath would permit usage of a higher number of assay sites e.g. for drug tests. In this Section, the continuous pacing of

myocytes in this array format was investigated at various frequencies ranging from 0.5 Hz to 2.0 Hz. As demonstrated, the microelectrodes and microchannels can both be produced in an array-based format to allow for tests with higher throughputs. Although up to 15 single myocytes can be placed in this microchannel array, sarcomere length was monitored using a 63 C-Apochromat water immersion lens, NA 1.2, which only allows investigation of one single myocyte at a time, as shown in Figure 5.6.

(a)

(b)
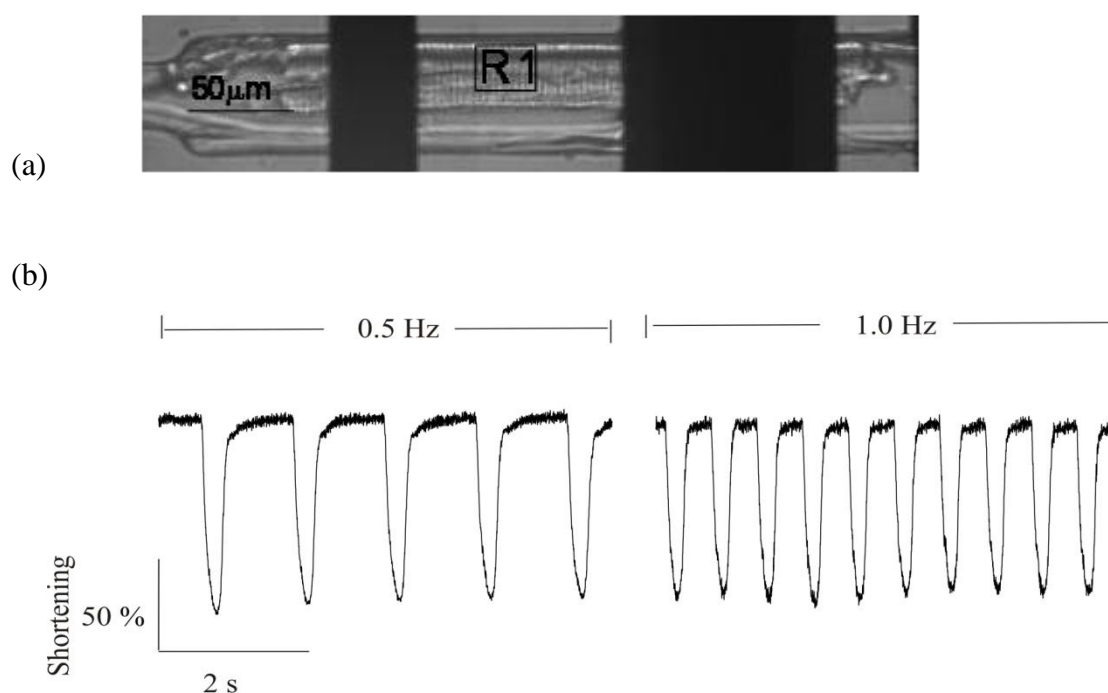
Figure 5.6 shows the contractility of a typical myocyte. (a) Microscopic image of a single cardiomyocyte that has settled down within a PDMS microchamber. The monitored region of sarcomere was selected as indicated by R1; (b) sarcomere length of the myocyte in response to continual pulses at 0.5 and 1.0 Hz.

The effect of continuous stimulation on the amplitude of the cell shortening was investigated. It was found that in this restricted microchannel volume of 240 pL, the amplitude of cell shortening was decreased to a small amount during continual stimulation for up to 20 min, to 30% of the resting amplitude after continual stimulation for up to 40 min, and contractility almost completely decayed within a 60-minute period of continuous stimulation, as shown in Figure 5.7. Big variation exist in different cells (see Table 5.1), for example, in some case, the amplitude of cell shortening only decreased to 70% of the resting amplitude after 40 min (compared to 30% in most cells). These variations might be caused by the variation of capacity in response to acidification

of the extracellular space in different cells. It was also noted that buffer renewal after 60 minutes allowed partial recovery of the contractility, indicative that changes in buffer composition during the continuous contraction had affected cell contractility. Accordingly, the effect of increased extracellular buffer volume on cell contractility was investigated (see 5.3.4.3).
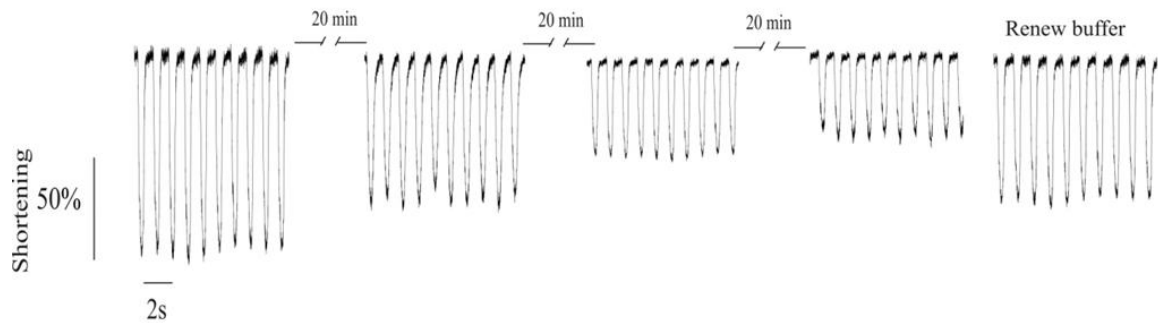
Figure 5.7 The effect of continual pacing on the contractility of single cardiomyocytes. Myocyte contractility was measured as the change of the sarcomere length from cardiomyocytes stimulated at 1 Hz in a 240 pL microchannel at 20 °C. Single transients of 10s duration from a continuous record are shown and monitored at time points 0, 20, 40 and 60 min.

5.3.4.3 Effect of Chamber Volume

As detailed in Section 2.3, using 12, 24, 36 μm thick AZ4562 master moulds, PDMS multi-chambers with various thicknesses can be realised. A 24 μm thick PDMS chamber gives a volume of ca. 2 nL. The effect of continual pacing on the contractility of single cardiomyocytes in these three defined volumes (240 pL, 480 pL, 3nL) was investigated. The average decline in cell shortening under these three conditions is shown in Table 5.1.

		Relative contractility of Cell shortening (%)		
Time point of pacing (min)	Chamber Volume (pL)	240	480	720
0		100	100	100
10		80±7	82±10	85±11
20		72±10	75±9	80±12
30		35±35	38±20	75±13
40		30±30	35±17	62±18
60		20±20	26±19	60±22

Table 5.1 Cell contractility during continuous electrical stimulation (up to 60 minutes) of single cardiomyocytes in a microchamber of three different defined volumes. The number of cells tested for each volume is 5 (N = 5). The change in sarcomere spacing over time was related to the sarcomere length at 0 time point (100%).

It was noted there was a dramatic drop in cell shortening starting after 20~30 minutes of continuous stimulation in the limited extracellular spaces of both 240 pL and 480 pL volume, while stimulation of the myocytes in 720 pL caused a small reduction (to 75%) in shortening amplitude over 30 min. This finding indicates that increasing the thickness of PDMS creates a maximum volume of 720 pL and allows single cardiomyocytes to contract continuously for longer times with gradually decreasing amplitude. As discussed in Chapter 4, the possible reason for this fall in cell contractility is the acidification of the extracellular space. Increasing the buffer to a certain volume might partly neutralise the acidification of the extracellular space and thus increase the duration of cellular excitability. The cause and possible mechanism of acidification of the extracellular space will be investigated in a subsequent section.

5.3.5 Ca²⁺ Flux from Electrically Stimulated Single Cells

5.3.5.1 Threshold for Ca²⁺ Excitation

Applying 1.0 V between the two stimulatory electrodes elicited stable Ca^{2+} transients, as shown in Figures 5.8 and 5.9. The average field strength was comparable to that which enables electrical pacing of myocytes and also well below that of both the electroporation or permeabiliseation (see Section 4.4.2.2) and electrolysis thresholds. Cell electroporation arises when a field strength over 100 V/cm is applied, was indicated by the irreversible leakage of $[Ca^{2+}]_i$. The electrolysis threshold is below 1 V, as shown in Figure 5.5.

(a)	(b)

Figure 5.8 Single myocytes loaded with Fluo-3 (by incubation for 30 minutes in 20 mM Fluo-3 AM) were placed within a microchannel and stimulated by applying unipolar pulses of 1.0 V at 0.5 Hz using the two stimulatory electrodes. (a) Single frames from the fluorescence video recording of intracellular $[Ca^{2+}]$ from a single resting myocyte. (b) Fluorescence image of the point showing the maximal global increase of the $[Ca^{2+}]_i$ upon excitation-contraction.
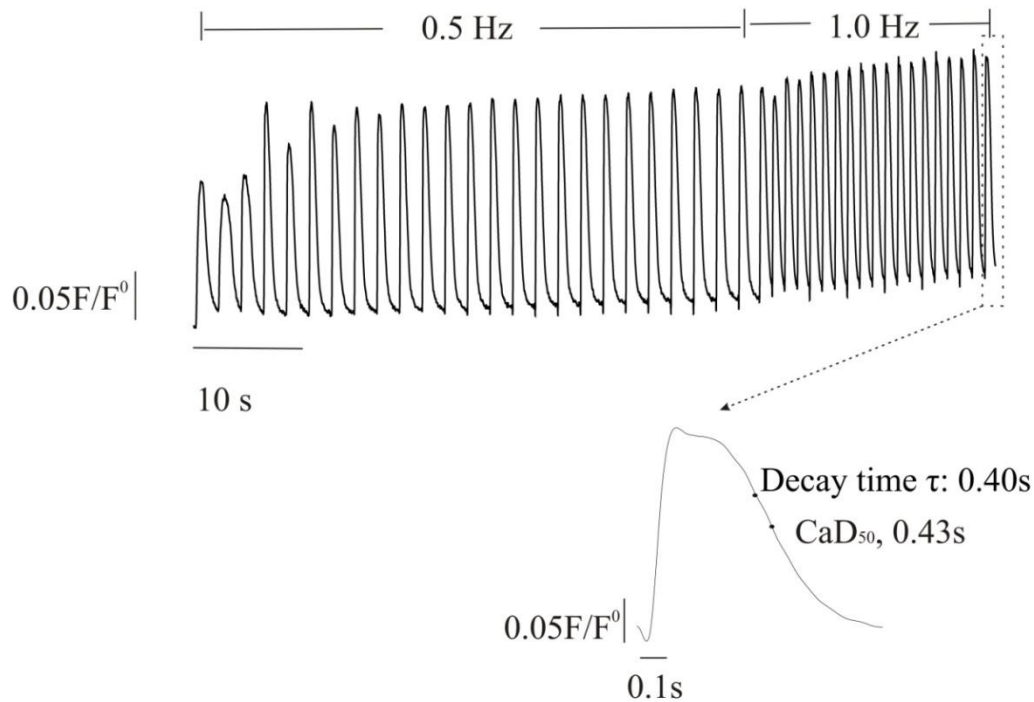
Figure 5.9 Typical [Ca^{2+}]i transients during electrical stimulation. Single Fluo-3-loaded cardiomyocytes were electrically stimulated in the restricted extracellular space of the microchannel (100 pL) by applying 1.0 V at alternating frequencies of 0.5 Hz and 1.0 Hz. Inset: A single Ca^{2+} transient at steady state at 1.0 Hz: the decay time τ is estimated as 0.40s, and CaD$_{50}$ 0.43s; the transient of the recovery period could be fitted with a monoexponential function: $Y = 0.25F/F_0 + 0.25F/F_0e^{-t/0.4}$

Intracellular Ca^{2+} fluxes are implicated in excitation-contraction coupling. The peak of the fluorescence transient (systolic Ca^{2+}) reached steady state immediately. The diastolic Fluo-3 fluorescence signal adapted instantaneously to slightly higher levels of what at higher frequencies, as shown in Figure 5.9. To characterise the Ca^{2+} transient during stimulation, the following parameters were used: the duration of CaD$_{50}$ (the time from the start of the transient to the point of 50% recovery), the decay time (τ) was taken as the time from the peak to the point of 36.79% recovery.

The transients in the recovery period could be fitted with a monoexponential function shown in Equation 5.2, expressing a relationship between the amplitude of the Ca^{2+} transient and time. (Y_0 is the minimal amplitude, defined as the amplitude of diastolic levels of Ca^{2+}, τ is the decay time, A is defined as $Y_{max} - Y_0$)

$$Y = Y_0 + Ae^{-t/\tau} \hspace{3cm} \text{Equation 5.2}$$

5.3.5.2 Ca²⁺ Fluxes during Continuous Contraction

Single Fluo-3-loaded cardiomyocytes were stimulated to contract continuously by applying 1.0 V between the two stimulatory electrodes within a microchannel, under which conditions stable Ca^{2+} transients were elicited.

The amplitude of the Fluo-3 fluorescence signal decreased slowly over 20 minutes of stimulation, as shown in Figure 5.10. This decrease may represent a fall in the intracellular levels of Ca^{2+}. To account for the decrease in the fluorescence signal caused by dye bleaching or dye loss, a control experiment was carried out involving monitoring of the intracellular Ca^{2+} fluorescence signal for the same period of time but without stimulation. The control experiment indicated that although there was a decrease of dye background signal, the amplitude of decrease was much less than the attenuation of fluorescence signal caused by the decrease of intracellular Ca^{2+}.
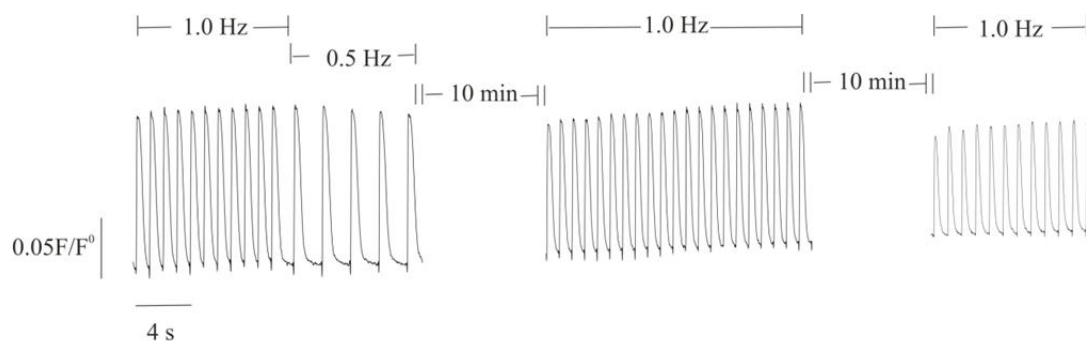
Figure 5.10 Ca^{2+} fluxes from single cardiomyocytes within a microchannel during continuous contraction. Single Fluo-3-loaded cardiomyocytes were stimulated to contract continuously within a microchannel. The amplitude of the Fluo-3 fluorescence signal was monitored over 20 minutes of stimulation.

	Ca^{2+} transient of 3 cells (Mean±SEM)		
Stimulation period (min)	Transient peak (%)	CaD$_{50}$(s)	Decay (s)
0	100	0.44±0.04	0.40±0.04
10	80±10	0.36±0.04	0.32±0.04
20	75±15	0.32±0.08	0.28±0.08
25	25±25	0.20±0.08	0.16±0.08
Buffer renewal	60±10	0.24±0.08	0.20±0.08

Table 5.2 Attenuation of the Ca^{2+} transients (from continually stimulated single cardiomyocytes in a microchannel of defined volume as 480 pL)

We also found that the attenuation of intracellular Ca^{2+} was similar to the decrease of cell shortening (both nearly eased after 20 minutes of continuous pacing). The falls in both intracellular Ca^{2+} and shortening could be caused by the acidification of the extracellular space (as discussed in Chapter 4), although some studies have argued that intracellular acidification causes decreased shortening but increased Ca^{2+} transient amplitude [142].

Single Fluo-3-loaded cardiomyocytes were paced at 1.0 Hz and the electrically evoked Ca^{2+} transients were continually recorded for off-line evaluation. Peak systolic Ca^{2+} was normalized to the maximum amplitude at steady state. The CaD$_{50}$ is taken as the duration from the start of the transient to the point of 50% recovery. Decay is taken as the time from the peak to the point of 36.79% recovery.

5.3.6   Intracellular pH within Electrically Stimulated Single Cells

As discussed previously, we investigate the metabolism of single paced cardiomyocytes which were electrically stimulated over a long period of time. It was noted that there was a fall in both Ca^{2+} and cell shortening after a certain period. One possible explanation is that the falling contractility was due to the increase of external concentration of H^+ within

the restricted extracellular space, which may inhibit cell metabolism. We have shown that there is a decrease in extracellular pH during continuous cell contraction (Section 4.4.4.2). Here, the intracellular pH is monitored in real time during continuous cell contraction using single wavelength fluorescence of AM-BCECF. As with other fluorophores, the amount of dye loaded into cells is crucial because excessive dye concentrations can result in the self-quenching of fluorescence. An optimised average amount of 0.02mg L^{-1} AM-BCECF was loaded in the cell culture and incubated for over half an hour.
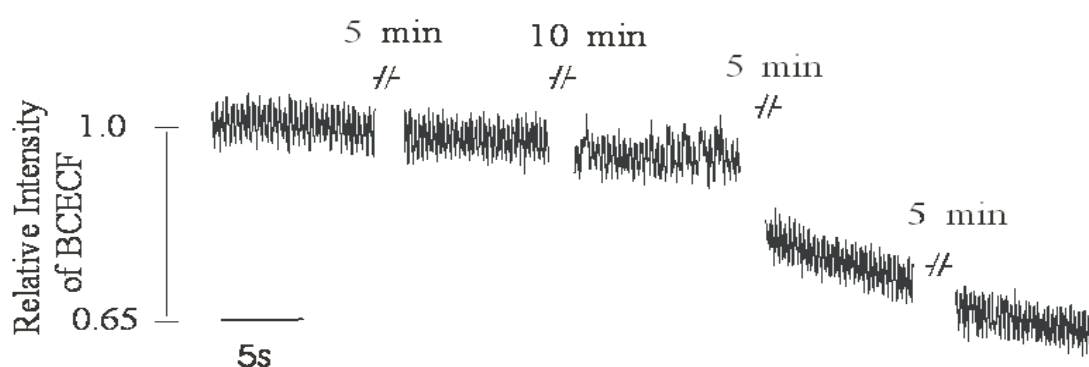
Figure 5.11 Intracellular pH of single cardiomyocytes in a microchannel during continuous stimulation. Single AM-BCECF-loaded cardiomyocytes were stimulated continuously within a microchannel. The amplitude of the BCECF fluorescence signal was monitored over 20 minutes of stimulation.

Table 5.3 Intracellular pH measurement of single AM-BCECF-loaded cardiomyocytes during continuous stimulation:

Time point of pacing (min)	Cell No.	Relative Fluorescence Intensity of AM-BCECF		
		1	2	3
0		1.0	1.0	1.0
5		0.99	1.0	1.0
15		0.96	0.97	0.95
20		0.75	0.72	0.70
25		0.68	0.69	0.67

Intracellular pH was monitored as relative fluorescence of AM-BCECF during continuous stimulation (up to 25 min). It was noted that there was a dramatic break point with respect

142

to the intracellular pH decrease after ca. 20 minutes of continuous stimulation (Figure 5.11).

Five individual cells were monitored by loading them into separate channels on a single device. Interestingly, there was a break point with respect to intracellular pH after ca. 20 min, at which the pH fell significantly compared to the previous period, as shown in Table 5.3. During control experiments (with loaded cells but without electrical field stimulation) there was no such intense change, although a slightly decreased signal was seen due to bleaching of BCECF fluorescence and/or the diffusion of fluorescent dye to the extracellular space. Therefore, this dramatic fall in intracellular pH is caused due to cell stimulation. The dramatic decrease of intracellular pH could occur because during continuous cell contraction, there is a dramatically increased proton concentration within the intracellular space as a by-product of anaerobic glycolysis, and cell metabolism could be inhibited by the resultant decreased intracellular pH. The cell was able to restore the intracellular pH using alternative pH regulatory mechanisms. It has been shown that there would be an efflux of protons from the intracellular to the extracellular space, which would contribute to the acidification of the extracellular space (see Chapter 4).

However, it was also noted that in most cases, the cell was no longer able to contract or contracted irregularly in response to the continuous electrical field stimulation before this dramatic decrease in intracellular pH had occurred. Therefore, it is possible that the cell membrane was partly electropermeabilised due to the long exposure to the electrical field. The BCECF fluorescent dye could also have diffused into the extracellular space through this electropermeabilised membrane at some point, which would then contribute to this dramatic drop in the signal.

It is known that when a cell is undergoing very intense exercise (which could be referred to as anaerobic metabolism), there is an increased accumulation of lactate from this anaerobic glycolysis [143]. Lactic acid would be transported out of the cell at some point to restore the intracellular pH [144]. Therefore, the questions here would be whether there is any relation between this dramatic drop in pH and the lactate accumulation, and whether the accumulation of intracellular lactate accordingly causes the dramatic drop in intracellular pH.

5.3.7 Lactate from the Electrically Stimulated Single Cell

Lactate is measured from single cardiomyocytes during continuous cell contraction (particularly after this dramatic drop in intracellular pH) to investigate whether there is lactate accumulation in the intracellular space during continuous cell contraction, and to explore whether there is any relation between lactate accumulation and the dramatic drop in intracellular pH.

Single AM-BCECF-loaded cardiomyocytes were stimulated continuously within a microchannel. Lactate was monitored in real time during this period using a three-electrode system integrated within the microchannel, which involves an LOD enzyme-modified microelectrode, an Ag|AgCl quasi-micro reference and a counter microelectrode.

However, unlike the metabolically inhibited cells (Chapter 4), no measurable current signal was seen in the period during which the cell was electropermeabilised after a dramatic fall in intracellular pH was observed, indicative that the significant intracellular pH decrease might not be directly attributable to the intracellular lactate accumulation.

The result also indicated that no simultaneous electrochemical signal arose during continuous cell contraction, although there was a slightly raised background of electrochemical signal, to which a partial contribution might be made by lactate released from the cell during contraction. It is possible that during continuous cell contraction, the cell membrane was compromised during electrical stimulation prior to any further anaerobic glycolysis; thus, any lactate produced during the anaerobic glycolysis would have been released through this partly permeabilised membrane into the extracellular space. However, the amount of lactate released was too small to be measured in real time by our system although, as before, it could be measured if the signal was integrated over an extended period of time, and measured as Q. It would be possible in the future further to investigate whether there is a relationship between the production of lactate and the "work" that the cell is doing (as measured by the rate of contraction).

5.4 Conclusion

A new platform based on an array of poly(dimethylsiloxane) (PDMS) microchannels integrated with a microelectrode array has been presented. The advantages of this device were demonstrated in single-cell manipulation within microfluidic channels, with the potential of the parallel handling and analysis of single cells. In addition, this device has improved efficiency over the single SU8 chamber device, as the regeneration of fouled electrodes is not required. The microelectrode array was electrochemically characterised and LOD was immobilised. In this array device, Ca^{2+} flux from electrically stimulated single cells and intracellular pH was monitored in real time during continuous contraction for a long period of time. The amplitude of intracellular Ca^{2+} flux was decreased over time and the flux nearly eased after 20 minutes of continuous contraction. Intracellular pH decreased gradually until a dramatic break-down point was seen. Lactate was then monitored in real time during the course of intracellular acidosis to explore the relation between lactate efflux and acidosis. The initial results indicated that the significant intracellular pH decrease might not be directly attributable to the intracellular lactate accumulation. Although sufficient information about released lactate during the course of acidosis has not yet been obtained, the array system has shown the potential to enable simultaneous electrical and optical monitoring of extra- and intracellular metabolites from single beating heart cells.

Chapter 6 Future Work and Conclusion: Microfluidic Integrated Systems for Single-Cell Analysis

6.1 Introduction

Microfluidic and micromachined devices make it possible to manipulate single cells, so their analysis under controlled yet physiologically relevant environments can be created. By parallelization of these applied methods, large numbers of single cells can be observed simultaneously, and in future metabolomics and proteomics of single cells can be analysed in parallel simultaneously, which will boost basic biological research, clinical medicine and drug discovery research [145].

This Chapter complements the previous descriptions of the fabrication of a simple, integrated microfluidic system by describing how the new materials and methods can yield simple, cost-effective routes for real-time analysis of a single heart cell. Finally, a microelectrode array system with a view of developing high-throughput analysis of single cells is proposed.

6.2   Chemicals and Materials

SU-8 10 and SU-8 2050 was obtained from Microchem Corp (Newton, MA, USA). SU-8 developer (Micro deposit EC-solvent: propylene glycol monomethyl ether acetate) was from Shipley Europe Limited (Coventry, UK). Isopropyl alcohol and glass slides were obtained from BDH Laboratory Supplies (Poole, England). Poly(dimethylsiloxane) (PDMS) was obtained from Dow Corning (Northants, UK).

6.3   Methods

The fabrication of a microfluidic system in PDMS was realised using two methods. The advantages and disadvantages of both methods will be discussed as follows.

6.3.1   Fabrication from SU-8 Mould

Fabrication of PDMS microfluidic channels from an SU-8 mould is illustrated in Figure 6.1, briefly described as the following process:
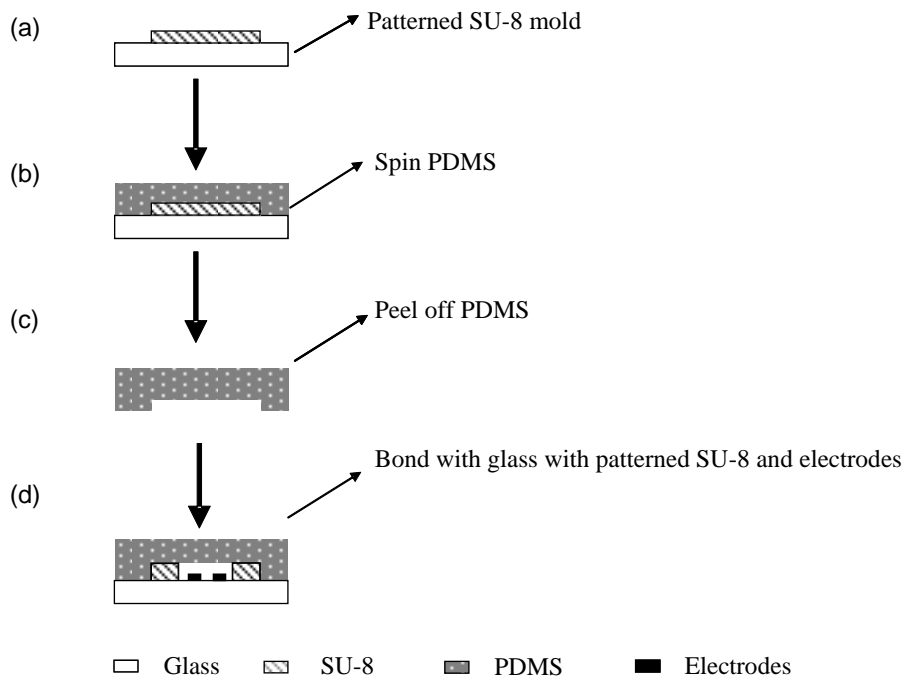
Figure 6.1 Schematic diagram describing the fabrication of an enclosed PDMS microfluidic channel from an SU-8 mould: (a) An SU-8 mould structure was patterned and modified to produce a hydrophobic surface; (b) A prepolymer of PDMS was cast onto the mould and cured at 70°C for 1 hour; (c) The PDMS replica containing a negative relief of the channels was peeled away from the mould; (d) The PDMS replica and glass substrate containing SU-8 and microelectrode patterns were treated in oxygen plasma for 1 minute and immediately brought into close contact for bonding.

6.3.1.1 Fabrication of SU-8 Mould

Different thicknesses of SU-8 mould structures were fabricated (depending on the desired thickness of the PDMS channel) using standard photolithographic methods, by adjusting spin speed and time, pre-baking time, exposure time, post-baking time and developing time of the mould. Following fabrication of the SU-8 mould structures, the mould was modified by CF_4 plasma to produce a hydrophobic surface for easy removal of PDMS (Figure 6.1a).

147

6.3.1.2 PDMS Replica Moulding

The two components of PDMS prepolymer were thoroughly mixed using a volume ratio 10:1 (10ml base to 1ml curing agent). Trapped air bubbles were allowed to disappear from the catalysed materials for ca. 10 min. Following that, PDMS was cast onto the master either by drop-coating or by spinning. The former produced a thicker film, whereas the later produced a PDMS film of ca. 0.7 µm thick. The sample was cured at 70°C in an oven for 60 min. After curing, the PDMS containing the inlaid pattern was peeled from the mould (Figure 6.1b, c).

6.3.1.3 Oxidation and Bonding

The glass slide substrate (with patterned microelectrodes and SU-8 chambers) was rinsed in ethanol and water, blown dry in nitrogen and placed in an oven at 200 °C. The glass substrate and fresh PDMS replica were placed in oxygen plasma cleaner (ET plasmofab 505 Barrel Asher, Electrontech) for 60 sec (2 L/min oxygen, 5 psi nitrogen, 30 mT base pressure, 70 W RF power). The two substrates were contacted by conformal press to produce an irreversible bond immediately following plasma treatment (Figure 6.1d).

6.3.2   Fabrication from AZ Resist

Figure 6.2 shows schematic the general fabrication process for defining the enclosed microfluidic structures, which is different from traditional mould fabrication.

After the glass substrate had been patterned by microelectrodes within an SU-8 microchamber (see section 2.3.4.1), a layer of positive photoresist (AZ4562) was spin-coated and UV-patterned on the top of the SU-8 layer. Following that, the device was covered with a slab composed of a thin film of silicone sealant either by drop-coating or by spinning, in both cases using a 5% v/v solution of N-heptane as a carrier solvent. The PDMS was allowed to cure for 60 minutes at 70 °C in an oven. PDMS layers can be obtained from hundreds of micrometres up to several millimetres thick. After curing, the inlet and outlet interconnect ports were exposed by cutting away an area of silicone

rubber. AZ resist inside the channels was eluted by simple immersion of the device in acetone for ca. 60 minutes.

Due to the robust, truly elastomeric nature of the silicone adhesive seal, the surface of the rubber can be manually pressed or temporarily deformed to speed up resist elution without compromising the channel shape or the integrity of the seal to the substrate. Glass micro-bore capillary tubes as fluidic connectors were inserted into the channel entrances and secured using Loctite 350 UV-curable glue to form a fluidic outlet.

(a)   Pattern AZ resist

(b)   Spin PDMS

(c)   Elute AZ resist with acetone after curing silicone rubber

☐ Glass   ▨ AZ4562   ▨ PDMS
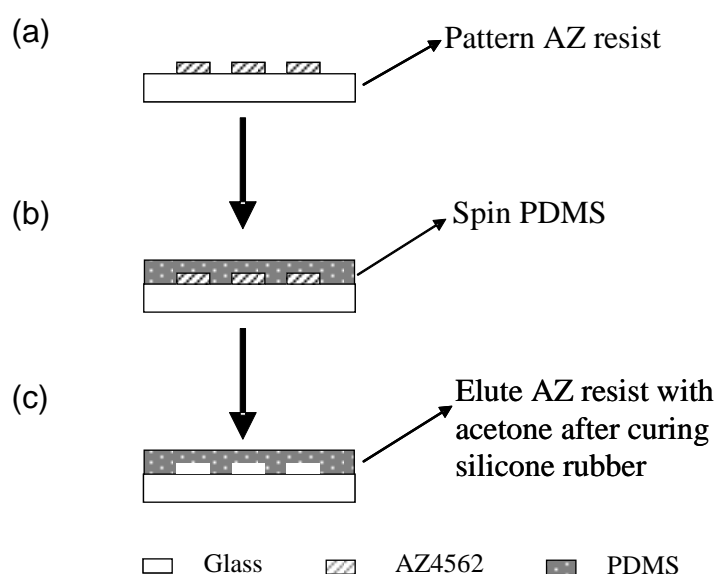
Figure 6.2 Schematic outline of the procedure of fabrication of enclosed PDMS microchannels from AZ resis: (a) AZ resist was photolithographically patterned on a glass substrate (containing previous patterns); (b) A thin prepolymer of PDMS was spin on and cured at 70°C for 1 hour; (c) AZ resist inside the channels was eluted by immersion in acetone for 1 hour to produce the enclosed sealed PDMS microfluidic channels.

6.4   Results and Discussion

6.4.1 Integrated Microfluidic Channels

An enclosed microfluidic structure was integrated into the design, involving a five-electrode system integrated within a microchamber. The microfluidic channel was 40 μm in width (wide enough to enable the single myocyte to flow through), and had an inlet and outlet port as the reservoir for the cell suspension and waste, as shown in Figure 6.3. The

purpose of this design is to produce a three-layer integrated device for automated analysis and sequential operations of single cells using microfluidics to trap the cell. Further, the advantage of this design is associated with the simple fabrication process for multi-layer structures without dry etching or wet etching, as detailed previously.
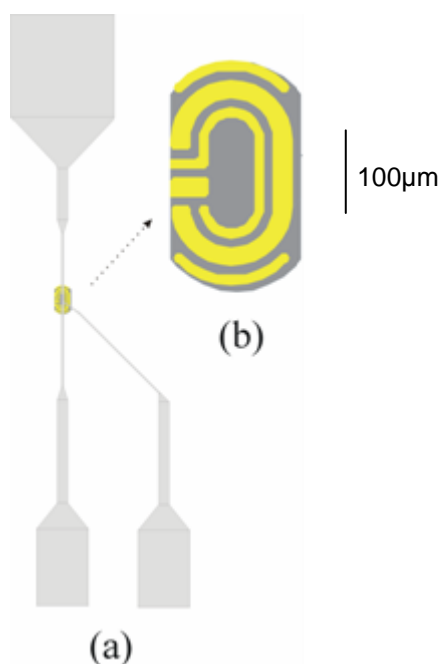
Figure 6.3 Diagram of design for the integrated microfluidic channels: (a) Layout of microfluidic channels integrated with electrochemical device (scale 6:1); (b) magnification of the electrochemical device (scale 60:1).

6.4.2   Fabricating PDMS Channels

Two different methods were introduced to fabricate the PDMS microfluidic channels, one of which involves taking PDMS replicas from an SU-8 master. To improve the PDMS/substrate seal, the PDMS interface can be exposed to oxygen plasma followed by rapidly placing the activated surface on the substrate [146, 147]. However, this method forms a "once-only" seal so accurate alignment between features in the PDMS layer and the glass substrate was a problem. Alternatively, PDMS can be irreversibly sealed on the substrate simply by pressing [148]. However, if the substrate is not smooth – for example, containing other structures such as patterned metal electrodes or a microchamber – this

will reduce the durability of the seal over the whole structure. In this condition, the seal can become problematic and can only withstand a low pressure [149].

To seal the PDMS and the patterned SU-8, a small area of SU-8 patterned on the glass substrate was designed in order to expose a large area of glass outside of the SU-8 pattern so that it is possible to achieve a spontaneous irreversible bond between the exposed outside glass area and the PDMS. This method improved the bonding between SU-8 and PDMS; however, accurate alignment between features in the PDMS layer and the glass substrate was still a problem.

To circumvent this alignment problem, in contrast to traditional methods, an alternative method to fabricate PDMS channels was developed. An enclosed channel structure was created by lithographically defining the pattern of the microfluidic structure on a substrate using a photopatternable soluble AZ thick-film resist. The method provides an alternative to the use of plasma-treated PDMS, and has the advantage, particularly in the present study, that the substrate has shaped fabricated structures that form part of an overall multi-layer microfluidic chip.

It is likely that the elution of AZ resist from the silicone rubber-covered channels was due to the ability of acetone to permeate through the silicone rubber layer (solvent access to the AZ resist was not restricted to the micrometre-sized openings at the entrance to the channels). However, it was found that such solvent permeation does not weaken the silicone-glass seal only when the PDMS adhesive layer is as thin as less than ca. 300 μm, although thicknesses of PDMS can be obtained up to several millimetres by drop-coating. PDMS of high thickness may limit solvent permeation to the resist and thus may cause the silicone partly to swell in acetone after long immersion. Therefore, a thin adhesive layer of PDMS (ca. 100 μm-thickness by spin-coating at 2000 rpm for 30 sec) was used to form enclosed channels.

Figure 6.4 shows microscope images of a microfluidic channel network fabricated using the second method (Figure 6.4a, b), including the finalised multi-layer microfluidic device (Figure 6.4c) to be used for the study of single cardiomyocytes. Fig. 6.4 b corresponds to the device of the upper panel after AZ resist removal and shows that clear channels are formed.

151

(a)

(b)

(c)
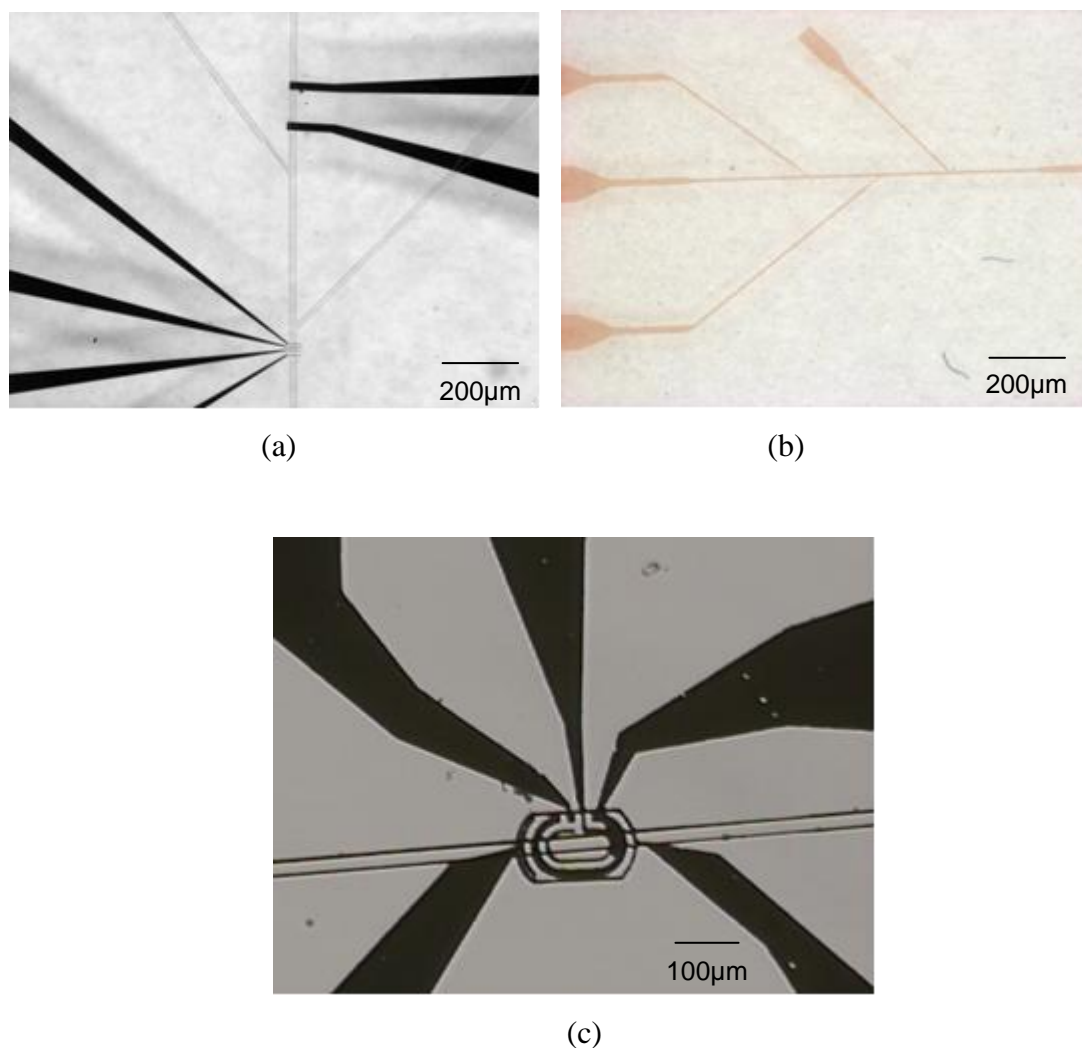
Figure 6.4 Microscope images of different structures of microfluidic channels using the methods described above: (a) Microfluidic PDMS-enclosed channel; (b) PDMS channels after AZ resist removal; (c) Finalised multi-layer microfluidic device with integrated PDMS channel.

6.4.3 Integrated Microfluidic System for Real-time Monitoring of Single Myocytes

On the basis of the techniques described in this work, an integrated microfluidic biosensor chip is proposed, as shown in Figure 6.5. The device includes a common Pt counter electrode (CE), one quasi-reference electrode (Ag|AgCl) and one Pt working electrode, and two stimulatory electrodes, as described previously. Two layers of SU-8 could be used, one of which is a thin layer as insulator (~2 μm) for the electrode pattern and the other a thick SU-8 layer (~50 μm) as a flow chamber.

Before being enclosed by PDMS channels, the immobilization of various enzymes on the microelectrode was developed using the methods described previously. The PDMS channels containing an inlet and outlet of buffer were enclosed within an SU-8 chamber (Figure 6.5 a, b). The dimensions of the microfluidic channel and flow chamber allow them to be used to form an analytical chamber where single myocytes can be located (total internal nano volume of < 2 nl). A syringe pump was used to deliver cell culture buffer from inlet to outlet at a slow rate (~µl/min) so that single myocytes can flow through with the buffer separately and pass into the chamber individually (diluted cell buffer ($<10^4$ /ml) is also required). Due to there being little flow, the cell then can slowly "sit down" and eventually be immobilised within the microchamber (300 µm wide, 20 µm deep) by its sedimentation and by discontinuing the flow pressure.
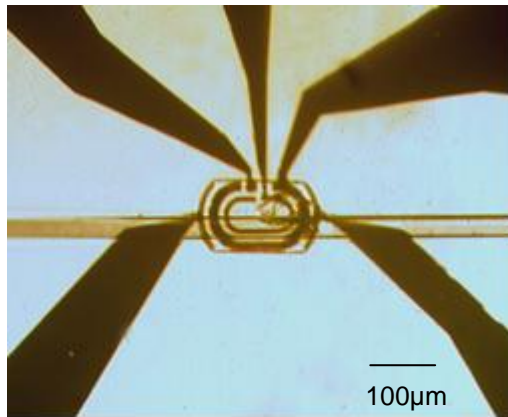
(a)
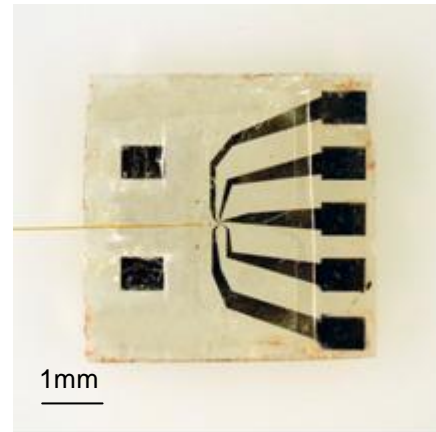
(b)
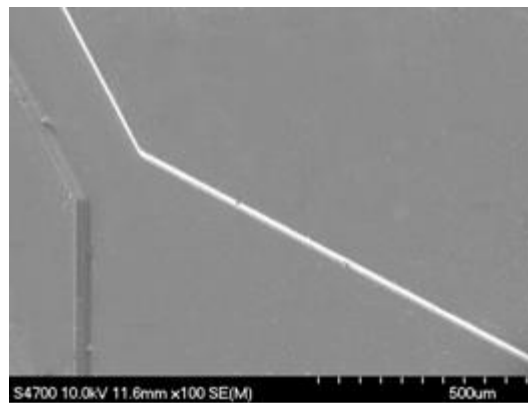
(c)

Figure 6.5 Microscopic image (a) and original photograph (b) of an integrated microfluidic system chip: This microfluidic chip includes biosensors (comprising five microelectrodes) integrated within an SU-8 analytical microchamber enclosed by PDMS to form a microfluidic chip, through which single myocytes can flow and be immobilised within the microchamber; (c) SEM image of PDMS microfluidic channel with inlet opening. The channel has the dimensions 100 μm width and 20 μm height.

6.4.4 Individually Addressable Microelectrode Array Towards High-throughput Analysis

Work was performed toward developing a planar microelectrode array for real-time monitoring of individual cells in parallel. An array of sensor elements patterned into a substrate is proposed, connected to a system of microchannels through which mixtures of analytes and individual cells can be delivered. This potential microfluidic network allowed the transport of single cells and their manipulation at desirable locations where

intracellular or extracellular analytes (for example, the metabolites released from a single heart cell) are electrochemically measured in real time using individually addressable microelectrode arrays. The system would afford the additional benefits of high-throughput screening of single cells using both electrochemical and optical methods.

In the first aspect of work, the chip consists of an array of SU-8 microchambers, as illustrated in Figure 6.6, with each chamber containing a working electrode, a counter electrode, a reference electrode and possibly two stimulatory electrodes. Microfluidic channels built upon the SU-8 chambers form the enclosed microfluidic network (which is similar to previous work), enabling single cells to be transported through a flow-through system.

<table>
<tr><td>(a)</td><td>(b)</td></tr>
</table>
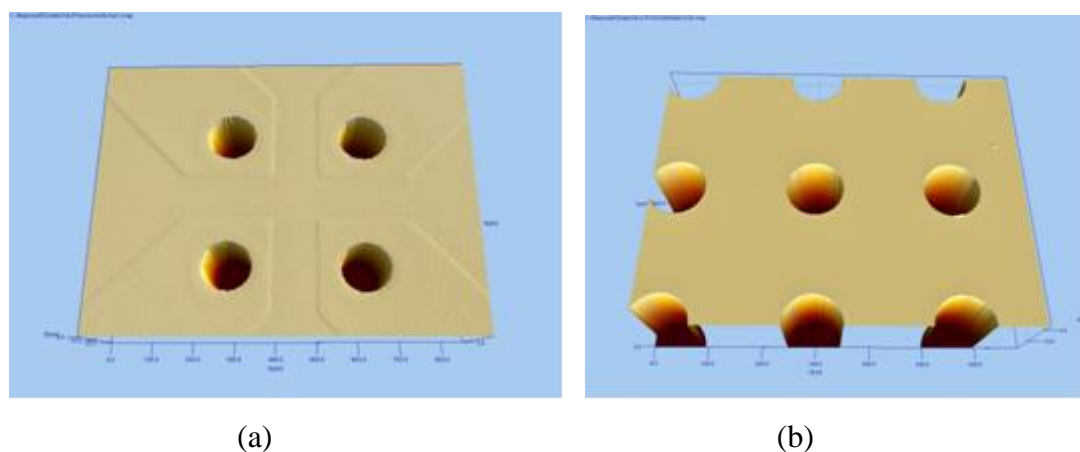
Figure 6.6 The proposed chip for high-throughput screening of single cells: (a), (b) Images of surface profilometry on 2x2 and 3x3 array microwell SU-8 apertures (20μm depth), which was integrated with an electrochemical biosensor system involving a working electrode, a counter electrode, a reference electrode, and possibly two stimulatory electrodes.

In the second aspect of work, the chip design has borrowed the advantages of open chamber architecture specifically for an array of myocytes (an average-sized ventricular myocyte has dimensions of 160 μm in length, 25 μm in width), as illustrated in Figure 6.7. This design enabled single myocytes to be placed much less elaborately between two stimulating electrodes within the chamber, which process is again contributed to by the hydrophobic character of the PDMS chamber on a hydrophilic glass substrate. In addition, this arrangement involves four individually addressable microelectrodes (apart from a common pseudo-reference electrode crossing each chamber) to permit the sequential

stimulation of individual cells with different field strengths and/or frequencies of stimulation, as well as both electrochemical and optical measurement of individual cells under different experimental conditions, where the metabolic state of each cell can be individually controlled.

200 µm
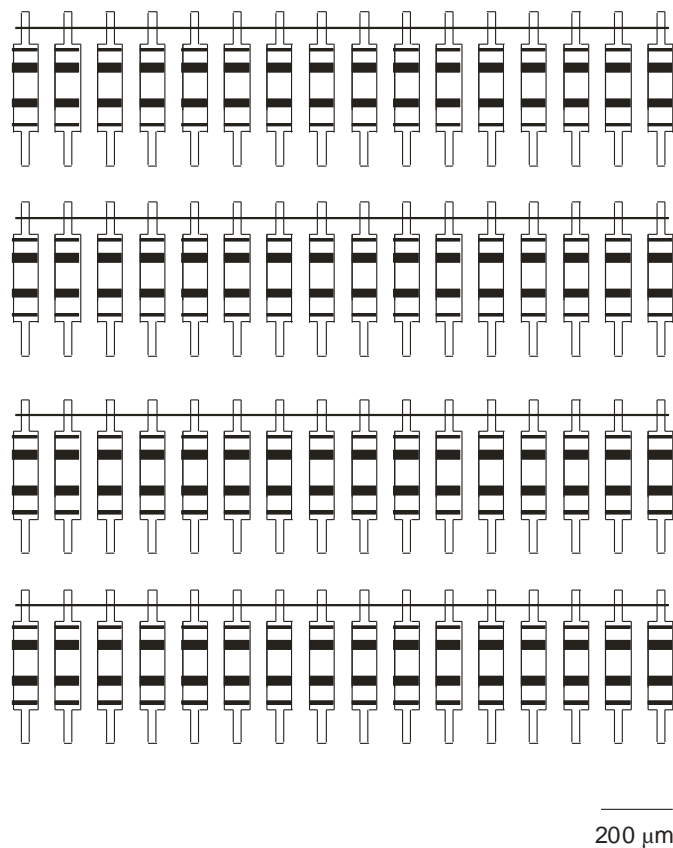
Figure 6.7 A proposed chip for high-throughput screening of single myocytes. The schematic integrated biosensor chip shows (from top) a common pseudo-reference electrode crossing each chamber, two stimulatory electrodes, a working electrode, and a counter electrode. Up to 64 single myocytes can in principal be placed between two stimulating electrodes within each chamber.

156

6.5 General Conclusion

This research has been concerned with microfabricated devices which enable electrochemical and optical real-time monitoring of metabolites from single, stimulated, beating heart cells. The general conclusion from this study is summarised below.

Two general designs for the metabolic study of single beating cardiomyocytes have been developed. One involved microelectrodes, fully integrated within a single microfluidic SU-8 chamber. The other had a sensor array integrated within a poly(dimethylsiloxane) (PDMS) microchannel array. Each device had a five-electrode system, which comprises one pair of pacing microelectrodes used for the field-stimulation of the cell, and the other three microelectrodes configured as an electrochemical biosensor, containing a working electrode, a counter electrode, and an internal Ag|AgCl microreference electrode. The devices were fabricated using photolithography to give a high aspect ratio SU-8 well and PDMS chamber array. A thin layer of photoresist was used in fabricating the SU-8 chamber (having a depth of 20-25µm) as a sacrificial layer over the microelectrode to protect the electrodes from fouling by SU-8 residues. AZ photoresist films of varying thickness were patterned as master structures to form PDMS microfluidic chambers with different thicknesses (ranging from 12µm to 36µm). Both devices were evaluated to give reproducible fabrication, and excellent analytical results.

The device was then electrochemically characterised using FMCA to reveal the cyclic voltammetric responses to FMCA at various scan rates from the integrated sensors, and the response to different concentrations of FMCA. The internal Ag|AgCl reference was evaluated by using FMCA as a calibrating redox couple, and by comparing the actual potential of the internal micro-pseudo reference Ag|AgCl *vs.* a true Ag|AgCl electrode, and showed a stable potential within 15 hours. Microvolume and pL-scale lactate measurements using the micromachined integrated sensor were carried out, with a real detection limit of 18 µM and 7.6 µM lactate respectively. The response of the sensor to microvolumes of lactate at different applied potentials was investigated, giving a plot of peak current against potential. An immobilised microfabricated enzyme-modified sensor was achieved using an electrochemically polymerised film to entrap lactate oxidase enzyme onto the working electrode. The enzyme-immobilised lactate sensor was electrochemically characterised using a microinjection system to dispense volumes as low

as 1 pL, producing a linear calibration curve for the charge transferred *vs.* the amount of the injected lactate in the range of 4.8 to 66 fmol, with a detection limit equivalent to 7.4 μM. The fundamental kinetics of the sensor were investigated. This LOD enzyme-immobilised lactate sensor was found to be stable for at least four days. The quick response and high sensitivity of the LOD enzyme-immobilised lactate sensor provided a generic method to make a wide range of single-cell sensors in pL-scale volumes based on oxidase-reductase enzyme.

The study of ionic and metabolic fluxes from active, beating single heart cells on the microfabricated device was presented. Single myocytes were manipulated within the SU-8 microchamber to be paced at the optimised field stimulation (75 V/cm) without local pH change. Cell contraction was simultaneously recorded as the change of the sarcomere length upon electrical stimulation within the microfluidic structure. The change of intracellular [Ca^{2+}] from single Fluo-3-loaded cells upon stimulatory pulses of low frequency was optically monitored in response to cell shortening, indicating normal excitation-contraction coupling (EC coupling). In a model of anoxia, the amplitude of cell shortening decreased to ca. 20% of the maximum after 20 minutes of continuous stimulation. Accordingly, the relative extracellular pH was optically monitored in real time as a function of the amplitude of cell shortening, with a 2% and 5% decrease after respectively 10 and 20 minutes of continuous pacing, indicating that the decrease in the contractility of the cell could be associated with the fall in extracellular pH.

The integrated microelectrodes were configured as an enzyme-linked lactate microbiosensor, and were used to measure the amounts of lactate produced by the heart cell. The efflux of lactate into the extracellular space after the single cell was permeabilised was demonstrated. In total ca. 20 fmol lactate was detected from a single aerobic myocyte, giving the estimated average concentration of intracellular lactate to be 2.0 ± 0.1 mM. In a primarily study of an anoxia model, in total ca. 150 fmol lactate, equivalent to an intracellular lactate concentration of 15 mM, was detected in the extracellular space around cells equilibrated with 2 mM of the mitochondrial inhibitor FCCP. The electrodes of the device needed to be regenerated by dry etching after each cell assay. The integrated Ag|AgCl electrode particularly showed poor biocompatibility with the cell assay, causing the reference electrode to degrade, unless it was regenerated.

Further, a new platform based on an array of poly(dimethylsiloxane) (PDMS) microchannels integrated with a microelectrode array was presented. This device demonstrated the advantage of allowing single-cell manipulation within microfluidic channels, with the potential to allow the parallel handling and analysis of single cells. In addition, this device improved the use efficiency without the need to regenerate fouled electrodes. The microelectrode array was also electrochemically characterised as both a free and an immobilised enzyme sensor for measurement of lactate. In this array device, Ca^{2+} flux from electrically stimulated single cells and intracellular pH were monitored in real time during continuous contraction for long periods. Intracellular Ca^{2+} flux with the decreased amplitude over time and nearly eased after 20 minutes of continuous contraction. Intracellular pH decreased gradually until a dramatic break-down point was seen. Lactate was then monitored in real time during the course of intracellular acidosis to explore the relation between lactate efflux and acidosis metabolism. The initial results indicate that the significant intracellular pH decrease might not be directly attributable to the accumulation of intracellular lactate. Although there is not sufficient information about lactate release during the course of acidosis, partly due to the cell membrane being compromised during contraction, the array system has shown the potential to enable simultaneous electrical and optical monitoring of extra- and intracellular metabolites from single beating heart cells to address significant technical requirements with respect to both fundamental and applied studies. Finally, new materials and methods which yield simple, cost-effective routes to integrate microfluidic systems were described. Devices towards high-throughput analysis of single cells were proposed.

References

1. Microcolumn separations and the analysis of single cells. Kennedy, R. T.; Oates, M. D.; Cooper, B. R.; Nickerson, B.; Jorgenson, J. W. *Science.* 1989, 246, 57-63.

2. Single-cell analysis by capillary electrophoresis. Stuart, J. N.; Sweedler, J. V. *Anal. Bioanal. Chem.* 2003, 375, 28-29.

3. Single-cell analysis by electrochemical detection with a microfluidic device. Xia, F. Q.; Jin, W. R.; Yin, X. F.; Fang, Z. L. *Journal of Chromatography.* 2005, 1063, 227-233.

4. New approaches to single-cell analysis by capillary electrophoresis Zabzdyr, J.L.; Lillard, S.J. *TrAC Trends in Analytical Chemistry.* 2001, 20, 467-476.

5. Recent developments in single-cell analysis. Lu, X.; Huang, W. H.; Wang, Z. L.; Cheng, J. K, *Analytica Chimica Acta.* 2004, 510, 127-138.

6. Simultaneous detection of catecholamine exocytosis and Ca2+ release from single bovine chromaffin cells using a dual microsensor. Xin, Q.; Wightman, R. M. *Anal. Chem.* 1998, 70, 1677-1681.

7. Amperometric monitoring of stimulated catecholamine release from rat pheochromocytoma (PC12) cells at the zeptomole level. Chen, T. K.; Luo, G.; Ewing, A. G. *Anal. Chem.* 1994, 66, 3031-3035.

8. Insulin-stimulated insulin secretion in single pancreatic beta cells. Aspinwall, C. A.; Lakey, J. T.; Kennedy, R. T. *J. Biol. Chem.* 1999, 274, 6360-6365.

9. Single-cell measurements of purine release using a micromachined electroanalytical sensor. Bratten, C. D. T.; Cobbold, P. H.; Cooper, J. M. *Anal. Chem.* 1998, 70, 1164-1170.

10. Towards electronic Petri dishes and picolitre-scale single-cell technologies. Cooper, J. M., *Trend in Biotechnology.* 1999, 17, 226-230.

11. Temporally resolved catecholamine spikes correspond to single vesicle release from individual chromaffin cells. Wightman, R. M.; Jankowski, J. A.; Kennedy, R. T.; Kawagoe, K. T.; Schroeder, T. J.; Leszczyszyn, D. J.; Near, J. A.; Diliberto, E. J.; Viveros, O. H. *Proc. Natl. Acad. Sci. U.S.A.* 1991, 88, 10754-10758.

12. Voltammetric and pharmacological characterization of dopamine release from single exocytotic events at rat pheochromocytoma (PC12) cells. Kozminski, K. D.; Gutman, D. A.; Ewing, A. G. et al. *Anal. Chem.* 1998, 70, 3123-3130.

13. Exocytotic release from individual granules exhibits similar properties at mast and chromaffin cells. Pihel, K.; Travis, E. R.; Borges, R.; Wightman, R. M. *Biophys. J.* 1996, 71, 1633-1640.

14. Electrochemical detection of histamine and 5-hydroxytryptamine at isolated mast cells. Pihel, K.; Hsieh, S.; Jorgenson, J. W.; Wightman, R. M. *Anal. Chem.* 1995, 67, 4514-4521.

15. Electrochemical detection of exocytosis at single rat melanotrophs. Paras, C. D.; Kennedy, R. T. *Anal. Chem.* 1995, 67, 3633-3637.

16. Extracellular pH causes rapid release of insulin from Zn-insulin precipitates during exocytosis. Kennedy, R. T., Huang, L., Aspinwall, C. A. *J. Am. Chem. Soc.* 1996, 118, 1795-1796.

17. Exploring single cell dynamics using chemically modified microelectrodes. Huang, L., Kennedy, R. T. *Tr. Anal. Chem.* 1995, 14, 158-164.

18. A method for the fabrication of low-noise carbon fiber nanoelectrodes. Huang, W. H.; Pang, D.W.; Tong, H.; Wang, Z. L; Cheng, J. K. *Anal. Chem.* 2001, 73, 1048-1052.

19. Spatial and temporal amperometric monitoring dopamine release from single PC12 cells with carbon fiber nanoelectrode. Huang, W.H.; Zhang, L. Y.; Cheng, W.; Pang, D. W.; Wang, Z. L.; Cheng, J. K. *Chem. J. Chin. Univ.* 2003, 24, 425-427.

20. Monitoring dopamine release from single living vesicles with nanoelectrodes. Wu, W.Z.; Huang, W. H.; Wang, W.; Wang, Z. L.; Cheng, J. K.; Xu, T.; Zhang, R.Y.; Chen, Y.; Liu, J. *J. Am. Chem. Soc.* 2005, 127, 8914-8915.

21. Real-time amperometric measurements of zeptomole quantities of dopamine released from neurons. Hochstetler, S. E.; Puopolo, M.; Gustincich, S.; Raviola, E.; Wightman, R. M., et al. *Anal. Chem.* 2000, *72*, 489-496.

22. Detection of secretion from single pancreatic beta-cells using extracellular fluorogenic reactions and confocal fluorescence microscopy. Qian, W. J.; Aspinwall, C. A.; Battiste, M. A.; Kennedy, R. T. *Anal. Chem.* 2000, 72, 711-717.

23. Detection and imaging of zinc secretion from pancreatic beta-cells using a new fluorescent zinc indicator. Gee, K. R.; Zhou, Z. L.; Qian, W. J.; Kennedy, R. T. *J. Am. Chem. Soc.* 2002, 124, 776-778.

24. Dopamine transport into a single cell in a picoliter vial. Troyer, K.P., Wightman, R.M. *Anal. Chem.* 2002, 74, 5370-5375.

25. Imaging single events at the cell membrane. Jaiswal, J. K.; Simon, S. M. *Nature Chemical Biology.* 2007, 3, 92-98.

26. Light microscopy techniques for live cell imaging. Stephéns, D. J., Allan, V. J. *Science.* 2003, 300, 82-86,

27. Imagining imaging's future. Tisen, R. Y. *Nature Reviews Molecular Cell Biology.* 2003, 4, SS16-SS21.

28. Single-bead, single-molecule, single-cell fluorescence: technologies for drug screening and target validation. Hintersteiner, M.; Auer, M. *Ann N Y Acad Sci.* 2008, 1130, 1-11.

29. Regulation of dense core release from neuroendocrine cells revealed by imaging single exocytic events. Angleson, J. K.; Cochilla, A. J.; Kilic, G.; Nussinovitch, I.; Betz, W. J. *Nat Neurosci.* 1999, 2, 440-446.

30. Temporal and spatial monitoring of exocytosis with native fluorescence imaging microscopy. Lillard, S. J.; Yeung, E. S. *J. Neurosci. Methods.* 1997, 75, 1, 103-109.

31. Dynamic inhibition of excitatory synaptic transmission by astrocyte-derived ATP in hippocampal cultures. Koizumi, S.; Fujishita, K.; Tsuda, M.; Shigemoto-Mogami, Y.; Inoue, K. *Proc Natl Acad Sci.* 2003, 16, 11023-11028.

32. Fluorescence microscopy of stimulated Zn^{2+} release from organotypic cultures of mammalian hippocampus using a carbonic anhydrase-based biosensor system. Thompson, R. B.; Whetsell, W. O.; Maliwal, B. P.; Fierke, C. A.; Frederickson, C. J. *J. Neurosci. Methods.* 2000, 96, 35-45.

33. Optical imaging fiber-based single live cell arrays: a high-density cell assay platform. Brian, I.; Walt, D. R.; *Anal. Chem.* 2002, 74, 3046-3054.

34. On the use of single-cell fluorescence imaging for the measurement of intracellular ion concentrations. Ginsburg, H. *Parasitol Today.* 2000, 16, 40-41.

35. Fluorescence imaging of signaling networks. Meyer, T.; Teruel, M. N.; *Trends Cell Biol.* 2003, 13, 101-106.

36. Microtubules meet substrate adhesions to arrange cell polarity. Small, J. V., Kaverina, I. *Curr. Opin. Cell Biol.* 2003, 15, 40-47.

37. A FRET-based sensor reveals large ATP hydrolysis-induced conformational changes and three distinct states of the molecular motor myosin. Shih, W. M.; Gryczynski, Z.; Lakowicz, J.R.; Spudich, J.A. *Cell.* 2000, 102, 683-694.

38. Direct observation of calcium-independent intercellular ATP signaling in astrocytes. Wang, Z.; Haydon, P. G.; Yeung, E. S. *Anal. Chem.* 2000, 72, 2001-2007.

39. Simultaneous monitoring of Zn^{2+} secretion and intracellular Ca^{2+} from islets and islet cells by fluorescence microscopy. Qian, W.J.; Peters, J.L.; Dahlgren, G.M.; Gee, K.R.; Kennedy, R. T. *Biotechniques.* 2004 37, 922-924.

40. In vivo imaging of quantum dots encapsulated in phospholipid micelles. Dubertret, B.; Skourides, P.; Norris, D. J.; Noireaux, V.; Brivanlou, A. H.; Libchaber, A. B. *Science.* 2002, 298, 1759-1762.

41. Imaging of Zn^{2+} release from pancreatic beta-cells at the level of single exocytotic events. Qian, W.J.; Gee, K.R.; Kennedy, R. T. *Anal. Chem.* 2003, 75, 3468-3475.

42. Single channel recording. Sakmann, B.; Neher, E. 1995. Plenum Press, New York.

43. Development of excitation-contraction coupling in cardiomyocytes. Tohse, N.; Seki, S.; Kobayashi, T.; Tsutsuura M.; Nagashima M.; Yamada Y. *Jpn J Physiol.* 2004, 54(1), 1-6.

44. Calcium-induced release of calcium from the cardiac sarcoplasmic reticulum. Fabiato, A. *Am J Physiol Cell Physiol.* 1983, 245, 1-14.

45. Excitation-Contraction Coupling and Cardiac Contractile Force. Bers, D. M. 2003. Kluwer Academic, Boston.

46. Calcium microdomains: organization and function. Berridge, M. J. *Cell Calcium.* 2006, 40, 405-412.

47. Cardiac excitation-contraction coupling. Bers, D. M. *Nature.* 2002, 415, 198-205.

48. Relaxation in rabbit and rat cardiac cells: species dependent differences in cellular mechanisms. Bassani, J. W. M.; Bassani, R. A.; Bers, D. M. *J. Physiol.* 1994, 476, 279-293.

49.   The control of calcium release in heart muscle. Cannell, M. B.; Cheng, H.; Lederer, W. J. *Science.* 1995, 268, 1045-1049.

50.   Theory of excitation-contraction coupling in cardiac muscle. Stern, M. D. *Biophysical Journal.* 1992, 63, 497-517

51.   The effects of overexpression of the Na+/Ca2+ exchanger on calcium regulation in hypertrophied mouse cardiac myocytes. Stagg, M. A.; Malik, A. H.; MacLeod, K. T.; Terracciano, C. M. N. *Cell Calcium.* 2004, 36, 111-118.

52.   Cellular functions of diabetic cardiomyocytes: contractility, rapid-cooling contracture, and ryanodine binding. Yu, Z.; Tibbits, G. F.; McNeill, J. H.; *Am. J. Physiol.* 1994, 266, 2082-2089.

53.   Signaling to the nucleus by an L type calcium channel calmodulin complex through the MAP kinase pathway. Dolmetsch, R. E.; Pajvani U.; Fife K.; Spotts, J. M.; Greenberg, M. E. *Science.* 2001, 294, 333-339.

54.   Abnormal intracellular Ca2+homeostasis and disease. Missiaen, L.; Robberecht, W.; Van Den Bosch, L.; Callewaert, G. et al., *Cell Calcium* 2000, 28, 1-21.

55.   The myofilament force-calcium relationship as a target for positive inotropic therapy in congestive heart failure. MacGowan, G. A. *Cardiovasc. Drug Ther.* 2005, 19, 203-210.

56.   Caffeine enhances the calcium-dependent cardiac mitochondrial permeability transition: relevance for caffeine toxicity Sardão, V. A.; Oliveira, P. J.; Moreno, A. J. M. *Toxicol. Appl. Pharmacol.* 2002, 179, 50-56.

57.   Recent advances in technology for measuring and manipulating cell signals. Zacharias, D.A.; Baird, G.S.; Tsien, R.Y. *Current Opinion in Neurobiology* 2000, 10, 416-421.

58.   Measurement of cytosolic free Ca^{2+} with Quin2. Tsien. R.Y.; Pozzan T. *Method in Enzymology.* 1989, 172, 230-244.

59.   Monitoring cell calcium. *In Calcium as a Cellular Regulator,* Tsien, R.Y. 1999. ed. by E. Carafoli and C. Klee. New York: Oxford University Press, 28-54.

60.   Measurement of intracellular calcium Takahashi, A.; Camacho, P.; Lechleiter, D. J.; Herman, B. *Physiological Reviews.* 1999, 79, 1089-1125.

61.   Measurement of Intracellular Calcium Concentration Using Confocal Microscopy *In Calcium Signaling Protocols*, Perez-Terzic, C.; Jaconi, M.; Stehno-Bittel, L. 1999.ed. by Lambert, D. G. New York: Humana Press, 75-91.

62. Micromachining a miniaturized capillary electrophoresis-based chemical analysis system on a chip. Harrison, D. J; Fluri, K.; Seiler, K.; Fan, Z.; Effenhauser, C.S.; Manz, A. *Science.* 1993, 261, 895-897.

63. Physics and applications of microfluidics in biology. Beebe,D.J.; Mensing, G.A.; Walker, G.M. *Annu. Rev. Biomed. Eng.* 2002, 4, 261-286.

64. Miniaturized total analysis systems for biological analysis. Jakeway, S. C.; de Mello, A. J.; Russell, E. L. *Fresenius J. Anal. Chem.* 2000, 366, 525-539.

65. Microfabricated devices in biotechnology and biochemical processing. Chovan, T.; Guttman, A. *Trends Biotechnol.* 2002, 20, 116-122.

66. Microfluidic chips for clinical and forensic analysis. Verpoorte, E. *Electrophoresis.* 2002, 23, 677-712.

67. Biosensors and biochips: advances in biological and medical diagnostics. Vo-Dinh, T.; Cullum, B. *Fresenius J. Anal. Chem.* 2000, 366, 540-551.

68. Micro total analysis systems. Latest advancements and trends. Dittrich, P. S.; Tachikawa, K.; Manz, A. *Anal. Chem.* 2006, 78, 3887-3908.

69. Micro total analysis systems. Recent developments. Vilkner, T.; Janasek, D.; Manz, A. *Anal. Chem.* 2004, 76, 3373-3385.

70. Using individual cells as experimentation platforms. Andersson, H.; Van den Berg, A. *NanoBioTechnology* 2005, 1, 319-321.

71. Microfluidic devices for cellomics. Andersson, H.; Van den Berg, A. *Sensor and Actuators B.* 2003, 92, 315-325.

72. Microtechnologies and nanotechnologies for single-cell analysis. Andersson, H.; Van den Berg, A. *Current Opinion in Biotechnology* 2004, 15, 44-49.

73. Integrated microfluidic devices. Erickson, D.; Li, D. Q., *Analytica Chimica Acta.* 2004, 507, 11-26.

74. Microfluidics technology for manipulation and analysis of biological cells. Yi, C. Q.; Li, C. W.; Ji, S. L.; Yang, M. S. *Analytica Chimica Acta.* 2006, 560, 1-23.

75. Transport, manipulation, and reaction of biological cells on-chip using electrokinetic effects. Li, P. C.; Harrison, D. J. *Anal. Chem.* 1997, 69, 1564-1568.

76. A chip-based biosensor for the functional analysis of single ion channels. Schmidt, C.; Mayer, M.; Vogel, H. *Angew Chem Int.* 2000, 39, 3137-3140.

77. High-speed separation system of randomly suspended single living cells by laser trap and dielectrophoresis Arai, F.; Ichikawa, A.; Ogawa, M.; Fukuda, T.; Horio, K.; Itoigawa, K. *Electrophoresis.* 2001, 22, 283-288.

78. An optically driven pump for microfluidics. Leach, J.; Mushfique, H.; Leonardo, D. M.; Padgett, M.; Cooper, M. J. *Lab Chip.* 2006, 6, 735-739.

79. On-chip single-cell microcultivation assay for monitoring environmental effects on isolated cells. Umehara, S.; Wakamoto, Y.; Inoue, I.; Yasuda, K. *Biochem. Biophys. Res. Commun.* 2003, 305, 534-540.

80. Optical tweezers applied to a microfluidic system. Enger, J.; Goksör, M.; Ramser, K.; Hagberg, P.; Hanstorp, D. *Lab Chip.* 2004, 4,196-200.

81. Filter-based microfluidic device as a platform for immunofluorescent assay of microbial cells. Zhu, L.; Zhang, Q.; Feng, H.; Ang, S.; Chau, F. S.; Liu, W. T. *Lab Chip.* 2004, 4, 337-341.

82. Development of a rare cell fractionation device: application for cancer detection. Mohamed, H.; McCurdy, L.D.; Szarowski, D. H.; Duva, S.; Turner, J. N.; Caggana, M. *IEEE Trans. Nanobiosci.* 2004, 3, 251-256.

83. In situ fabricated porous filters for microsystems. Moorthy, J.; Beebe, D. J., *Lab Chip.* 2003, 3, 62-66.

84. Continuous particle separation through deterministic lateral displacement. Huang, L. R.; Cox, E. C.; Austin, R. H.; Sturm, J. C., *Science.* 2004, 304, 987-990.

85. Molded polyethylene glycol microstructures for capturing cells within microfluidic channels. Khademhosseini, A.; Yeh, J.; Jon, S.; Eng, G.; Suh, K.Y.; Burdick, J.A.; Langer. R. *Lab Chip.* 2004, 4, 425-430.

86. Chip-based bioassay using bacterial sensor strains immobilized in three-dimensional microfluidic network. Tani, H.; Maehana, K.; Kamidate, T. *Anal. Chem.* 2004, 76, 6693-6697.

87. Surface engineering with poly(ethylene glycol) photolithography to create high-density cell arrays on glass. Revzin, A.; Tompkins, R. G.; Toner, M. *Langmuir.* 2003, 19, 9855-9862.

88. Cell docking and on-chip monitoring of cellular reactions with a controlled concentration gradient on a microfluidic device. Yang, M. S.; Li, C. W.; Yang, J. *Anal. Chem.* 2002, 74, 3991-4001.

89. Hydrodynamic simulation of cell docking in microfluidic channels with different dam structures. Yang, J.; Li, C. W.; Yang, M. S. *Lab Chip.* 2004, 4, 53-59.

90. PDMS-based microfluidic device with multi-height structures fabricated by single-step photolithography using printed circuit board as masters. Li, C.W.; Cheung, C. N.; Yang, J.; Tzang, C. H.; Yang, M. S. *Analyst.* 2003,128,1137-1142.

91. Reactive polymer coatings: a first step toward surface engineering of microfluidic devices. J. Lahann, J.; Balcells, M.; Lu, H.; Rodon, T.; Jensen, K.F.; Langer, R. *Anal. Chem.* 2003, 75, 2117-2122.

92. Programmable modification of cell adhesion and zeta potential in silica microchips. Kirby, B.J.; Wheeler, A.R.; Zare, R.N.; Fruetel, J.A.; Shepodd, T. J. *Lab Chip.* 2003, 3, 5-10.

93. Surface passivation of a microfluidic device to glial cell adhesion: a comparison of hydrophobic and hydrophilic SAM coatings. Cox, J.D.; Curry, M.S.; Skirboll, S.K.; Gourley, P.L.; Sasaki, D.Y.; *Biomaterials.* 2002, 23, 929-935.

94. Biomimetic technique for adhesion-based collection and separation of cells in a microfluidic channel. Chang, W. C.; Lee, L. P.; Liepmann, D.; *Lab Chip.* 2005, 5, 64-73.

95. Enzymatic methods for in situ cell entrapment and cell release. Chen, T.H.; Small, D. A.; McDermott, M. K.; Bentley, W. E.; Payne, G. F. *Biomacromolecules.* 2003, 4, 1558-1563.

96. Electrodeless dielectrophoresis of single- and double-stranded DNA. Chou C. F.; Tegenfeldt, J. O.; Bakajin, O.; Chan, S. S.; Cox, E. C.; Darnton, N.; Duke, T.; Austin, R. H.; *Biophys. J.* 2002, 83, 2170-2179.

97. Transport, location, and quantal release monitoring of single cells on a microfluidic device. Huang, W. H.; Cheng, W.; Zhang, Z.; Pang, D.W.; Wang, Z. L.; Cheng, J. K.; Cui, D. F.; *Anal. Chem.* 2004, 76, 483-488.

98. Perfusion and chemical monitoring of living cells on a microfluidic chip. Shackman, J. G.; Dahlgren, G. M.; Peters, J. L.; Kennedy R. T. *Lab Chip.* 2005, 5, 56-63.

99. Patch clamping by numbers. Wood, C.; Williams, C.; Waldron, G. J. *Drug Discov. Today.* 2004, 9, 434-441.

100. Whole cell patch clamp recording performed on a planar glass chip. Fertig, N.; Robert, H. B.; Behrends, J. C. *Biophys. J.* 2002, 82, 3056-3062.

101. Mammalian electrophysiology on a microfluidic platform. Ionescu-Zanetti, C.; Shaw, R. M.; Seo, J.; Jan, Y. N.; Jan, L. Y.; Lee, L. P. *PNAS.* 2005, 102, 9112-9117.

102. Integration of single cell injection, cell lysis, separation and detection of intracellular constituents on a microfluidic chip. Gao, J.; Yin, X. F.; Fang, Z. L.; *Lab Chip.* 2004, 4, 47-52.

103. Converting a protease assay to a caliper format lab chip system. Johnson, M.; Li, C.; Rasnow, B.; Grandsard, P.; Xing, H.; Fields, A. *Journal of the Association for Laboratory Automation.* 2002, 7, 62-68.

104. Amperometric detection of quantal catecholamine secretion from individual cells on micromachined silicon chips. Chen, P.; Xu, B.; Tokranova, N.; Feng, X.; Castracane, J.; Gillis, K. D. *Anal. Chem.* 2003, 75, 518-524.

105. Microfluidic device for single-cell analysis. Wheeler, A. R.; Throndset, W. R.; Whelan, R. J.; Leach, A. M.; Zare, R. N.; Liao, Y. H.; Farrell, K.; Manger, I. D.; Daridon, A. *Anal. Chem.* 2003, 75, 3581-3586.

106. On-chip amperometric measurement of quantal catecholamine release using transparent indium tin oxide electrodes. Sun, X.; Gillis, K. D.; *Anal Chem.* 2006, 78, 2521-2525.

107. Electroanalysis of metabolic flux from single cells in simple picoliter-volume microsystems. Yasukawa, T., Glidle, A., Cooper, J. M., Matsue, T. *Anal. Chem.* 2002, 74, 5001-5008.

108. Single-cell measurements of purine release using a micromachined electroanalytical sensor. Bratten, C. D. T.; Cobbold, P. H.; Cooper, J. M. *Anal. Chem.* 1998, 70, 1164-1170.

109. Towards electronic petri dishes and picolitre-scale single-cell technologies. Cooper, J. M., *Trend in Biotechnology* 1999, 17, 226-230.

110. Ultra-low-volume, real-time measurements of lactate from the single heart cell using microsystems technology. Cai, X.; Klauke, N.; Glidle, A.; Cobbold, P.; Smith, G. L.; Cooper, J. M.; *Anal. Chem.* 2002, 74, 908-914.

111. Voltammetric and pharmacological characterization of dopamine release from single exocytotic events at rat pheochromocytoma (PC12) cells. Kozminski, K.

D.; Gutman, D. A.; Davila, V.; Sulzer, D.; Ewing, A. G. et al. *Anal. Chem.* 1998, 70, 3123-3130.

112. Microfluidic single-cell analysis of intracellular compounds Chao, T. C.; Ros, A. *J. R. Soc. Interface.* 2008, 5, 139-150.

113. Recent advances in electric analysis of cells in microfluidic systems Chang, L.; Bao, N.; Wang, J. *Anal Bioanal Chem.* 2008, 391, 933-942.

114. Cell culture models in microfluidic systems. Meyvantsson. I.; Beebe, D. J. Annual Review of Analytical Chemistry. 2008, 1, 423-449.

115. Electronic sensors with living cellular components Kovacs, G. T. A., *Proceedings of the IEEE.* 2003, 91 (6) 915-929.

116. Stimulation of single isolated adult ventricular myocytes within a low volume using a planar microelectrode array. Klauke, N.; Smith, G. L.; Cooper, J. *Biophys. J.* 2003, 85, 1766-1774.

117. A microfluidic device to confine a single cardiac myocyte in a sub-nanoliter volume on planar microelectrodes for extracellular potential recordings. Werdich, A. A.; Lima, E. A.; Ivanov, B.; Ges, I.; Anderson, M. E.; Wikswo, J. P.; Baudenbacher, F. J. *Lab Chip.* 2004, 4, 357-62.

118. Extracellular recordings of field potentials from single cardiomyocytes. Klauke, N., Smith, G.; Cooper, J. M. *Biophys. J.* 2006, 91, 2543-2551.

119. Microfluidic Partitioning of the Extracellular Space around Single Cardiac Myocytes. Klauke, N., Smith, G.; Cooper, J. M. *Anal. Chem.* 2007, 79, 1205-1212.

120. Sarcoplasmic reticulum calcium release is stimulated and inhibited by Daunorubicin and Daunorubicinol. Olson, R. D.; Li, X.; Palade, P.; Shadle, S. E. et al., *Toxicol. Appl. Pharmacol.* 2000, 169, 168-176.

121. Microfluidic selection and retention of a single cardiac myocyte, on-chip dye loading, cell contraction by chemical stimulation, and quantitative fluorescent analysis of intracellular calcium. Li X. J.; Li P. C. H. *Anal. Chem.* 2005, 77, 4315-4322.

122. Real-time monitoring of intracellular calcium dynamic mobilization of a single cardiomyocyte in a microfluidic chip pertaining to drug discovery. Li, X. J.; Huang, J. B.; Tibbits, G. F.; Li P. C. H. *Electrophoresis* 2007, 28, 4723-4733.

123. On-chip acidification rate measurements from single cardiac cells confined in sub-nanoliter volumes Ges, I. A.; Dzhura, I. A.; Baudenbacher, F. J. *Biomedical Microdevices.* 2008, 10, 347-354.

124. Microfluidic device to confine single cardiac myocytes in sub-nanoliter volumes for extracellular pH measurements. Ges, I. A.; Baudenbacher, F. *Journal of Experimental Nanoscience.* 2008, 3, 63-75.

125. Dynamic responses of single cardiomyocytes to graded ischemia studied by oxygen clamp in on-Chip picochambers. Ganitkevich, V.; Reil, S.; Schwethelm, B.; Schroeter, T.; Benndorf, K. *Circulation Research.* 2006, 99, 165-171.

126. Influence of electrical axis of stimulation on excitation of cardiac muscle cells. Tung, L., Sliz, N.; Mulligan, M. R.; *Circ. Res.* 1991, 69, 722-730.

127. Real-time measurement of transmitter release from single synaptic vesicles. Bruns, D.; Jahn, R. *Nature.* 1995, 377, 62-65.

128. Zones of exocytotic release on bovine adrenal medullary cells in culture. Schroeder, T. J.; Jankowski, J. A.; Senyshyn, J.; Holz, R. W.; Wightman, R. M. *Journal of Biological Chemistry,* 1994, 269,17215-17220.

129. Colocalization of calcium entry and exocytotic release sites in adrenal chromaffin cells. Robinson, I. M., Finnegan, J. M.; Monck, J. R.; Wightman, R.M.; Fernandez, J. M. *Proceedings of the National Academy of Sciences of the United States of America.* 1995, 92, 2474-2478.

130. Immobilization of Enzymes and Cells. Guisan, J. M. 2006, Humana Press, New York.

131. A review of the immobilization of enzymes in electropolymerized films. Bartlett, P. N.; Cooper, J. M. *J. Electroanal. Chem.* 1993, 362, 1-12.

132. An in situ electrosynthesized amperometric biosensor based on lactate oxidase immobilized in a poly-o-phenilenediamine film: determination of lactate in serum by flow injection analysis. *Biosens. Bioelectron.*1994, 9, 471-479.

133. Multianalyte sensor for the simultaneous determination of glucose, L-lactate and uric acid based on a microelectrode array. Frebela, H.; Chemnitiusa, G. C.; Cammanna, K.; Kakerowb, R.; Rospertb, M.; Mokwab, W. *Sensors and Actuators B,* 1997, 43, 87-93.

134. Exercise Metabolism. Hargreaves, M.; Spriet, L. L. *Human Kinetics*. 2nd Edition 2006, Champaign, IL.

135. Analysis of electric field stimulation of single cardiac muscle cells. Tung, L.; Borderies. J. R. *Biophys. J.* 1992, 63, 371-386.

136. Intracellular pH recovery during respiratory acidosis in perfused hearts. Vandenberg, J. I.; Metcalfe, J. C.; Grace, A. A.; *Am J Physiol.* 1994, 266, C489-C497.

137. Mechanisms of pH$_i$ recovery after global ischemia in the perfused heart. Vandenberg, J. I.; Metcalfe, J. C.; Grace, A. A. *Circ Res.* 1993, 72, 993-1003.

138. Single-cell electroporation. Olofsson, J.; Nolkrantz, K.; Ryttsen, F.; Lambies, B. A.; Weber, S. G.; Orwar, O. *Curr Opin Biotechnol.* 2003, 14, 29-34.

139. Lactate Physiologic, Methodologic and Pathologic Approach. Moret, P. R.; Weber, J.; Haissly, J.; Denolin, H. *Springer-Verlag: Berlin,* 1980, 16, 174-180.

140. Contraction and intracellular Ca^{2+}, Na^+, and H^+ during acidosis in rat ventricular myocytes. Harrison, S. M.; Frampton, J. E.; McCall, E.; Boyett, M. R.; Orchard, C. H. *Am. J. Physiol. Cell Physiol.* 1992, 262, C348-C357.

141. Determination of molecular self-diffusion coefficient using multiple spin-echo NMR spectroscopy with removal of convection and background gradient artifacts, Zhang, X.; Li C. G.; Ye. C.H.; Liu, M. L. *Anal. Chem.* 2001, 73, 3528-3534.

142. Microelectrodes. Definitions, characterization, and applications (Technical report) Štulik, K.; Aamatore, C.; Holub, K.; Marecek, V, Kutner, W. *Pure and Applied Chemistry* 2000, 72, 1483-1492.

143. Muscles, Reflexes, and Locomotion. Thomas, M. A. *Princeton University Press.* 1984, Princeton.

144. Lactate, not pyruvate, is neuronal aerobic glycolysis end product: an in vitro electrophysiological study. Schurr, A.; Payne, R. S. *Neuroscience.* 2007, 147, 613-619.

145. Lab-on-a-chip: microfluidics in drug discovery. Dittrich, P. S.; Manz, A. *Nature Reviews Drug Discover*y. 2006, 5, 210-218.

146. Rapid prototyping of microfluidic systems in poly(dimethylsiloxane). Duffy, D. C.; McDonald, J. C.; Schueller, O. J. A.; Whitesides, G. M. *Anal. Chem.* 1998, 70, 4974-4984.

147. Hydrophobic recovery of plasma-treated polydimethylsiloxane. Fritz, J. L.; Owen, M. J. *J. Adhesion.* 1995, 54, 33-45.

148. Monolithic microfabricated valves and pumps by multilayer soft lithography. Unger, M. A.; Chou, H. P.; Thorsen, T.; Scherer, A.; Quake, S. R. *Science.* 2000, 288, 113-116.

149. Fabrication of microfluidic systems in poly (dimethylsiloxane). McDonald, J. C.; Duffy, D. C.; Anderson, J. R.; Chiu, D. T.; Wu, H.; Schueller, O. J. A.; Whitesides, G. M. *Electrophoresis.* 2000, 21, 27-40.

Appendix (Research papers written during the research)

Journal Paper:

Cheng, W, Klauke, N, Sedgwick, H, Smith, G L, Cooper, J M, Metabolic monitoring of the electrically stimulated single heart cell within a microfluidic platform
June, 2006, **LAB-ON-CHIP,** 2006 6 (11):1424-31. (Featured by front cover)

Cheng, W, Klauke, N, Smith, G L, Cooper, Picolitre Cell Array for Metabolic Monitoring of Stimulated Cardiomyocytes, submitted to **Electrophoresis**, May, 2009

Conference Paper:

Cheng, W, Klauke, N, Cooper, J M, Monitoring of single beating heart cells in a microfabricated system, **In Proceedings (and sponsored presentation) of EPSRC Postgraduate Research Conference in Electronics, Photonics, Communications and Software (PREP)**, University of Lancaster, April 2005.

Cheng, W, Klauke, N, Cooper, J M, Real-time monitoring of single beating heart cells in a Lab-on-a-Chip system **In Proceedings (and sponsored presentation) of Gordon Research Analytical Chemistry Conference,** Biological Station, Roscoff, France, June, 2005.